Masters Thesis

Spectroscopic Mode Identifications of Three γ Doradus Stars

Author:
Matthew Davie

Supervisor:
Dr. Karen Pollard

Associate Supervisor:
Prof. Peter Cottrell

Submitted in Partial Fulfilment of the Requirements for the Degree
Master of Science in Astronomy

February 2013

Disclaimer

The work presented on HD 189631 builds upon the prior work of Maisonneuve et al. (2010). It includes the spectra originally obtained in Maisonneuve et al. (2010) and adds a significant number of new spectra for analysis. The reduction and analysis of these were carried out in this thesis. The analysis of QW Puppis includes the spectra examined in Wright (2008) and a large number of new spectra obtained in 2012. These were reduced and analysed in this thesis. The spectra of IR Draconis were the result of a coordinated multi-site spectroscopic observing campaign and were generously provided by Dr. Peter De Cat. These were reduced and analysed in this work and have not been published previously.

Abstract

We present the modes identified for frequencies found in spectroscopic observations of the γ Doradus stars HD 189631, QW Puppis, and IR Draconis. A cross-correlation technique was used to create mean line profiles for HD 189631. Four frequencies and modes were identified for this star: 1.6774 ± 0.0002 d^{-1}, 1.4174 ± 0.0002 d^{-1}, 0.0714 ± 0.0002 d^{-1}, and 1.8228 ± 0.0002 d^{-1} which were identified with the modes (l,m) = $(1, +1)$, $(1, +1)$, $(2, -2)$, and $(1, +1)$ respectively. A least-squares deconvolution method was implemented for line profile generation in the study of QW Puppis and IR Draconis. Three frequencies were identified for QW Puppis: 0.055972 ± 0.000004 d^{-1}, 0.064846 ± 0.000004, and 5.219398 ± 0.000002 d^{-1}. These frequencies were identified with the modes (l,m) = $(1, -1)$, $(4, -1)$, $(4, +1)$. Two frequencies were identified in spectra of the rapidly rotating star IR Draconis: 0.00515 ± 0.00003 d^{-1} and 2.35538 ± 0.00004 d^{-1}; which were identified with (l,m) = $(1, -1)$, and $(1, +1)$ modes respectively. These mode identifications will assist in modelling the structure and interior conditions of these main sequence, non-radially pulsating stars.

"All this happened, more or less"
Kurt Vonnegut

Contents

Figures

Tables

Chapter 1

Introduction

The structure and evolution of a star is in many cases entirely dominated by the processes that take place in the interior of the star. Understanding the stellar interior is a critical part of models describing the stars we see but unfortunately, classical observations do not deliver information about the stellar interior structure. The age, internal composition, extent of the core, and interior rotation of the star cannot be determined by normal observational methods. Without good information, the construction of robust models is deeply challenging.

1.1 Asteroseismology

Variable stars are all around us and there are numerous classified groups of variable stars, from those confined to the instability strip, to the Mira stars and white dwarfs (Figure 1.1).

Asteroseismology is a relatively recently devised field of astronomy originating, unsurprisingly, with observations of our own Sun (Leighton, 1960) before the full implications of these oscillations were understood. The name describes this science well; *aster* meaning star, *seismos* meaning oscillation, and *logos* a discourse or reasoning. This is a line of reasoning about stellar pulsations, or better yet, a discourse told by the stellar pulsations.

A deeply penetrating stellar pulsation may pass from the stellar surface layers to the edge of the core, where its velocity will change and appear to reflect off the pressure or compositional gradient and come back to the surface. A pulsation seen at the surface will bear characteristics related to the media through which it has travelled.

There are two complementary aspects to the growth of understanding in this area: that of the development of models - what we think we understand, and that of mode identification - what we see. This work will analyse some high-quality spectra to identify stellar pulsations with the aim of providing good information to help guide the further development of stellar modelling.

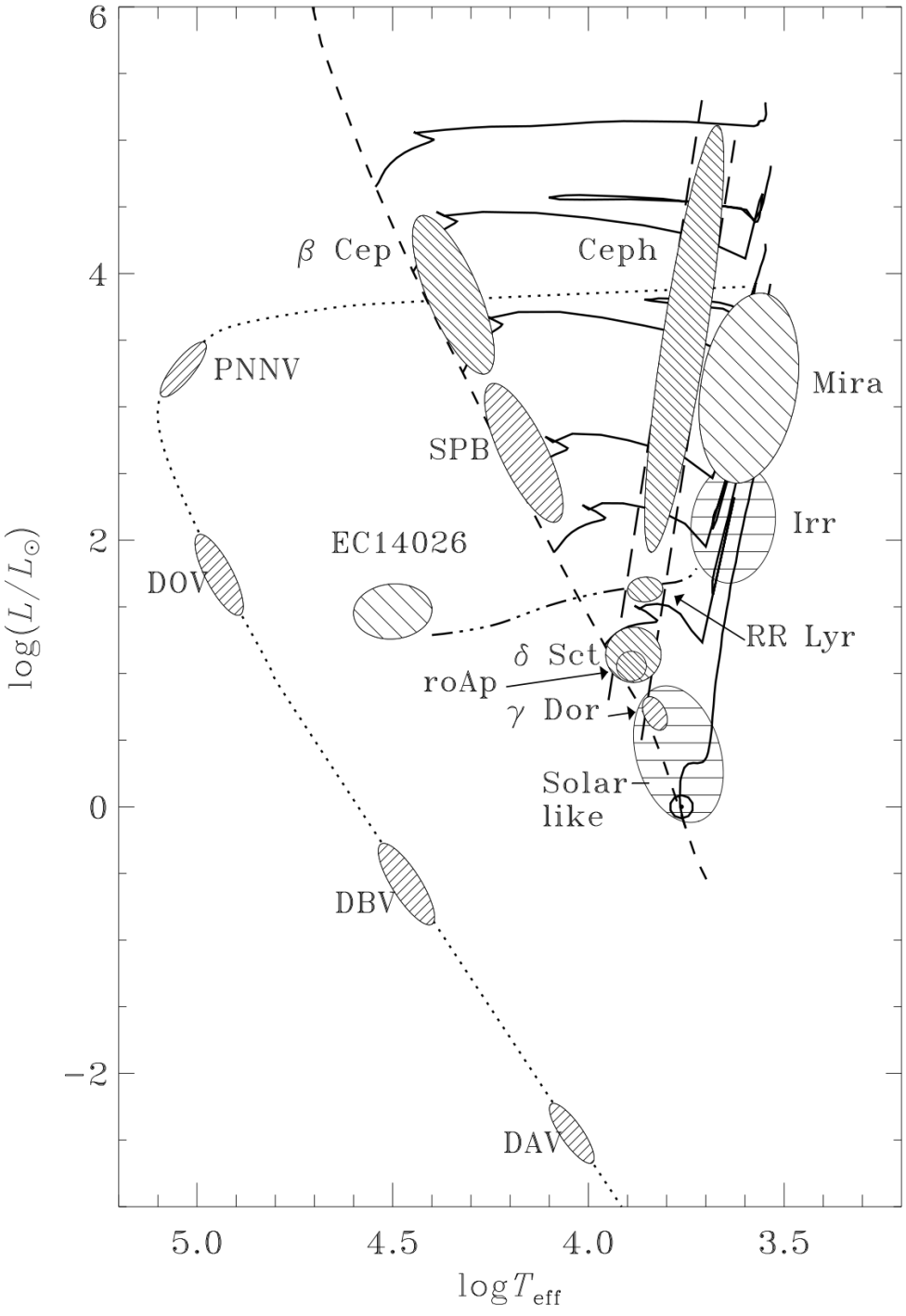

Figure 1.1: Hertzsprung-Russell diagram showing the approximate locations of many of the groups of variable stars known to us. The main sequence is shown for solar abundance with some evolutionary tracks. The classical instability strip extends from the γ Doradus and δ Scuti groups to the Cepheids. Figure taken from Aerts (2006).

1.2 Pulsational Characterisation

1.2.1 Gravity Modes of pulsation

Two types of pulsations are commonly encountered in stellar atmospheres. Pressure modes (p-modes), which are restored by pressure as the name suggests, are acoustic waves. They do not penetrate particularly deeply into the star and are the typical pulsation found in the δ Scuti class of variable stars. Gravity modes (g-modes), however, are buoyant oscillations of a displaced parcel of fluid about its equilibrium position. Equation 1.1, taken from Aerts et al. (2010), shows that the fundamental period Π_0 of such a stellar pulsation is intimately related to the depth of the cavity in which it propagates. The Brunt-Väisälä frequency N (equation 1.2 is a simplified version of this) is closely tied to the density and density gradient of the medium in which the pulsation exists.

$$\Pi_0 = 2\pi^2 \left(\int \frac{N}{r} dr \right)^{-1} \tag{1.1}$$

$$N \equiv \sqrt{-\frac{g}{\rho_0} \frac{\partial \rho(r)}{\partial r}} \tag{1.2}$$

The g-mode pulsations in γ Doradus stars are driven by the interaction of the relatively short convective timescale and the comparatively longer pulsation period. This mechanism was called 'convective blocking' by Pesnell (1987) when the mechanism was posited in a study of white dwarf stars. It occurs when the luminosity perturbation at the base of the convective zone in the star is blocked, leading to heating being in phase with compression in the envelope. Guzik et al. (2000, 2002) proposed it as an explanation for the g-mode pulsations seen in γ Doradus stars and it has been shown that this mechanism is the major driving component for γ Doradus stellar pulsations in model studies (Dupret et al., 2004, 2005).

1.2.2 Spherical geometry of pulsations

Starting with the one dimensional 'vibrating string' oscillator one can start to build up a model in our minds for these pulsations. The number of nodes for this oscillator increases as the frequency increases to higher harmonics. Transitioning from the one dimensional to the two dimensional scenario - observing a flat disc - we could conceivably see nodes repeating in the radial direction as well as around the circumference, and to three dimensions all we need do is imagine it rotating about another vertical or horizontal axis.

In this work a mode will be characterised by (l, m). This is in reference to the spherical harmonic given by equation 1.3, where $l = 0, 1, 2, ...$ and integer m is in the range $-l \leq m \leq l$. This is from the Legendre polynomials (P_l^m) (equation 1.4, Aerts (2006)) that describe these harmonic departures from normal sphericity.

$$Y_l^m(\theta, \phi) = \sqrt{\frac{2l+1}{4\pi} \frac{(l-m)!}{(l+m)!}} P_l^m(cos\theta) e^{im\phi} \tag{1.3}$$

$$P_l^m(x) = \frac{(-1)^m}{2^l l!} \left(1 - x^2\right)^{m/2} \frac{d^{l+m}}{dx^{l+m}} \left(x^2 - 1\right)^l \tag{1.4}$$

l denotes the *degree* of the pulsation, that is the total number of nodal lines at a given radius. m is the *azimuthal order*, the number of nodes intersecting the axis of symmetry. And n

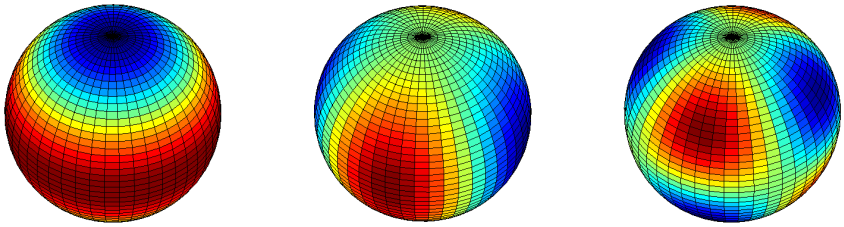

Figure 1.2: Doppler maps of various modes. Left: an (l, m) = (2,0) zonal mode. Middle: an (l, m) = (2,2) sectoral mode. Right: An (l, m) = (3,2) tesseral mode. In terms of visualising this pulsation, imagine that the areas shaded blue are moving radially outwards and the red ones inwards. These pulsations will oscillate, blue will become red and back again over time with a particular frequency.

represents the *radial order*, the number of interior nodal shells in the radial direction; these shells become weaker asymptotically as the base of the convective envelope is approached. If $m = 0$, a zonal mode appears which is set of latitude-constrained oscillating rings. If $l = |m|$ the mode is said to be sectoral, like the segments of an orange. However if $l > |m| > 0$ the pulsation is said to be tesseral (Figure 1.2). Pulsations with prograde motion relative to stellar rotation are assigned positive m values, and retrograde motions negative values, but this is merely a convention and sometimes the opposite sign is used.

1.3 Rotation

Stars are not static relative to our observational reference frame. A star's intrinsic rotation may be more rapid than the propagation of a non-radial pulsation (NRP). This can make the identification of the azimuthal order m a little more challenging in rapidly rotating stars. If a retrograde NRP propagates less quickly in the corotating reference frame than the rotation rate of the star, the pulsation may appear prograde, irrespective of the reality.

$$\sigma_{observed} = \sigma_{corotating} - m\Omega \tag{1.5}$$

Equation 1.5 shows the relationship between the observed frequency and the corotating one, where Ω is the rotational frequency of the star (Maintz et al., 2003). Mode identification is still quite possible if one is well aware of the rotation of the star under examination.

Rotation also broadens spectral lines. For a star of equatorial velocity v inclined at angle i, and given that the spectrum is assumed to be independent of the position on the stellar surface, the observed normalised profile is given by equation 1.6, adapted from Gray (1976; pages 396 and 397).

$$R(t) = \int_{-1}^{1} H(t-y)G(y)dy \quad , \tag{1.6}$$

with
$$y = \frac{\lambda - \lambda_0}{\Delta\lambda_D} \quad , \tag{1.7}$$

where
$$\Delta\lambda_D = \frac{\lambda_0}{c} vsini \tag{1.8}$$

and
$$G(y) = \frac{\int_{-\sqrt{1-y^2}}^{\sqrt{1-y^2}} I_c'(M,\lambda_0)dz}{\int_{-1}^{1} dy \int_{-\sqrt{1-y^2}}^{\sqrt{1-y^2}} I_c'(M,\lambda_0)dz} \tag{1.9}$$

$H(\lambda)$ is the normalised intrinsic stellar spectrum, $G(y)$ is the rotational profile imposed upon it, and z is in the direction of the projection of the rotational axis onto the stellar surface at a point M. Further, $I_c^{'}$ is the emerging continuum intensity corresponding to the cone of solid angle between the normal at point M and the path to the observer.

Wright (2008) applied this in the form of equation 1.10 for a least squares fitting to determine $v\sin i$ when convolved with spectral line profiles.

$$G = \frac{2(1-\varepsilon)\sqrt{1-\left[\frac{\lambda\cdot c}{\lambda_0 v\sin i}\right]^2} + \frac{\pi\varepsilon}{2}\left[1-\left(\frac{\lambda\cdot c}{\lambda_0 v\sin i}\right)^2\right]}{\frac{\pi\lambda v\sin i}{c}\left(1-\frac{\varepsilon}{3}\right)} \tag{1.10}$$

ε is the limb darkening coefficient, λ_0 is the rest wavelength of the line, and λ is the linear vector of wavelengths describing the line profile. One can regard the effect of this rotation as a convolution of the rotational profile with the intrinsic profile. In the Fourier domain, we see the result according to equation 1.11, where $r(\omega), h(\omega), g(\omega)$ are the Fourier transforms of their counterparts in equation 1.6 (Jankov, 1995).

$$r(\omega) = h(\omega) \cdot g(\omega) \tag{1.11}$$

As $G(y)$ scales with $v\sin i$, determination of this projected rotational velocity becomes rather straight forward in the Fourier domain (Royer, 2005), with the need to find only two minima. If the star rotates rapidly enough that the rotational profile is significantly larger than the line profile at a point M (equation 1.9) on the stellar surface, then the stellar variability will give rise to a bump or ripple that will be noted moving across the line profile over time (Berdyugina et al., 2000).

1.4 γ Doradus Stars

γ Doradus stars are a relatively newly-defined class of star. They were a group of variable stars that did not conform to the characteristics of the most similar class, the δ Scuti stars. They all show periods of variability of 0.4 to 3 days with photometric variation of up to 0.1^m in Johnson V (Kaye et al., 1999), and are of spectral type A7 to F5 (Bruntt et al., 2008). The number of confirmed and suspected candidates is growing. Kaye et al. (1999) describe metallicites of around $[M/H] = 0.06$[1], absolute visual magnitudes from 1.93 to 3.07, mean T of 7160 K, and masses about 1.6 $M_\odot$. Handler (1999) quickly offered a defined instability region on the HR diagram for the group (Figure 1.3). This region is in fair agreement with the instability strip found by Kaye et al. (2004) from model simulations. It is noted that this has some significant overlap with the δ Scuti class.

A number of δ Scuti stars have since been reclassified, and a number of hybrid stars have also been noted (including HD49434 from my own work (Davie, 2009) and that of Uytterhoeven et al. (2008) and Chapellier et al. (2011)). These hybrids display both g-mode and p-mode pulsations.

In 2002 γ Doradus stars had been established as targets of significant merit and interest (Zerbi and Kaye, 2002). *MOST*, *CoRoT*, and the *Kepler* space telescopes have all been put to very good use in the study of these stars. Using space-based telescopes allows for the avoidance of aliasing problems associated with frequency analysis of nightly ground-based observations. Ground-based spectroscopy, however, gives access to a good deal more information than just photometry. Telescopes like the 1.2m Euler telescope in La Silla, Chile have been used to characterise γ Doradus stars by the variation of the profile of their spectral lines to readily confirm populations of prospective γ Doradus stars, calculate their metallicity and build up the pool of information on these interesting stars (Bruntt et al., 2008).

More recent findings from the *Kepler* observations have shown that "there are practically no pure δ Scuti or γ Doradus pulsators" (Grigahcène et al., 2010), they are all hybrids to some degree, and a classification scheme has been proposed based on comparison of the amplitudes of the different pulsation frequencies found. The data from *Kepler* have now enabled classification of more than 10,000 stars (Balona et al., 2011). Three subgroups were found in this paper that fall within the γ Doradus instability region. The characteristics of these subgroups have prompted questions about contamination by migrating star-spots.

[1] $[M/H] = log(M/H)_{star} - log(M/H)_\odot$ where M/H is the abundance ratio of metallic elements (Fe, Ti, Si etc.) to H.

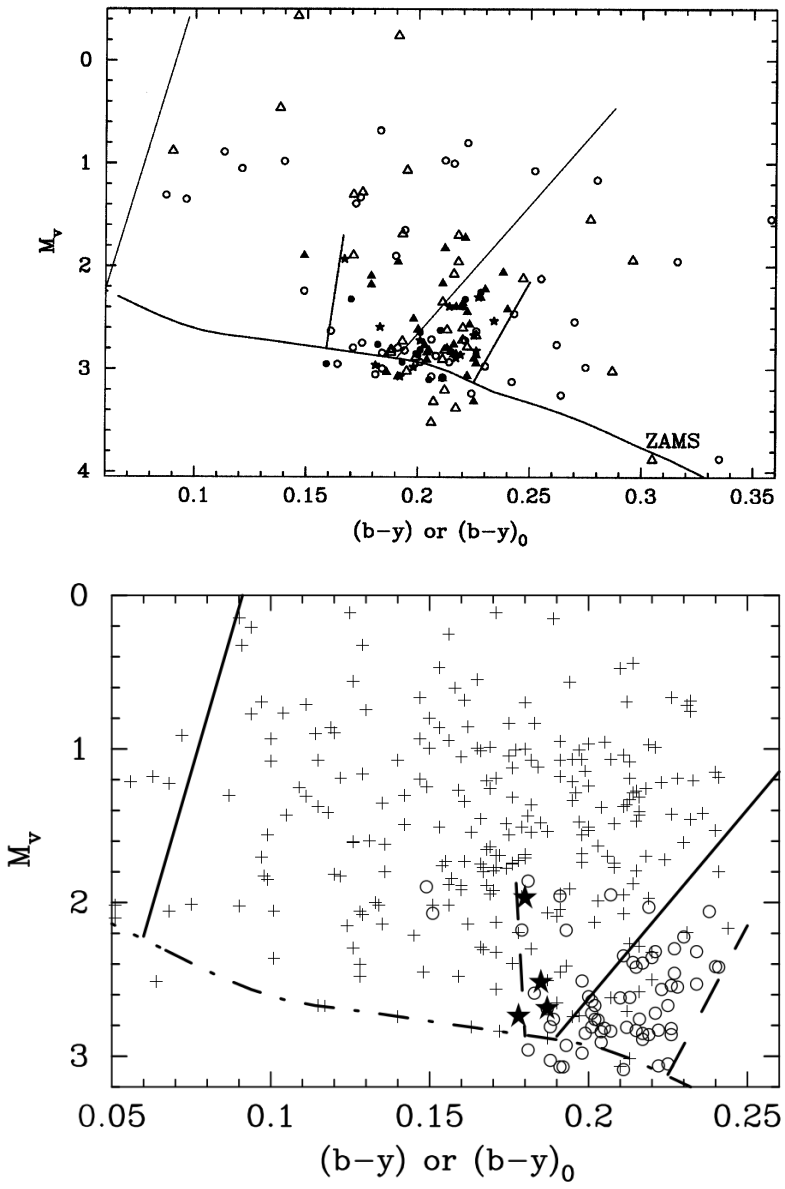

Figure 1.3: Known and suspected γ Doradus variables as of 1999 (upper). Filled circles signify confirmed γ Doradus stars. Other symbols are of those not yet confirmed nor excluded at this date. The zero age main sequence (ZAMS) is shown. The longer lines show the δ Scuti class bounds, and the shorter the domain proposed in the paper from which this diagram is taken (Handler, 1999). Grigahcène et al. (2010) (lower) provides a much more densely populated diagram, with δ Scuti stars shown as plus symbols, γ Doradus stars are shown as open cirles and hybrids as stars.

Target	Right Ascension	Declination	Visual Magnitude
HD 189631	$20^h\ 02^m\ 40.798^s$	$-41°\ 25'\ 03.94''$	7.54
QW Puppis	$07^h\ 12^m\ 33.625^s$	$-46°\ 45'\ 33.49''$	4.5
IR Draconis	$12^h\ 55^m\ 28.548^s$	$+65°\ 26'\ 18.51''$	5.23

Table 1.1: Coordinates and visual magnitudes of targets in this thesis.

1.5 Targets

The coordinates of all three targets observed and analysed in this thesis are given in Table 1.1. The targets for this thesis were chosen based on the fact that they displayed good line profile variations. All are classified as candidate or *bona fide* γ Doradus stars that had a reasonable amount of data from Mt. John University Observatory (MJUO) or from coordinated multi-site campaigns.

1.5.1 HD 189631

This work on HD 189631 continues on from the recommendations for future work in a modest project completed previously by the author (Davie, 2011). This was a re-analysis of the spectra used in the doctoral thesis of Florian Maisonneuve (2010) to find pulsational frequencies and obtain mode identifications for HD 189631. However, the modes identified here are different for f_2 and f_4

In 1999 one period of variability for this star was published: 0.6 d (Handler, 1999), but as the average value of several possible further periods. In 2001 HD 189631 was classified as a γ Doradus star, as pulsation was believed to be the cause of the detected variations and no δ Scuti frequencies were detected (Handler and Shobbrook, 2002).

Perryman and ESA (1997) classified HD 189631 as an A9V star, and Vizier (Ochsenbein et al., 2000) lists the star as an F0V. This distinction is a rather close one to make and any discrepancy is minor. The star has a visual magnitude of 7.54 making it a good target for spectroscopic observation and analysis.

HD 189631 has been found to have a $v\sin i = 43.6 \pm 0.5$ kms^{-1} and a radial velocity of –10.13 kms^{-1} (Maisonneuve et al., 2011). Older publications report radial velocity values of –6.9 kms^{-1} (Duflot et al., 1995), and –6.9 $\pm$ 4.5 kms^{-1} (Gontcharov, 2006), that agree, within uncertainties, with the findings of Maisonneuve et al. (2011).

1.5.2 QW Puppis

QW Puppis is also known as HR 2740 and HD 55892. Its southern declination and V magnitude of 4.5 make it an excellent target for southern hemisphere observations.

QW Puppis was first found to be a variable star by Hensberge et al. (1981), with a period of $P_1 = 0.9363 \pm 0.005$ d. They assumed (not unreasonably) that QW Puppis was a mild Ap star of F0 IV with a $v\sin i$ of 40 kms^{-1}(Slettebak et al., 1975). This was, of course, nearly twenty years before the definition of the γ Doradus class. Beichman et al. (2006) included QW Puppis in their study of debris disks around nearby stars and gave an average metallicity of $[Fe/H] = -0.30$, but it was some time before QW Puppis was looked at again.

Poretti et al. (1997) found four frequencies in a multicolour photometric study of the star. These frequencies were 1.0434±0.0004 d^{-1}, 0.9951±0.0010 d^{-1}, 1.1088±0.0017 d^{-1}

and 0.9019±0.0020 d^{-1}. They also offered a line of reasoning as to why some of these frequencies were not just a result of rotational splitting.

Wright (2008) carried out a spectroscopic study of QW Puppis. It was found by various means to have a $v\sin i$ between 50.6 and 52.4 kms^{-1}. Wright found frequencies of 2.122 d^{-1}, 2.038 d^{-1}, 6.229 d^{-1} and 5.108 d^{-1} via a pixel-by-pixel analysis (PBP), two of which were in agreement with two of the frequencies found by Poretti et al. (1997) when aliases were considered.

1.5.3 IR Draconis

IR Draconis is a northern hemisphere object. It is also known as 8 Draconis, HD 112429 and HR 4916. It has a number of other less frequently used names too, in large part because it is a fairly bright star and as such has been included in the bright star catalogue. It was classified as a γ Doradus type star by Aerts et al. (1998), based on its characteristic variability and spectral type.

It has a V magnitude of 5.23(Fekel et al., 2003). Fekel et al. (2003) found it to have a $v\sin i$ of 115 kms^{-1}, Mathias et al. (2004) found a $v\sin i$ of 101 kms^{-1}, and Abt and Morrell (1995) and Aerts et al. (1998), a $v\sin i$ of 130 kms^{-1}. Whilst agreement on the rate of rotation of the star is poor, what is clear is that it is a rapid rotator likely to have a true $v\sin i$ greater than 100 kms^{-1}. Aerts et al. (1998) reported a temperature of 7190 K and a mass of 1.5 $M_\odot$, which agrees well with Plavchan et al. (2009) who reported a temperature of 7180K and a mass of 1.56 $M_\odot$.

The classification of the spectral type of this target is relatively consistent. Some researchers reported that it is an F0 V (Gray and Garrison, 1989), Fekel et al. (2003) classify the star as a type F1 V, while Abt and Morrell (1995) give a classification of F2 noting it as a metallic line star based on the Balmer series.

Several photometric frequencies have been found for this star. Aerts et al. (1998) found two frequencies in photometric data with periods of $P_1 = 0.4245$ d and $P_2 = 0.4458$ d. Henry et al. (2005) reported five very closely spaced frequencies with periods of $P_1 = 0.42450$ d, $P_2 = 0.44583$ d, $P_3 = 0.40533$ d, $P_4 = 0.39830$ d, and $P_5 = 0.48797$ d. They also showed that these variations were due to pulsations and not due to ellipticity or sunspots. Mathias et al. (2004) noted line-profile variation (LPV) in spectra of this star, but also that most of the variation is to be found in the wings of the profile.

1.6 Motivation and structure

The motivation for this study is to push at the boundaries of the currently available methodology. We wish to develop the best techniques possible to get the most out of our data. These precise data can then be used in a detailed analysis of the frequencies present in the stars and the modes in which the stars are oscillating. These frequencies and modes can then be compared with theoretical models of g-mode pulsations developed by other groups. This is a rapidly developing field, with the notable recent work of the *Kepler* team and others, but a continued dialogue between theoreticians and those from the observational side needs to continue in order to make better progress in this area of research.

This thesis is laid out so this chapter has introduced the reader to some of the topics useful to the understanding of the subsequent material, and to some of the problems likely to be encountered.

Chapter 2 describes the collection of spectra for analysis from the various observatories around the world, and how they were treated in data reduction. Chapter 3 outlines the methods used in the analysis of line profile variations of the these stars, how the line profiles are created, the frequencies are found, and the modes identified. Chapters 4, 5 and 6 are where these techniques and ideas are applied in the detailed analyses of spectral line profile variations in HD 189631, QW Puppis and IR Draconis. Chapter 7 discusses the results of this study, while Chapter 8 provides a overall conclusions of the thesis and includes suggestions for the future direction of this and similar research.

Chapter 2

Data Acquisition

This study required a large number of spectra over a broad timebase to give adequate frequency resolution. The cross-correlation method used however allows for the recovery of a high signal-to-noise (S/N) line profile from a comparatively short-exposure spectrum by combining profiles from a large number of spectral lines. That the periods of pulsation are from 8 hours to around 80 hours means that exposure times of up to 30 minutes are acceptable. Fortunately these long exposures were not needed for line profiles as the three targets examined were fairly bright, but longer exposures were needed for the metallicity analysis.

The utilisation of multi-site data is important because of the 1-day aliasing that can appear in frequency analysis of spectra collected from only one site. If spectra are collected at one site, at night, then that regular nightly pattern will be found in the data. This becomes problematic when the frequencies to be found lie around the $1\mathrm{d}^{-1}$ range as are normal for the g-mode pulsations of γ Doradus stars (see Section 3.3.1).

In the following sections, the data acquisition from the various different sites for the three stars HD 189631, QW Puppis, and IR Draconis, is described. This is followed by an explanation in section 2.4, of the steps in the data reduction to produce wavelength-calibrated, one-dimensional spectra from each site.

Date	Julian Date (JD-2450000)	Observer	Site	Instrument	Obs
Jul 2008	4620-4626	P. De Cat	La Silla	HARPS	272
Jul 2008	4651-4662	P. Kilmartin	MJUO	HERCULES	38
Jul 2008	4660-4667	L. Mantegazza	La Silla	FEROS	56
Aug 2008	4683-4685	K. Pollard	MJUO	HERCULES	7
Jun 2009	5003-5012	E. Poretti	La Silla	HARPS	23
Jul 2009	5028-5031	J.C. Suárez	La Silla	HARPS	25
Jun 2010	5363	P. Kilmartin	MJUO	HERCULES	1
Sep 2010	5455-5458	P. Kilmartin	MJUO	HERCULES	4
May 2011	5703-5712	E. Brunsden	MJUO	HERCULES	28
Jun 2011	5720-5738	P. Kilmartin	MJUO	HERCULES	25
Total					479

Table 2.1: Spectra of HD 189631 collected for analysis in this project. The lower section of the table displays spectra that have not been examined before this work.

2.1 HD 189631 Observations

These data are dominated by the extremely dense observational campaign organised by P. De Cat in 2008 at La Silla Chile (Table 2.1). It was decided that condensing these observations by binning them was a poor idea as the quality of these images is excellent and this would unnecessarily reduce the quality of this work. It does mean than the fitting of frequencies was heavily weighted towards a good fit during this range of dates at the possible expense of fits during other times. The addition of further spectra at later times was expected to moderate this somewhat.

2.1.1 MJUO

Mount John University Observatory (MJUO) is a facility run by the University of Canterbury in the South Island of New Zealand. It is located in New Zealand's recently proclaimed gold status Aoraki Mackenzie International Dark Sky Reserve at 43° 59' 12" S, 170° 27' 54" E and 1029m above sea level (Figure 2.1).

The 1.0m McLellan reflecting telescope is used to gather light to be fed by fibre to the High Efficiency and Resolution Canterbury University Large Échelle Spectrograph (HERCULES). It is capable of a resolving power of up to $R = 82{,}000$ (Hearnshaw et al., 2002) and these spectra are recorded with a 4096x4096 pixel CCD.

Data reduction up to the change of CCD in 2007 was undertaken using the HERCULES reduction software package (HRSP) (Skuljan, 2004). After this date, reduction has been carried out using a collection of scripts in MATLAB (MATLAB, 2011). These scripts allow for intimate customisation of the reduction process for the various needs of the data set. When the HERCULES vacuum-tank is opened, the image of the CCD can shift position slightly. When this happens the MATLAB scripts require some adjustment to enable the location of the Th-Ar standard arc lines for reduction of the associated stellar spectra (Table 2.1).

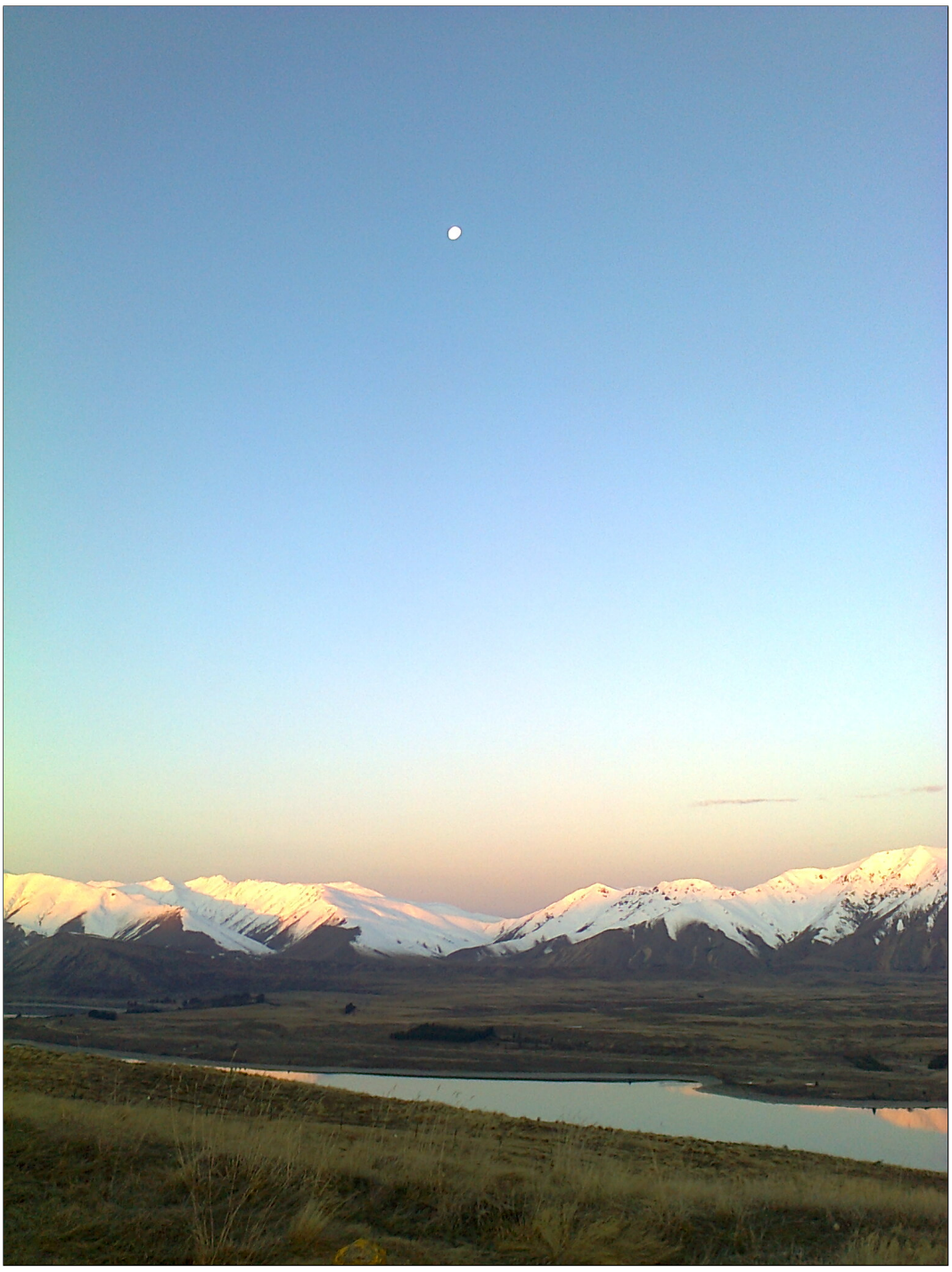

Figure 2.1: At MJUO there is much to see even when just waiting for the dome interior to equilibrate with the outide air for the night.

2.1.2 La Silla

There are two telescopes and spectrographs at the European Southern Observatory in La Silla, Chile that were used to observe HD 189631. The High Accuracy Radial velocity Planet Searcher (HARPS) spectrograph mounted on a 3.6m telescope gives a resolving power of 115,000, and the Fibre-fed Extended Range Optical Spectrograph (FEROS) on the 2.2m telescope has a resolving power of 48,000. They are located at 29° 15' 40" S, 70° 43' 54" W at an altitude of 2400m.

Observations were obtained during July-August 2008 and June-July 2009 (see Table 2.1) by various observers. These spectra were provided to the author in the form of wavelength calibrated but unnormalised spectra.

Date	Julian Date (JD-2450000)	Observer	Site	Instrument	Obs
2004					
7 - 9 Feb	3409-3411	D.J. Wright	MJUO	HERCULES	18
28 Feb - 4 Mar	3430-3434	D.J. Wright	MJUO	HERCULES	12
29 Mar - 3 Apr	3460-3464	P.M. Kilmartin	MJUO	HERCULES	27
23 Mar - 3 Apr	3452-3464	D.J. Wright	SAAO	GIRAFFE	122
2012					
27 - 30 Jan	5953-5957	P.M. Kilmartin	MJUO	HERCULES	52
2 - 7 Feb	5960-5967	M.W. Davie	MJUO	HERCULES	98
15 - 21 Mar	6002-6008	P.M. Kilmartin	MJUO	HERCULES	73
9 - 11 Jun	6088-6090	M.W. Davie	MJUO	HERCULES	66
21 - 24 Jun	6100-6104	P.M. Kilmartin	MJUO	HERCULES	20
24 - 27 Jul	6104-6107	M.W. Davie	MJUO	HERCULES	12
24 - 29 Aug	6164-6169	M.W. Davie	MJUO	HERCULES	68
30 Aug - 4 Sep	6170-6176	P.M. Kilmartin	MJUO	HERCULES	17
Total					585

Table 2.2: QW Puppis observations from SAAO and MJUO in 2004 and 2012.

2.2 QW Puppis Observations

QW Puppis was the major southern-hemisphere target for this study.

2.2.1 MJUO

Many of the initial 179 observations were collected at SAAO and MJUO by Dr. Duncan Wright from February to April 2004 (Wright, 2008). Several additional observation runs at MJUO were carried out in 2012 as shown in Table 2.2. QW Puppis is ideally a summer target, but is still visible in midwinter, setting about an hour after dusk at the June solstice.

2.2.2 SAAO

The GIRAFFE spectrograph gathers light from the fibre-feed from the 1.9m Radcliffe telescope, which is located at the South African Astronomical Observatory (SAAO) at Sutherland (32° 22' 41.88" S 20° 48' 37.8" E), and 1750m above sea level. GIRAFFE has a resolving power of $R = 39200$, limited by the size of the fibre-feed optical core.

122 Spectra were obtained at SAAO over March and April 2004 and these spectra were re-reduced from the original FITS files for this thesis.

2.2.3 MJUO

During Feb-April 2004, 57 spectra of QW Puppis were obtained at MJUO and reduced using HRSP (Skuljan, 2004). A further campaign on QW Puppis during 2012 meant an additional 406 spectra were obtained.

Date	Julian Date (JD-2450000)	Observer	Site	Instrument	Obs
2008					
11 Dec	4812	S. Yang	DAO	9682M	1
11 Dec	4812-4818	P. De Cat	McDonald	SES	32
2009					
6 - 11 Mar	4896-4901	E. Kambe	OAO	HIDES	165
7 - 15 Mar	4897-4905	D.J. Wright	La Palma	HERMES	36
9 Mar	1898-4899	S. Yang	DAO	9682M	4
10 - 16 Apr	4931-4937	H. Lehman	La Palma	HERMES	74
24 Apr	4945	R. Østensen	La Palma	HERMES	4
10 May	4961	G. Gentile	La Palma	HERMES	12
23 - 25 May	4974-4976	S. Yang	DAO	9682M	29
30 May	4981	M. Joos	La Palma	HERMES	4
8 - 14 June	5020-5026	P. De Cat	McDonald	SES	37
10 - 11 Jul	5022-5023	S. Yang	DAO	9682M	3
10 - 16 Jul	5022-5028	D.J. Wright	OHP	SOPHIE	90
30 Jul - 1 Sep	5042-5045	H. Lehmann	Tautenburg	Échelle	15
25 - 27 Sep	5100-5102	H. Lehmann	Tautenburg	Échelle	40
4 Oct	5109	A. Tkachenko	Tautenburg	Échelle	11
1 Nov	5137	S. Yang	DAO	9682M	5
2010					
23 - 27 Jan	5219-5224	C. Waelkens	La Palma	HERMES	82
Total					644

Table 2.3: IR Draconis observations from the multi-site campaign.

2.3 IR Draconis Observations

Dr. Peter De Cat (Royal Observatory of Belgium) and Dr. Duncan Wright (University of New South Wales) are members of a small working group (along with Prof. Peter Cottrell, Dr. Karen Pollard, Emily Brunsden, and myself) to study the pulsational characteristics and behaviour of γ Doradus stars. Being based in the northern hemisphere, Dr. De Cat was fortunate to obtain observing time on a range of telescopes and spectrographs able to observe IR Draconis.

2.3.1 HERMES

The High Efficiency and Resolution Mercator Echelle Spectrograph (HERMES) was built for the 1.2m Mercator telescope (Figure 2.2) located at Roque de los Muchachos Observatory on La Palma Island (Canary Islands, Spain) (at 2333m above sea level, 28° 45' 44" N, 17° 52' 42" W.) in the Canary Islands. It is the result of a collaboration between Belgian, Swiss and German interests. It is capable of resolving powers between R = 40,000 and 90,000 dependent on slit width, and focuses onto a 2048x4608 pixel CCD. The spectra are reduced on site in an automated fashion by the HERMESDRS software package.

A total of 212 IR Draconis spectra were collected and reduced on site to a wavelength-

Figure 2.2: The Mercator telescope dome on La Palma. It is found at 2333m above sea level, at 28° 45' 44" N, 17° 52' 42" W.

merged barycentric-corrected state.

2.3.2 OAO

The Okayama Astrophysical Observatory (OAO) is found on Mt. Chikurin-Ji, Japan (34° 34' 37.47" N, 133° 35' 38.24" E) at 372m above sea level. The 1.88m telescope is equipped with the HIgh Dispersion Échelle Spectrograph (HIDES). It is capable of a resolving power of $R = 65{,}000$ with a 0.76" slit (theoretically up to 100,000 with an 0.38" slit) and focuses to a 2048x4096 pixel CCD.

165 spectra were obtained in March 2009 and reduced and partially order-combined on site using IRAF software to three sub-spectra each. The ranges of the sub-spectra received were 3926Å — 5071Å, 5210Å — 6324Å, and 6512Å — 7605Å.

2.3.3 SOPHIE

SOPHIE (named from Spectrographe pour l'Observation des Phénoménes des Intérieurs stellaires et des Exoplanétes) is a high resolution échelle spectrograph located at l'Observatoire des Haute-Provence (OHP) between Marseille and Grenoble, France. It is found at 43° 55' 51" N, 5° 42' 48" E, at 650m above sea level. The 1.93m telescope is connected by fibre-feed to the spectrographic unit, and gives a spectral resolution of up to $R = 75000$ (see Figure 2.3).

Between July 10-16, 2009, 90 spectra were obtained and were reduced, barycentric-corrected and order-merged on site in an automated system.

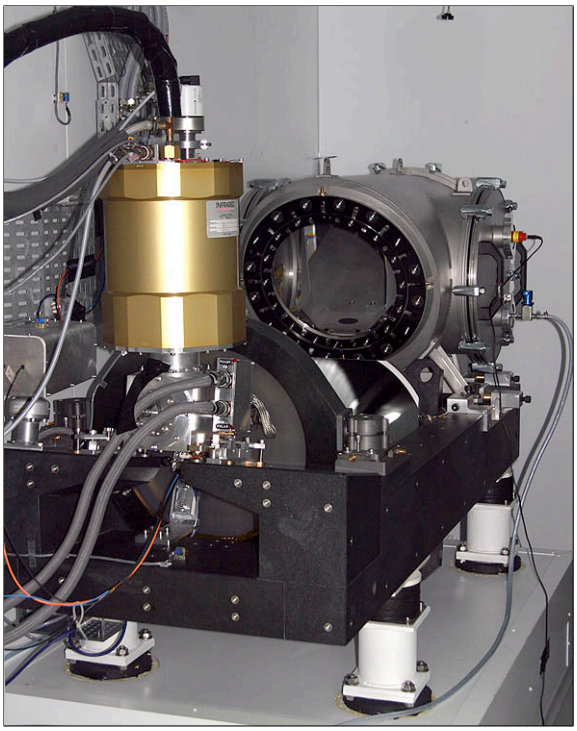

Figure 2.3: The SOPHIE unit without its cover. The brass cylindrical dewar is the cryostatic unit housing the cooled 4096x2048 pixel CCD.

2.3.4 Tautenburg

The Karl-Schwarzschild-Observatorium near Tautenburg, Germany is found at 50° 58' 48.4" N, 11° 42' 40.2" E at 341m above sea level (Figure 2.4). The 2.0m Alfred-Jensch Teleskop was used to collect the spectra obtained for this work. The échelle spectrograph is capable of a resolving power of up to $R = 67{,}000$ with a 1.2" slit width.

IR Draconis spectra were collected over three observing runs in 2009 (see Table 2.3).

2.3.5 McDonald Observatory

Located in western Texas, USA at 30° 40' 53.2" N, 104° 00' 53.0" W, and an altitude of 2070m, is the McDonald Observatory. The McDonald 2m Otto Struve Telescope was used with the Sandiford cassegrain Échelle Spectrometer (SES) to obtain 69 spectra over two observing runs (see Table 2.3). These spectra were reduced on site using the ESO's MIDAS software package into a number of sub-files for later re-combining. This number of spectra is such that a representative mean spectrum over the pulsational period was not be obtainable; these spectra were excluded from the data set as a result.

Figure 2.4: The 2.0m Alfred-Jensch-Teleskop, Tautenburg, open at night. One can see the constellation Orion above it.

2.3.6 DAO

The Dominion Astrophysical Observatory (DAO) is found southwest of Vancouver B.C., Canada, at 48° 31' 13.03" N, 123° 25' 5.33" W. The DAO's 1.2m telescope was used to collect spectra with the McKellar high-resolution 9682M spectrograph. The spectrograph is focused onto a 4096x2048 pixel CCD where they are collected and recorded as FITS files.

Over December 2008, and March, May and July of 2009 a total of 42 long-slit stellar spectra were obtained by Peter De Cat along with several Fe-Ar spectra for wavelength calibration. These were all bias subtracted and flat-fielded before being used for this study. One feature of these data, however, is that there is a restricted wavelength range, meaning that fewer spectral lines were available for cross-correlation leading to a lower S/N ratio in the line profiles generated from these spectra. For 41 of the spectra obtained the wavelength range is 4451Å to 4596Å. One of the spectra (collected on the 11th of December 2008) was of a different wavelength range (6054Å to 6191Å) and this was discarded from the data set.

The spectra were initially reduced on site by Stephenson L.S. Yang and the wavelength calibration was subsequently carried out by Peter De Cat using the MIDAS software package. Normalisation and barycentric correction had not been carried out on these spectra when the data were received.

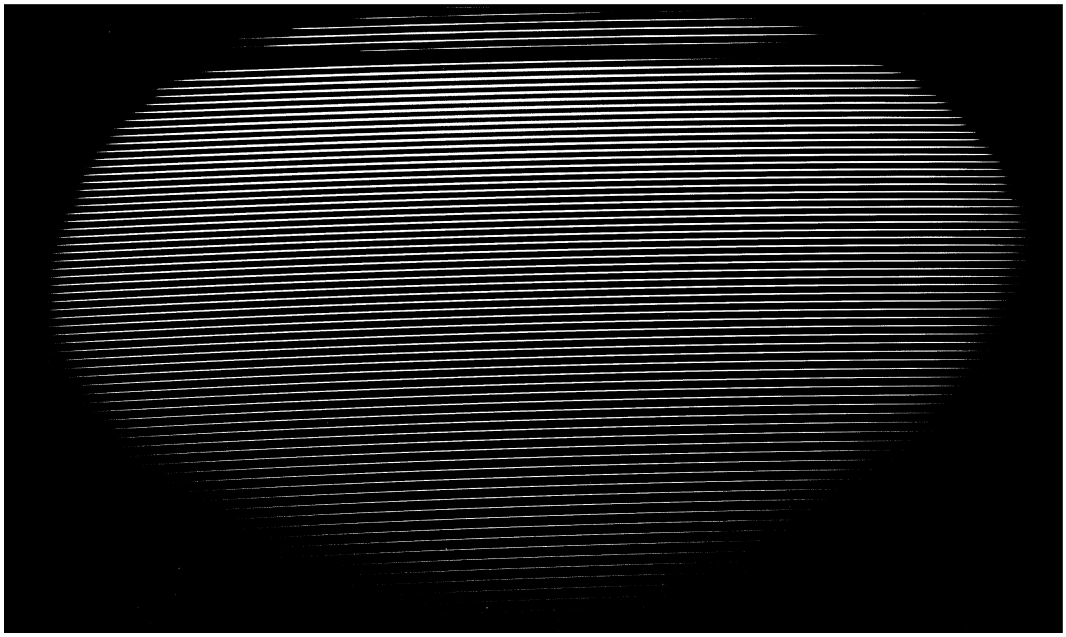

Figure 2.5: A sample échelle spectrum for a white lamp with a one second exposure time. This spectrum was taken with HERCULES at MJUO in June 2012.

2.4 Data Reduction

2.4.1 MJUO spectra

Preliminary data reduction for the 2004, and 2008-2009 MJUO observation sets was carried out prior to this work. The process for this was relatively similar to the data treatment of the other spectra from the site.

The processing of the HD 189631 spectra was carried out in several subsets. The MJUO spectra for HD 189631 from the HERCULES was broken into three subsets to allow for the limitations of MATLAB's RAM allocation. The MJUO data from 2004 was treated as one set, and those spectra from 2007 and 2008 as the other two data sets.

Several short-exposure flat field images were taken at the start of each night's observations (see, for example Figure 2.5), which were then summed to obtain sufficient S/N. The locations of the échelle orders on the image are traced from this and the data were extracted. The background was then extracted and the pixels affected by cosmic rays were located and adjusted.

The Th-Ar spectra (see, for example Figure 2.6) were then extracted along the found orders and corrected for any cosmic rays. These spectra were then compared to a list of known lines to assign a wavelength scale. For most of these Th-Ar spectra, between 900 and 1100 spectral lines were found for wavelength calibration.

The stellar spectra (Figure 2.7) were then extracted along the orders and corrected for cosmic rays. As these exposures are longer, there are usually many more pixels with cosmic ray defects than for the calibration spectra. The cosmic ray correction was done in two stages: an initial correction; and a later smoothing operation during continuum normalisation (see Figure 2.8).

Synthetic spectra were generated using SYNSPEC (Hubeny and Lanz, 2011) using the best available estimates of the model parameters for each star (Table 2.4). Continua were fitted and a second cosmic ray smoothing applied to spectra to remove points greater

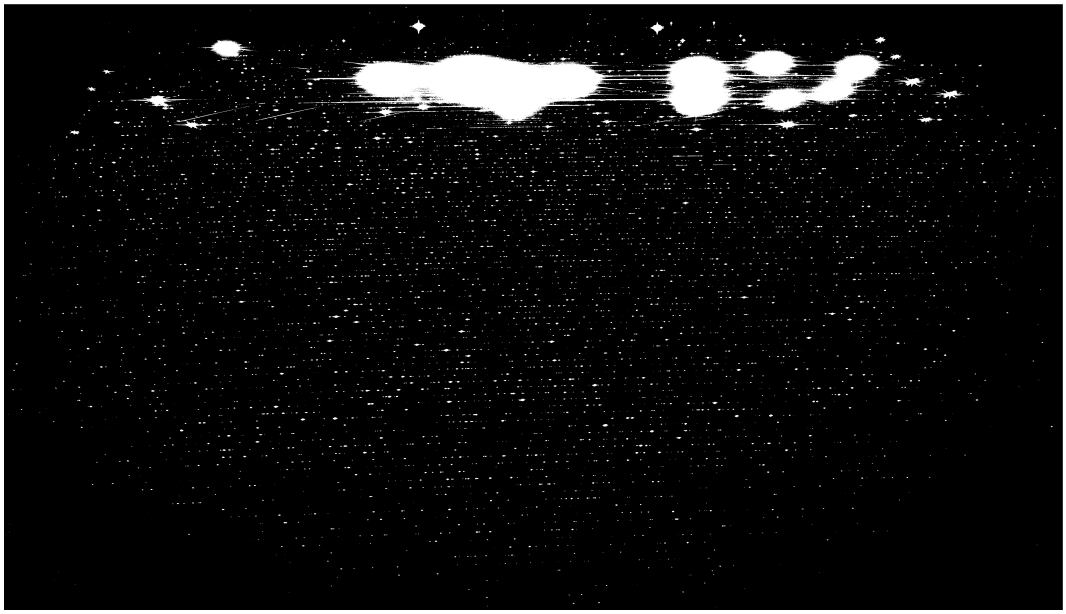

Figure 2.6: A sample échelle spectrum for a Th-Ar lamp with a ten second exposure time. The distinct lines here were used to calibrate the wavelength scale for the stellar spectra.

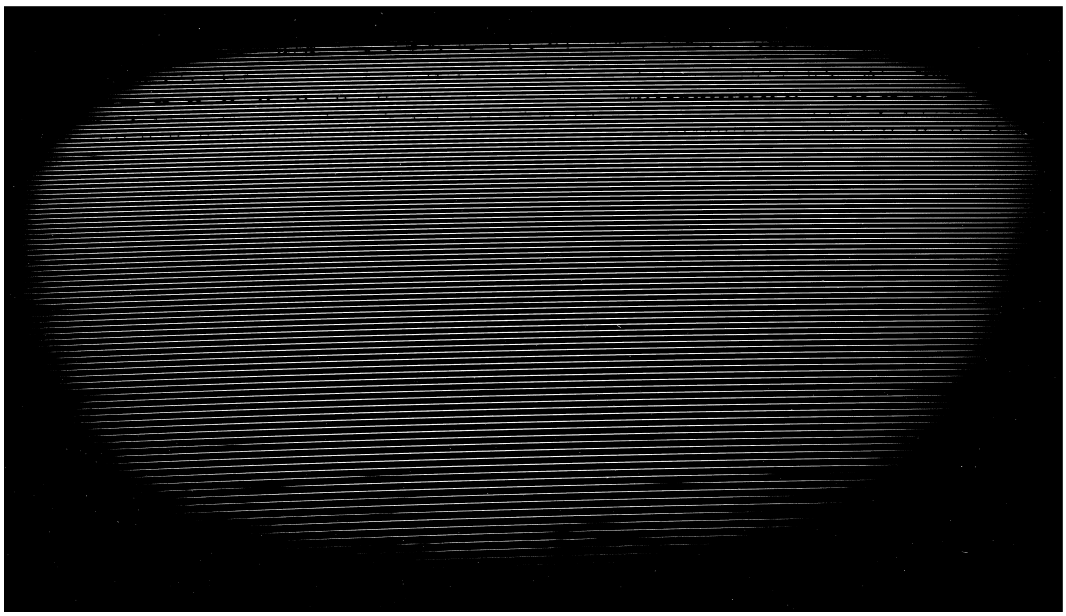

Figure 2.7: A sample spectrum for QW Puppis taken on 11 June 2012. Some of the strong absorption lines are visible.

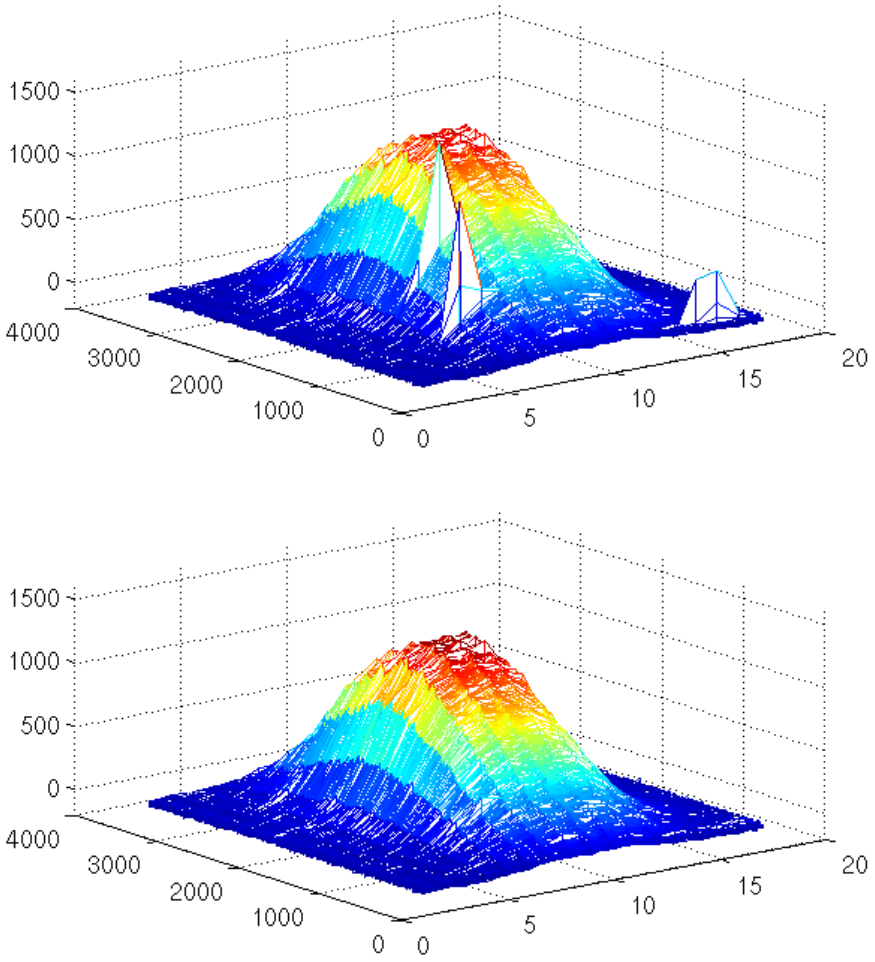

Figure 2.8: Cosmic ray removal during the initial steps of data reduction for QW Puppis. The two horizontal axes are in pixels of the CCD used to capture the image. It can be seen that the order (order number six) is less than twenty pixels wide but around 3500 long. These cosmic rays do not usually affect the whole width of the order but, with a long enough exposure, their incidence is greatly increased. It is seen that the cosmic ray removal and correction is not perfect, with some small remnant remaining, but is later smoothed when reduced to a one dimensional intensity array.

	QW Puppis[a]	HD 189631[b]	IR Draconis
T (K)	7400	6900	7180[c]
log$g$	4.2	4.05	4.01
$v\sin i$	51	43.6	101[d]
σ	0.5	0.5	0.5
Wavelength (Å)	3800 — 8000	3800 — 8000	3800 — 8000
Shift (kms^{-1})	-0.8	-10.13	-8.7[e]
$[Fe/H]$	-1.0	0.08	-0.14

[a]Wright (2008)
[b]Maisonneuve (2010)
[c]Plavchan et al. (2009)
[d]Mathias et al. (2004)
[e]Fekel et al. (2003)

Table 2.4: Parameters used with SYNSPEC to create synthetic spectra for continuum fitting during data reduction.

than 5σ away from the mean. The échelle orders were then merged together using cubic spline interpolation and normalised. HRSP trims the noisy edges of the orders leaving gaps between them when merged (Figure 2.9).

2.4.2 HARPS and FEROS spectra

The spectra from both La Silla spectrographs were initially reduced on site. They were then reformatted to a state where they could be processed using the same set of procedures as the MJUO data. Barycentric corrections were made later, as described in Section 2.4.1. Similarly continua were fitted, orders merged and spectra normalised in a manner similar to that of the MJUO spectra.

The spectra from HARPS are of an exceptional quality compared to the other sites for HD 189631, as would be expected given the high resolution spectrograph coupled with the comparatively large telescope.

2.4.3 SAAO spectra

Reduction of SAAO spectra was carried out initially by Duncan Wright for his PhD thesis work (Wright, 2008). In this work, the separate orders were taken and re-reduced and merged to ensure consistent methodology.

Some hurdles were encountered in dealing with these and other archival data sets. The formats in which they were stored were unusual, and the state of processing was poorly annotated. The major problem was that the intial FITS formatted files had been deleted and the post-processed data were kept. These, however, did not retain the FITS file headers which contain the observational parameters, including the Julian Date of observation. This lack of the observation time for the spectra caused delays in the processing of these data until the original files could be acquired. From the dates and exposure times in the FITS headers Julian Dates were generated and the barycentric correction performed on each spectrum. The Julian Dates used were the Julian Date at the midpoint in each exposure taken from the available information in the archived FITS header. Similar to the process for reduction of MJUO spectra (Section 2.4.1), a rough normalisation was carried out and

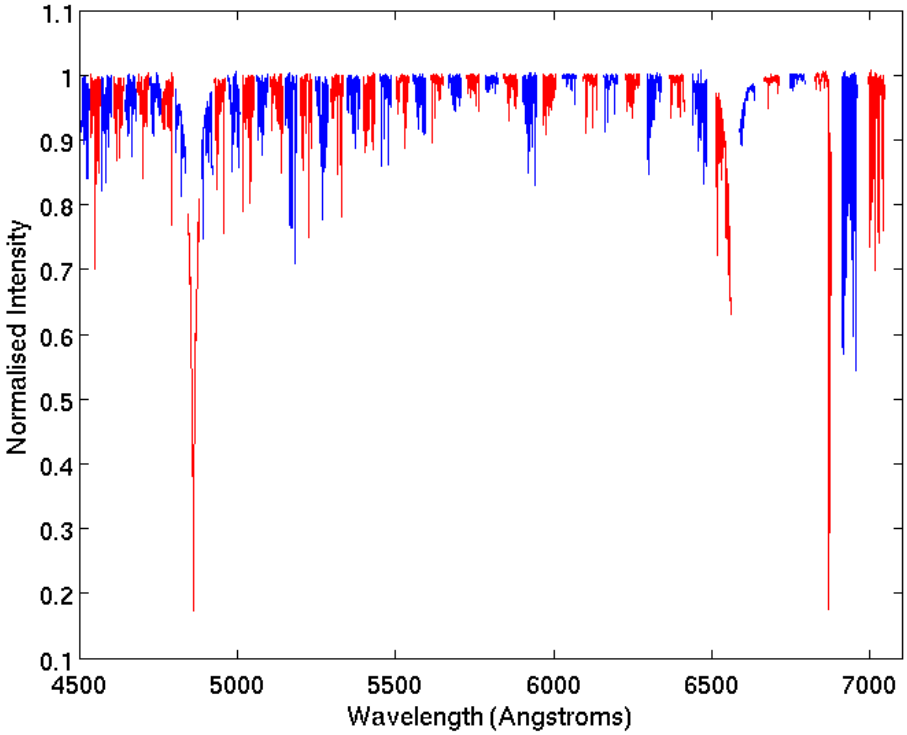

Figure 2.9: Here the gaps between the orders left by the HRSP data reduction package are seen clearly. The colours are alternated to see each order with greater clarity. In the creation of cross-correlated line profiles the Hα and Hβ lines and telluric regions are excised (see section 3.1).

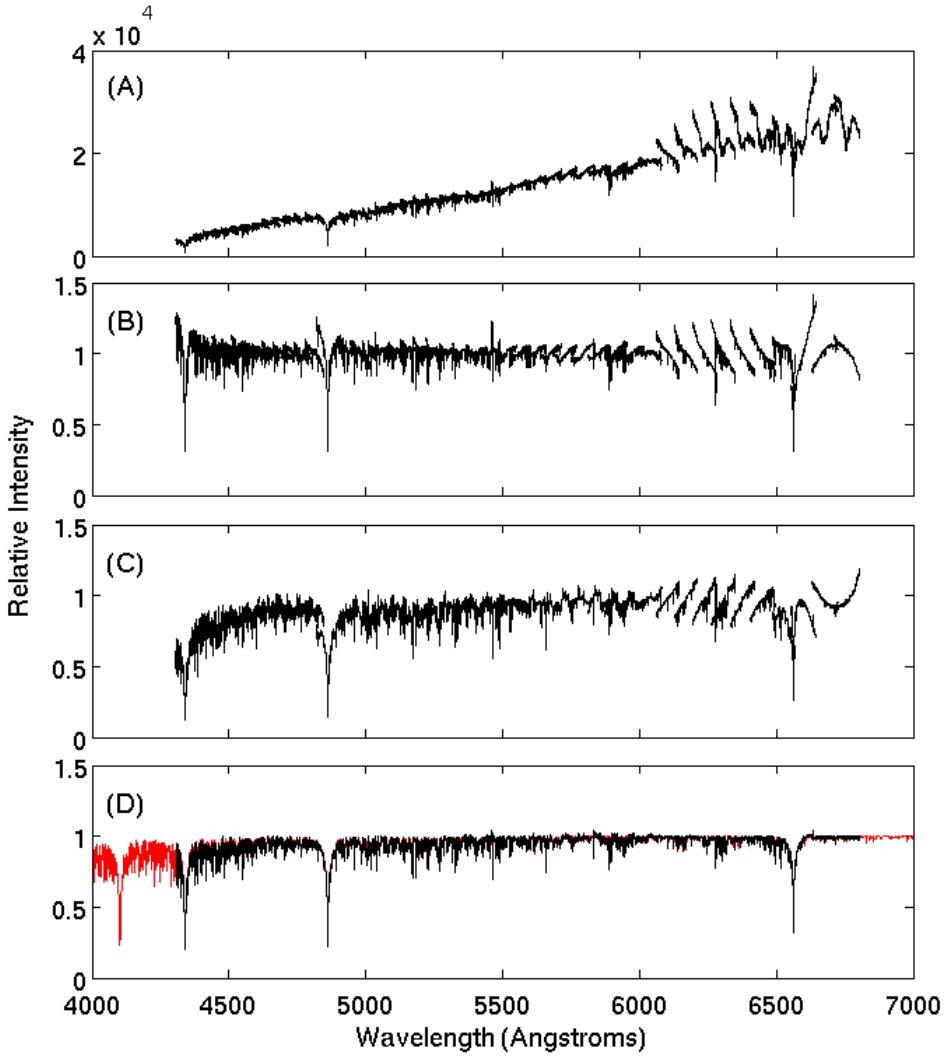

Figure 2.10: A summary of the reduction stages for the set of SAAO spectra. (A) The mean of the raw orders plotted with their assigned wavelength scales after barycentric corrections were carried out. (B) Medians of each roughly normalised order. (C) After continuum fitting was carried out using the median of each order. (D) Normalised, order-merged, cosmic ray removed spectra. The red line is the synthetic spectrum calculated for the star using the parameters set out in Table 2.4 and SYNSPEC.

again continua were manually fitted for normalisation. These were done using the median spectrum and not the mean spectrum as previously owing to the larger variability in these GIRAFFE spectra than for other data sets.

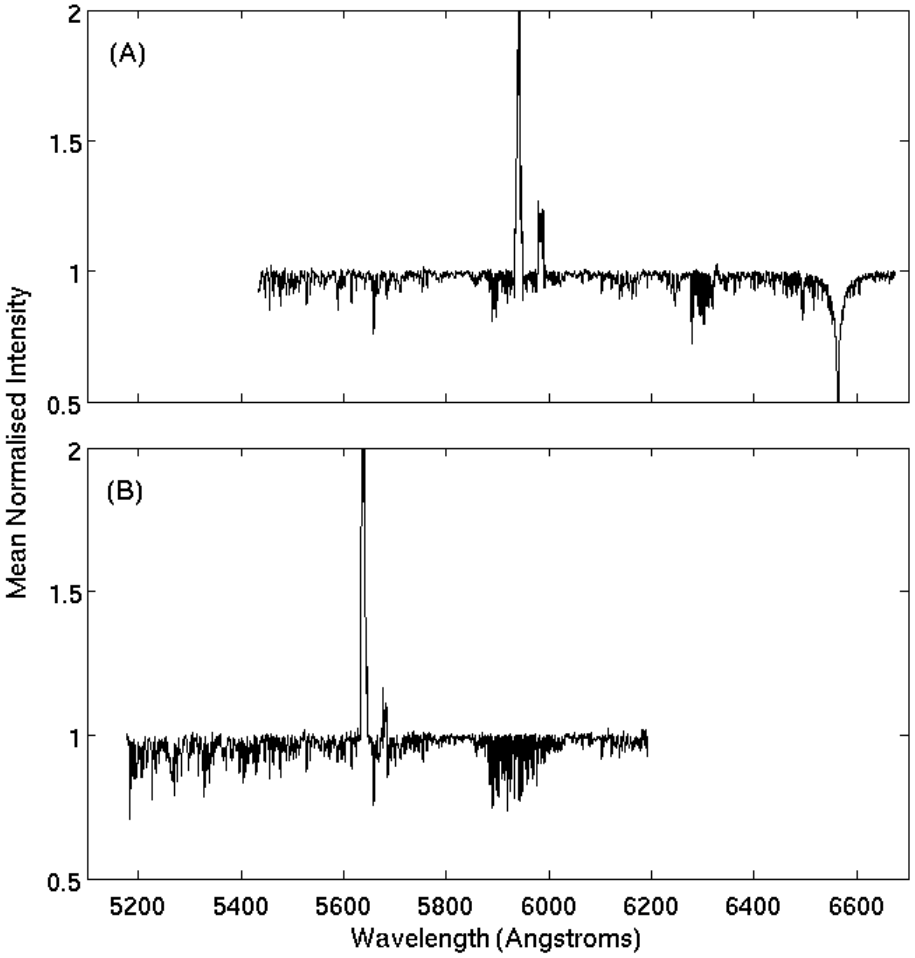

Figure 2.11: The two different wavelength ranges from the sets of McDonald data. (A) Mean spectrum from December 2008 (showing the Hα line) and (B) from June 2009. Notable is the abberant spike in the middle of each set of data (see text for more detail).

2.4.4 McDonald spectra

The spectra from the McDonald Observatory were obtained over two observing runs separated by about seven months. It was quickly apparent that these sets of spectra showed some notable differences. The two different groups of data had different ranges of observed wavelength (Figure 2.11). This meant that the two sets had to be reduced, continuum-fitted and order-merged separately.

The spike shown in the data in Figure 2.11 is of interest because it appears at different wavelengths in each set, but is consistent between the observations within each set. The feature moves with the shift in wavelength scale, leading to the belief that it is chip or spectrograph related. It led to some considerable problems in the post-continuum fitting order-merging step as the feature extended past the edge of an order (Figure 2.12), well above the continuum level and the splining operation to fit the orders together had some difficulty in merging and normalisation of these data.

Continuum fitting was redone for each set and the features at elevated levels treated as continua, thereby removing them from the finalised spectra. However owing to the

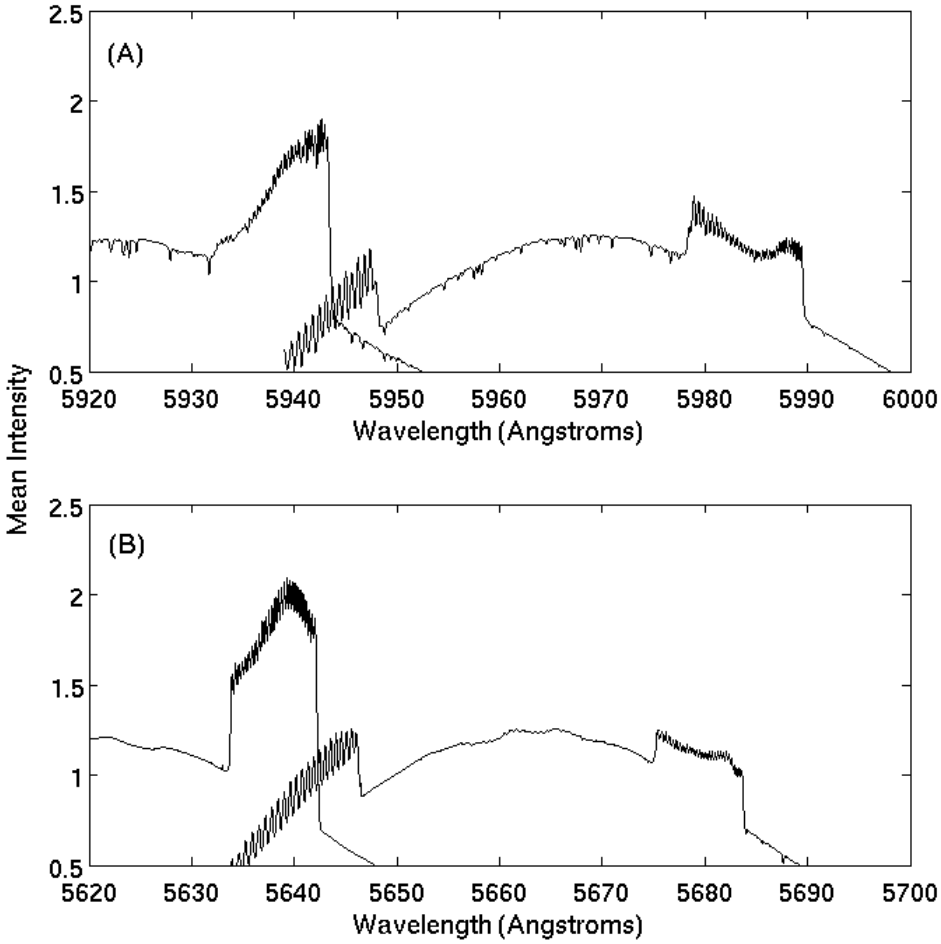

Figure 2.12: Orders 129 and 130 from the 2008 data set (A) and orders 136 and 137 from the 2009 data (B). The strong feature at the shorter wavelength end of the right hand order continues to the edge of the order in both cases. Note also that these features, whilst similar, appear at different wavelengths in the different data.

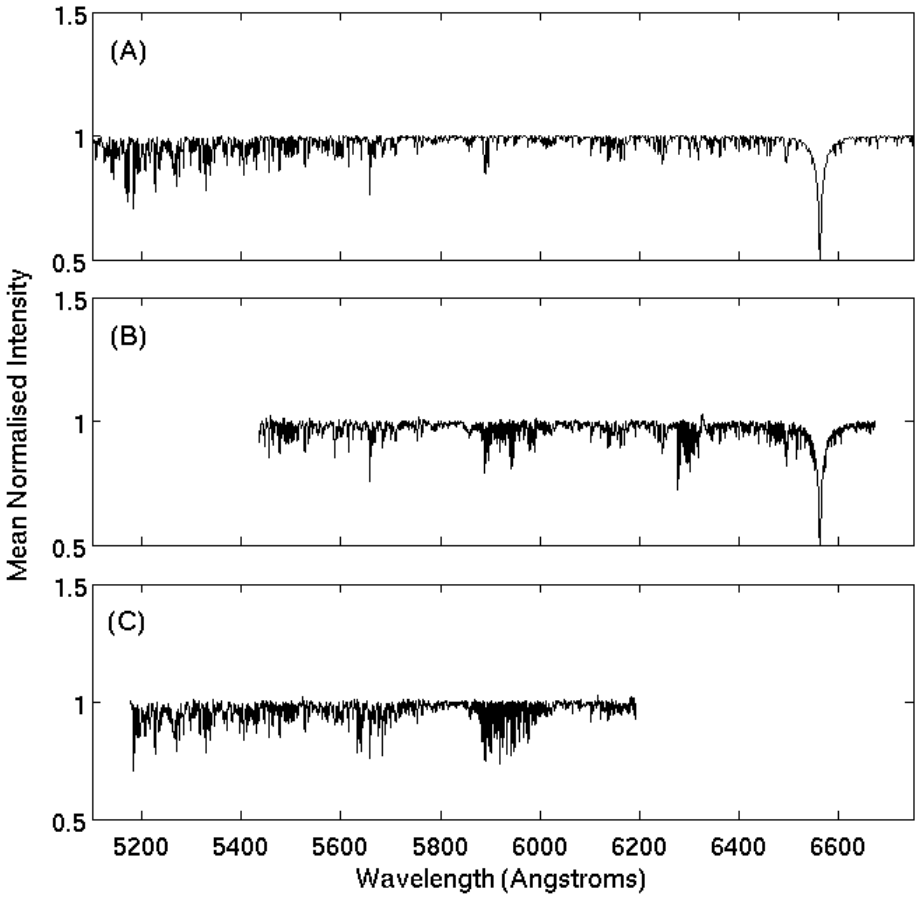

Figure 2.13: Synthetic spectrum (A) from SYNSPEC using parameters for IR Dra from Table 2.4. McDonald Observatory 2008 data (B), 2009 data (C). The McDonald data are shown prior to telluric and Hβ line removal and filling the empty wavelength ranges. The remnants of the approximately normalised features may still be seen at *ca.* 5940Å (B) and 5640Å (C). Removal of these ranges of wavelength will further reduce the number of spectral lines available to have their profile variation analysed.

significantly higher counts over these regions more noise is also apparent. Most of these regions will be removed prior to the generation of cross-correlated line profiles as they include telluric lines and very little signal in these orders (Figure 2.13) . The McDonald spectra were considered together in the forming of a single mean spectrum for the creation of a cross-correlated profile. This was possible by treating the different data sets together and where data were absent, a constant normalised intensity of one was set.

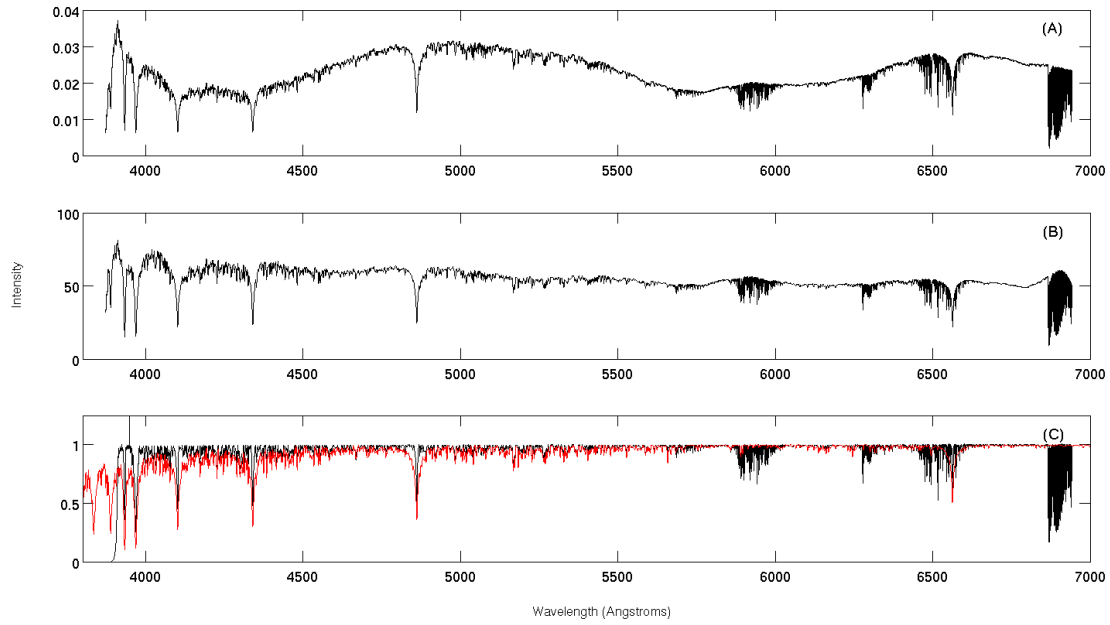

Figure 2.14: Summary of steps in the reduction of Sophie spectra. In black are mean spectra, and in red is a synthetically generated spectrum. (A) Mean received spectrum. (B) The spectra were broken into 25 artificially created orders from the received spectra. The spectra were cosmic-ray corrected and a low-order polynomial normalisation to mitigate inter-observational intensity variation. (C) Continuum fitted and normalised mean spectrum.

2.4.5 SOPHIE spectra

The 90 spectra obtained at the OHP were wavelength calibrated and order merged on site in an automated fashion. Whilst liberating some high-quality spectra this is not ideal for the method applied in the analysis of these data (Chapter 6). These spectra were not received in individual orders, so were broken into 25 artificially created orders for continuum fitting by hand and this continuum fit was applied to the whole spectrum. Using a $v\sin i$ of 110 kms^{-1} gave synthetic spectra that fit well the mean spectrum during the continuum fitting.

Given the wavelength scale ($\approx$ 308000 data points) the memory needed for calculation of the arrays for the line-profile generation would limit the wavelength scale to $\approx$ 17000 data points. The final normalised spectra were broken into twenty orders for creating the line profiles.

2.4.6 HERMES spectra

HERMES spectra were received as very complete spectra similar to those of HARPS and FEROS. They were wavelength calibrated and required little additional processing apart from continuum fitting and normalisation. A notable feature of these spectra when compared to those from the other sites that observed IR Draconis is their extended wavelength range. Having a wavelength range from just over 3760Å to over 9000Å many good isolated lines are available past the telluric lines to the red end of the spectrum. That these spectra cover a reasonable range of dates is good for the analysis but they were obtained by many different observers. Not all observers collected spectra in the same way and for some headers fields were missing. Not all spectra had Julian dates recorded, this was calculated

from the observation midpoint as a best approximation. Given the observation length a difference from the count-weighted mean exposure time would be relatively small.

2.4.7 HIDES spectra

Each spectrum from the OAO was received as three files and a log file with information on each spectrum. The log file contained date, time and exposure length information and from these Julian Dates were created at the midpoint of the exposure for each spectrum. These spectra were stored as a number of echelle orders concatenated together after wavelength calibration using the IRAF package using Th-Ar spectra. These orders needed to be separated before further data treatment could proceed. The seventy orders were each continuum fitted manually before normalisation. The significant overlap between orders enabled several independent observations of a few lines.

2.5 Summary

This chapter has summarised the different datasets obtained at the various observatories and instrumental setups for the three stars studied in this thesis: HD 189631, QW Puppis and IR Draconis. The basic reduction steps required to get each dataset to wavelength-calibrated, continuum-normalised one-dimensional spectra for further analysis has been presented. The following chapter will describe further analysis of these spectra to enable a detailed line profile study.

Chapter 3

Data Analysis Methods

Drawing precise information from data is no mean feat for something so foreign as a distant star. The variation of the stellar surface as it exhibits one or more non-radial pulsations is borne in the morphology of the lines in its spectrum. As a pulsation causes a ripple on the stellar surface, this particular velocity profile is carried by the spectrum, superimposed on the spectral lines received at a spectrograph.

It has been shown that the line profile variation is reasonably consistent across different lines and absorbing species in these A – F dwarf stars (Wright, 2008). Non-radial pulsations are, unfortunately, small in radial amplitude as the name suggests, and in order to extract high signal-to-noise (S/N) measurements of the variation over time, the variations of many lines are examined together using a cross-correlation technique.

3.1 Cross-Correlated Line Profiles

Forming a cross-correlated line profile for each observation is a way of greatly increasing the signal-to-noise level in the line profile to be examined. Rather than examining the variation of a single line over time, a cross-correlated line profile is formed combining the variation of many lines.

For each star, a synthetic spectrum was created using the best stellar parameters available (Table 2.4) using the program SYNSPEC. From this spectrum, the spectral line locations and equivalent widths were determined. After removal of weak (equivalent width $<$ 0.5 mÅ) lines from this list, a delta-function mask was created, with delta-functions placed at the central wavelength of each line and scaled in height by their equivalent widths. This scaling effectively weights the subsequent cross-correlation by the strength of the line and so by the amount of signal (Wright, 2008). This delta-function mask could in theory be as readily created from the mean of a well-sampled set of stellar spectra, but until the star is analysed, whether or not a pulsational phase is well-sampled is unknown.

The synthetically created delta-function mask was then cross-correlated in Matlab with each stellar spectrum using the XCORR function giving a high S/N line profile for each stellar spectrum. Using the (flux-weighted) mean Julian Date as the timebase for these line profiles, frequency and mode identification of these proceeded using the packages FAMIAS and SIGSPEC.

This approach makes a number of assumptions. It assumes the veracity of the independence of pulsational behaviour from both absorption species and depth of line formation in the stellar atmosphere. It also assumes that observed frequencies are stable over long periods, or, at least, the timespan of the observations.

3.2 Least Squares Deconvolution

New to this work was the implementation of a least-squares deconvolution (LSD) method for determining a representative line profile for analysis. This method was employed in the analysis of spectra from QW Puppis and IR Draconis.

With the cross-correlation function (Section 3.1), the δ-function line mask is cross-correlated with the obtained spectrum. A limitation of the cross-correlation method is blended lines. If a blended line is cross-correlated with the δ-function mask there will be signal detected where, if unblended, there would be none. Whilst one could select *only* unblended lines for the δ-function mask, this would seriously reduce the number of available lines in A – F stars thereby reducing the S/N of the combined line profile, the very thing that this method is designed to maximise.

For rapidly rotating stars, the incidence of blended lines increases with increasing rotation (Equation 1.9). The LSD method was devised from a combination of the works of Donati et al. (1997) and Barnes et al. (2012), and the assistance of D.J. Wright during a short visit in November 2012.

Barnes et al. (2012) used the method to study radial velocities for planet-searching, but were reasonably full in the description of their method. Much of the following is taken from Barnes et al. (2012).

If the observed spectrum is denoted o_j, and the deconvolved profile elements p_k, then the observed spectrum may be described as

$$o_j = \sum_k \alpha_{jk} p_k \quad , \tag{3.1}$$

where α_{jk} is a j by k matrix contructed using the line depths d_i and the piecewise triangular function $\Lambda(x)$ (Equation 3.3):

$$\alpha_{jk} = \sum_i d_i \Lambda(x) \quad , \tag{3.2}$$

$$\Lambda(x) = \begin{cases} 1+x & : \quad -1 < x < 0 \\ 1-x & : \quad 0 < x < 1 \\ 0 & : \quad \text{elsewhere} \end{cases} \quad , \tag{3.3}$$

$$\text{where } x = \frac{\upsilon_k - c\left(\frac{\lambda_j - \lambda_i}{\lambda_i}\right)}{\Delta\upsilon} \quad , \tag{3.4}$$

υ_k here is the radial velocity of the line profile bin k, c is the speed of light, λ_j is the wavelength of spectrum pixel j, λ_i is the wavelength of line i and $\Delta\upsilon$ is the velocity increment desired in the deconvolved profile.

The calculation of α_{jk} is computationally intensive and, even when written in a parallelised loop, takes quite some time for a large data set. By parallelising this step, the deconvolution time was reduced by 55 percent moving from a single processor to five. For the 2012 HERCULES data set, this resulted in a reduction from 42 hours to 18 hours of processing. This, however, was the single largest group of spectra from one site.

If O contains the observed spectrum in a normalised and continuum-subtracted state, and as told by Barnes et al. (2012) "inverse variances ... are contained in the vector, V", then the LSD profile should be obtained by solving the following:

$$p = (\alpha^T V \alpha)^{-1} \alpha^T V O \tag{3.5}$$

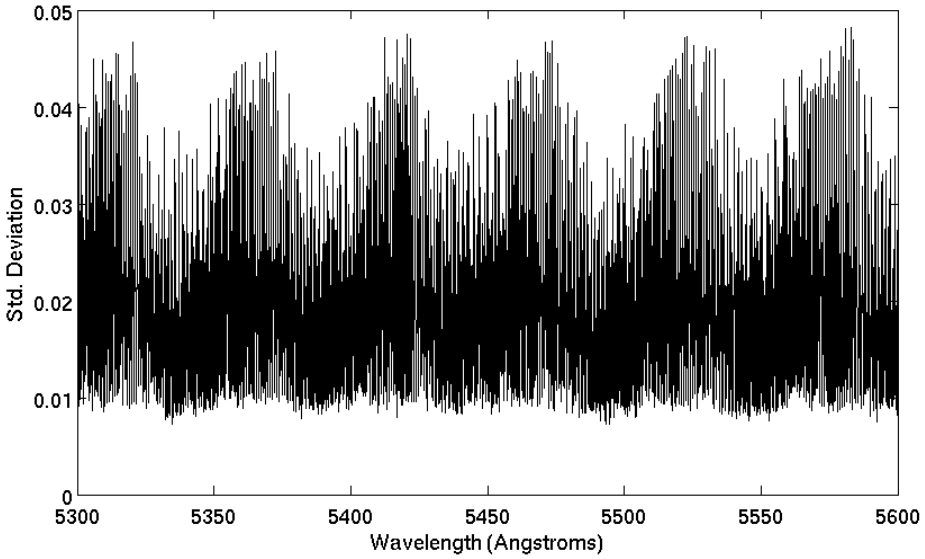

Figure 3.1: The standard deviation of a sample of order-merged QW Puppis spectra from HERCULES. It is seen that merging orders gives rise to undesirable variance in spectra where the ends of orders are fitted together.

.

The problem with this is that, on inspection, this does not work. The above will not multiply satisfactorily as V needs to be a square matrix, not a vector quantity. In this work V was calculated as a diagonal matrix, the non-zero elements of which were the inverse variances $1/\sigma_j^2$ described as S^2 in Donati et al. (1997). The Matlab implementation of this method may be found in Appendix A.

This method is intended to give a much cleaner deconvolved line profile than the cross-correlation method, with greater utility when applied to fast-rotating stars ($v\sin i$ >160 kms^{-1} (Donati et al., 1997)), such as IR Draconis.

The prior cross-correlation method was carried out using fully order-merged spectra. The LSD method described here was written to operate on each échelle order before order-merging occurred. This was done for several reasons. At the end of each order there is a region of relatively low photon-count and so low S/N. When merged together, the two regions of low S/N from each adjacent order give a large standard deviation over many observations, a deviation not arising from line profile variation but rather an undesirable artifact of data treatment (see Figure 3.1). In processing each order separately, there is also the opportunity to get more than one observation of a line in regions of overlap. These observations are independent measurements of these lines and may be treated as such, further increasing the number of lines sampled. Computing the LSD profiles from orders separately also has the benefit of allowing the data to be more easily manipulated by keeping the array sizes manageable.

These LSD profiles from each order were then combined in quadrature to give a single weighted LSD profile for each échelle spectrum obtained.

3.3 FAMIAS - Frequency and Mode Identification for Asteroseismology

FAMIAS was originally written for the study of p-mode pulsations (β Cephei, and δ Scuti stars) by Zima (2008), FAMIAS is also capable of analysing the g-mode pulsations in γ Doradus stars. FAMIAS uses the radius (R) and mass (M) in its models to generate what is called the k-value (approximated in Equation 3.6).

$$k = \frac{a_h}{a_v} \approx \frac{GM}{\omega^2 R^3} \tag{3.6}$$

This is effectively a ratio of horizontal (a_h) to radial (a_v) pulsational amplitude and can be seen to be approximately proportional to the mean density divided by the square of the angular co-rotating oscillation frequency ω. The small radial amplitudes of the g-mode, pulsations when compared to the p-mode pulsations, mean that an excellent S/N is required (ideally S/N >200 as sugested by Zima (2008)) for these analyses.

FAMIAS is used for carrying out the Fourier analysis of the line profile variations either of the pixel-by-pixel variation or by moment variation of the line profiles over the discrete and unevenly-sampled timebase. This is in order to obtain the strongest significant frequency in the observed line profile variation. This frequency is then removed via the inbuilt pre-whitening algorithm enabling further frequencies to be found in the residuals, until the largest significant peak in the obtained power spectrum falls to the noise level as determined using FAMIAS.

3.3.1 Frequency analysis and aliasing

Having obtained the significant frequencies from the power spectra, how confident may one be that these frequencies accurately describe the detected pulsational behaviour?

Observing one star from one site, each night will of course give a frequency of one cycle per day (d^{-1}), as the spectra are collected with this frequency. This is a problem, as the sampling pattern alone will produce a spectrum of frequencies which will be convolved with those of the true pulsational frequencies sought, as shown in Figure 3.2.

This effect of sampling could be mitigated by collecting the data at non-regular times, but with an astronomical application, this is limited by the hours of darkness and visibility of the target star. This is where satellite, or multi-site, data is invaluable – it enables sampling at nearly all times of the day, as will be described in Chapter 6.

From the ubiquitous one-cycle-per-day frequency the nightly observations give, aliases of this are also found, so that 2, 3 and 4 d^{-1} frequencies are often found. This, unfortunately, also occurs with the desired signal frequencies too. One may find a third frequency that is just a multiple or combination of any of the prior two. Checking for aliases when frequencies are found is thus very important.

Figure 3.3 shows spectral windows for observations of HD 189631 from each contributing site and as a whole. Distinctive peaks are readily seen at one-cycle-per-day and subsequent aliases. Figure 3.3(a) shows the spectral window for the HARPS observations. There are 273 observations over a relatively short timeframe. The data collection occurred over whole nights from just a few weeks. The expected one-day aliasing is quite low, as the spectra were obtained, not at just one time each night, but over many hours. That they were collected over just a few weeks is significant, as the peaks in the spectrum are broad and

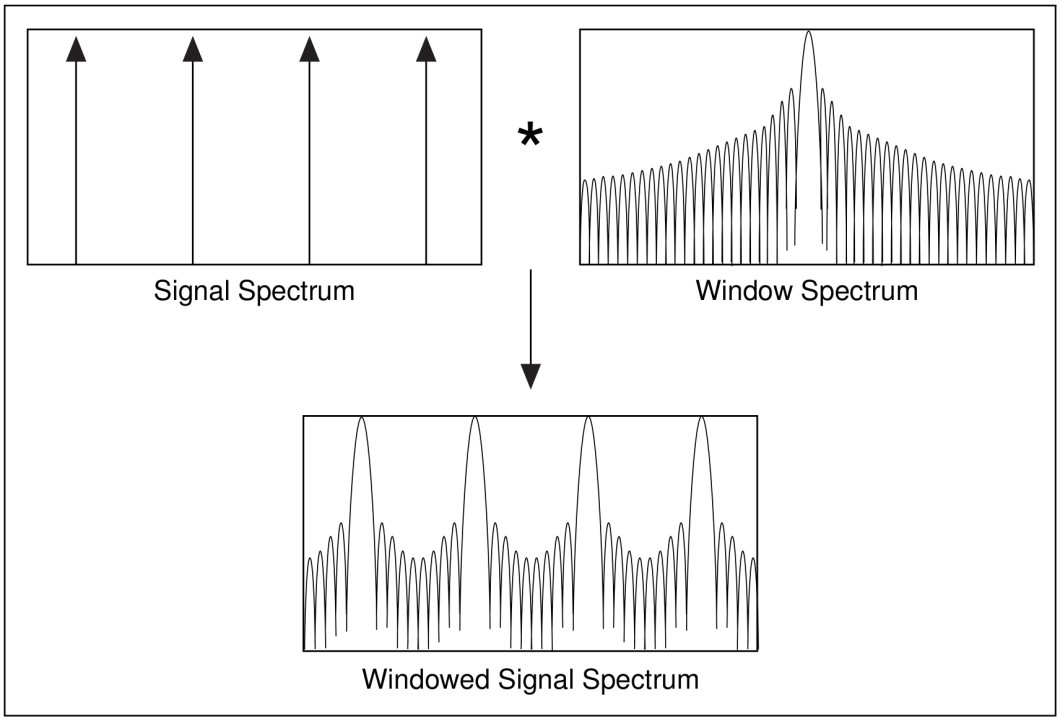

Figure 3.2: Signal frequencies are convolved with a window spectrum (from Cerna and Harvey 2000).

give relatively poor definition of the frequencies. In comparison, the other spectra were taken over a longer timespan, but with fewer spectra in total.

The Fourier spectra from FEROS appear particularly noisy owing to the relatively low number of observations and short timebase over which the observations span. In comparison, the spectra from HERCULES are of a similar number but over a much longer timebase giving better resolution of the peak (more depressed side-lobes) than FEROS, but a similar level of 1-day aliasing.

The sheer number of HARPS spectra means that it dominates in the collective spectral window (Figure 3.3(d)), but the collective timebase is now much longer, giving good sharpness of peaks for frequency determination.

3.3.2 SigSpec and uncertainty

The frequencies and the significance of each identified frequency were calculated using SIGSPEC (Reegen, 2010). SIGSPEC defines significance as per Equation 3.7, that is, the negative logarithm of the false alarm probability, $\Phi_{FA}(f)$.

$$sig(f) = -log[\Phi_{FA}(f)] \tag{3.7}$$

An acceptable significance was deemed to be $sig(f) > 15$. Normally a $sig(f) > 4$ would be acceptable but a more stringent margin is used due to larger observational errors. The determination of practical uncertainties associated with each detected frequency highlights several methods. One of these is the Rayleigh frequency resolution, T^{-1}, where T is the total timebase of observation. This is a poor option, as it has no contribution from the number of observations. That the observations are contributing in a discrete and unevenly-spaced manner makes little difference to the quality of the conclusions drawn. The key difference when compared with that with equally-spaced observations is that aliasing can

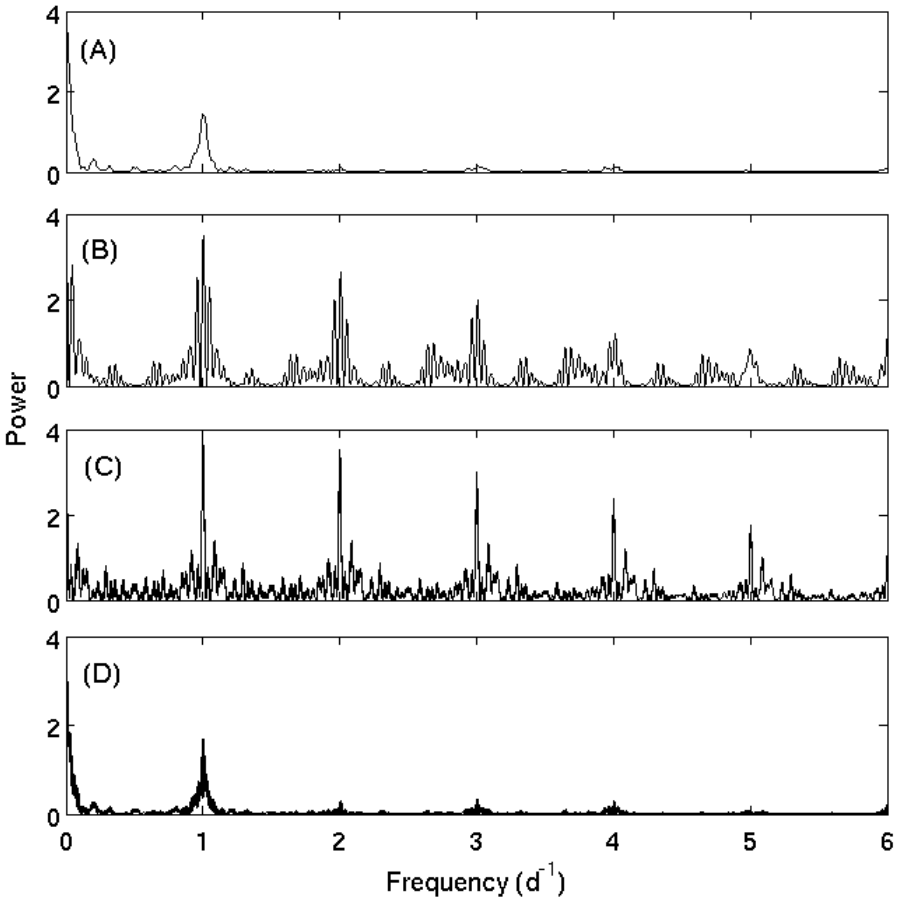

Figure 3.3: Spectral window for HD 189631 observations per site. (A) HARPS; (B) FEROS, (C) HERCULES, (D) all observations combined.

be predicted for equally-spaced observations, but must be examined after the fact in terms of a resultant spectral window (Deeming, 1975) for unequally spaced data.

Montgomery and O'Donoghue (1999) give uncertainties in determined frequencies as given in Equation 3.8:

$$\sigma(f) = \sqrt{\frac{6}{N}} \frac{1}{\pi T} \frac{\sigma(m)}{a} \tag{3.8}$$

, where $\sigma(f)$ is the one-sigma error in frequency, N is the number of observations, T is the total timebase of observations, a is the amplitude associated with the found frequency, and $\sigma(m)$ is the root-mean-square deviation in m, the variable being measured (be it amplitude at a pixel or in a moment). This method gives a more realistic estimate of the uncertainty than the lower value given by a least squares fit. It is argued, however, that Equation 3.9 gives a better estimate of the uncertainty associated with a frequency determined from poorly-sampled observations (Kallinger et al., 2008):

$$\sigma(f) = \frac{1}{T.\sqrt{sig}} \tag{3.9}$$

where sig is defined in Equation 3.7 Unfortunately, poor sampling is almost unavoidable for ground-based observations. In this thesis Equation 3.9 is how uncertainties in the found frequencies will be determined, where applicable.

3.3.3 Mode identification

Given a reliable set of pulsational frequencies, the next step is the identification of the modal geometry of each pulsation. For FAMIAS to identify a mode for a particular frequency, a range of stellar parameters are given, specifying the parameter-space over which it may search for the best (lowest reduced χ^2) fitting mode. This is done by generating models that adequately sample the given parameter-space and using a reduced χ^2 test against the observed line profile variation to focus the searches for reduced χ^2 minima within the parameter-space. It should be noted that reduced χ^2 tests are not typically used for systems with so many variable parameters and that the minimum reduced χ^2 is usually well in excess of 1. It does still indicate the best-fitting model, which is the desired outcome.

FAMIAS automates the model creation, and search for minima, by generating synthetic line-profile variations based on the sum of transformed flux vectors taken at grid points over a stellar disc. For low $v\sin i$ stars, using a grid of 1000 points over the stellar disc is adequate, but for rapid rotators it is suggested that 3000 – 5000 grid points be used to more fully sample the velocity field. The generation and comparison of models is quite time consuming given the sheer number of models that need to be generated to adequately sample a given parameter-space.

FAMIAS fits both the standard deviation profile and the phase of the variation simultaneously. It is also capable of fitting the line profile, but because of the amplitudes involved, the errors in the fit of the line-profile dominate the reduced χ^2. This usually results in very poor fits of phase and variation profiles, which are the most important for mode identification.

In the consideration of fitted modes and phase profiles in FAMIAS, one must be mindful of the physical limitations of the parameter-space being considered. Certain scenarios are not realistic; if for a given $v\sin i$ the value of the inclination varies toward zero the equatorial velocity will exceed the stellar breakup velocity. Clearly if this occurs something is rather awry with the fitted mode.

Similarly, with the frequency found, one must be aware of the effects of rotation upon the appearance of a detected frequency. To the first order we see the appearance of a frequency to be modulated by stellar rotation and the azimuthal order m of the mode:

$$f = f_{n,l} + m\Omega(1 - C_{n,l}) \tag{3.10}$$

(Ledoux, 1951) where f is the observed frequency, $f_{n,l}$ is the frequency as seen in the co-rotating reference frame of the star, Ω is the stellar rotational frequency and $C_{n,l}$ is a Coriolis-related term that approaches $[l(l+1)]^{-1}$ for high order g-modes as described by Aerts et al. (2010; p.287). Equation 3.10 is only valid whilst the conditional Equation 3.11 is met:

$$\upsilon = 2\left|\frac{\Omega}{f - m\Omega}\right| \lesssim 1 \tag{3.11}$$

(Monnier et al., 2010) where υ is the equatorial velocity.

3.3.3.1 Pixel-by-pixel

The line profile variation can be analysed for each pixel across the line. This shows where in the line profile the variation occurs. Some stars, like QW Puppis, show most of their variation in the wings of the profile. Whilst this is fine for stars with low to moderate rotational velocities, stars with higher rotational velocities have greatly broadened line profiles and this smears any line profile variation along with the line. The rotation also has other effects, like the suppression of detectable variability in photometry for retrograde, non-sectoral ($m < 0,\ m \neq l$), modes unless viewed at near pole-on angles ($i \approx 0°$) (Townsend, 2003b). The rotational line broadening does have some benefit in that, by broadening the line, the line profiles have a larger dispersion axis, and so more points across the line for the one profile may be obtained (better resolution).

3.3.3.2 A moment's consideration

Another way to examine line profile variation over time is to parameterise each line profile and examine the variability in each parameter. Given that any observed line profile is a convolution of the intrinsic line profile and the line-of-sight component of the velocity field at the line-formation depth one may calculate moments for each line as described in Balona (1986a,b) and exemplified in Aerts et al. (1992). The method employed in FAMIAS is that of Briquet and Aerts (2003). This paper also satisfactorily demonstrated that using only the first three moments is sufficient for reasonable mode identification in slow-rotating stars.

The easiest way to visualise what the first three moments mean is that the zeroth moment (M_0) is a measure of the equivalent width of the line, the first moment (M_1) gives a measurement of the radial velocity and the second moment (M_2) describes how skewed from vertical the line profile is. The third (M_3) and subsequent moments are not easily visualised as physical parameters and also become increasingly noisy. Additionally for modes above M_3 redundancy appears, as the moments are interpetable as combinations of prior moments.

Chapter 4

HD 189631: broadening the time-base

HD 189631 is a bright F0V, γ Doradus star. HD 189631 was studied in some detail by F. Maisonneuve for his doctoral thesis and presented in a condensed form in the subsequent paper (Maisonneuve et al., 2011). The previous spectroscopic frequencies and modes identified for HD 189631 by Maisonneuve et al. (2011) may be found in Table 4.1.

In this work additional spectra were obtained, substantially broadening the timebase (from 411 days to 1118 days, see Table 2.1) for determination of frequencies . The key outcome of this is to improve the frequency determination of the stellar pulsational behaviour and the confidence in the subsequent mode identifications for them. As seen in Figure 3.3, the sharpness of the peaks for the spectral window was improved by the inclusion of additional spectra at a later date, broadening the time-base.

The spectra obtained for this study were from two sites. Whilst this does offer some relief from the 1-day sampling problem it does not alleviate it completely as there are many more spectra obtained from HARPS and FEROS than from HERCULES. Figure 4.1 shows the uneven distribution of spectra over a period of time phased on one day.

In combining the cross-correlated line profiles from the three spectrographs (HARPS, FEROS and HERCULES) into one data set, the mean line profiles needed to be similar. As HARPS has the highest resolution of the three spectrographs, a greater number of lines can be chosen for creating the δ-function mask for the set by using the HARPS spectra. This gives the cross-correlated line profiles from the highest mean S/N from the three spectrographs. Figure 4.2 shows the sets of cross-correlated line profiles obtained from the various spectrographs.

	Frequency (d^{-1})	Mode (l;m)
f_1	1.68	1;+1
f_2	1.41	3;-2
f_3	0.07[a]	2;-2
f_4	1.82	4;+1[b]

[a]It is possible for a γ Doradus frequency to appear this low if it is retrograde in comparison to stellar rotation (see Section 3.3.3).

[b]The fit of this mode was uncertain, it was suggested that a 2;-2 mode may also be a good candidate for this frequency.

Table 4.1: Summary of previously determined frequencies and modes for HD 189631 in Maisonneuve et al. (2011)

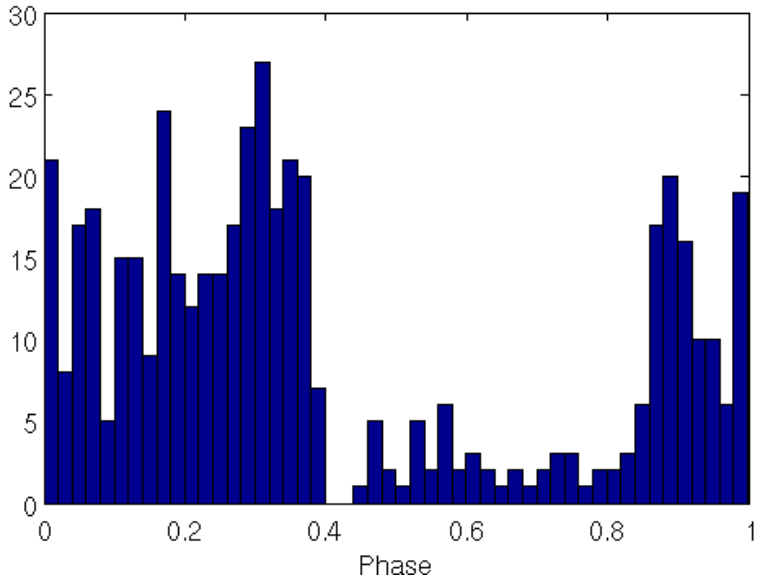

Figure 4.1: 1-day phase plot of spectra for HD 189631 showing uneven sampling of spectra. This bimodality is expected given the disparity in the number of spectra obtained at the two sites.

4.1 Frequency analysis from moments

The first four moments were calculated from the cross-correlated line profiles in FAMIAS. SIGSPEC was used to determine the frequencies and their significance, $sig(f)$, found in the zeroth to third moments of the cross-correlated line profiles (see Table 4.2). Strongly seen in the Equivalent widths (M_0) are the 1-day frequency expected (f_1) and two additional aliases of it at f_2 and f_4. The 1-day frequency also appears as f_3 in M_1 and as f_6 in M_3. The frequency f_3 from the zeroth moment corresponds to an apparent period of 25.6 days but is not seen in any other moment. An absence of significant frequencies in the zeroth moment is expected. No significant change in Equivalent width over time on timescales comparable to the expected γ Doradus g-mode pulsations werw observed for HD 189631.

In the first moment (M_1), several strong frequencies are noted that also appear in other moments. In M_1, f_1 (1.848 d^{-1}) appears very strongly but only marginally visible in the other moments as perhaps a 1-day alias of f_7 in M_1, f_3 in M_3, and perhaps f_5 in M_2.

f_2 at 1.675 d^{-1} appears in M_2 as f_2 (1.677 d^{-1}) and again in M_3 as f_4 (1.666 d^{-1}). This frequency corresponds to f_1 as found by Maisonneuve et al. (2011) (see Table 4.1).

f_4 (1.420 d^{-1}) appears as f_1 in both the second and third moments (1.423 d^{-1} and 1.420 d^{-1} respectively). It may also appear in M_1 as f_1; a possible combination of twice f_4 — f_3. This frequency corresponds to f_2 in Maisonneuve et al. (2011).

In M_1, f_5 (0.071 d^{-1}) also appears as f_2 in M_3 and as f_3 in Maisonneuve et al. (2011).

f_6 (0.561 d^{-1}) in M_1 is also seen (for each moment) as f_8 (0.564 d^{-1}) in M_3.

Using FAMIAS, frequencies were determined separately, as shown in Figures 4.3 and 4.4.

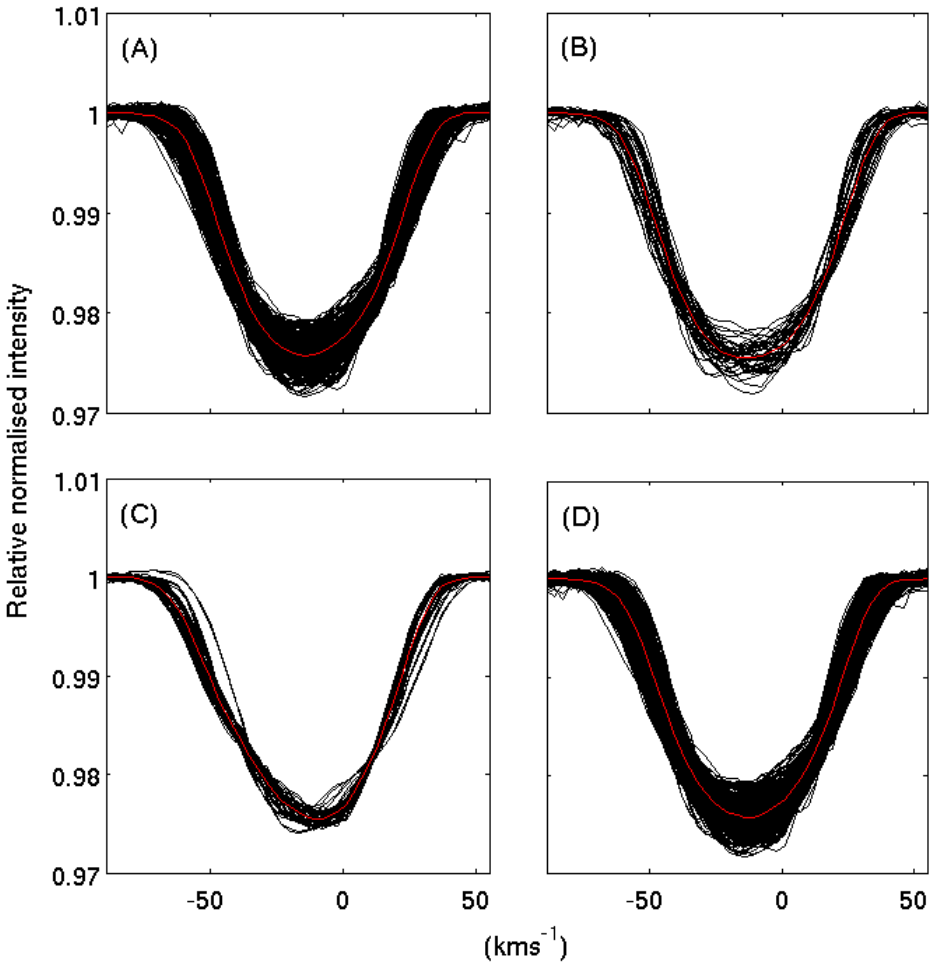

Figure 4.2: A comparison of the cross-correlated line profiles from the three spectrographs. (A): HARPS, (B): FEROS, (C): HERCULES, (D): all observations. Note that the HERCULES data set suffers from a poor sampling of the phase of the dominant pulsations. It can be seen that distinctly different line profiles are obtained at different times.

	M_0		M_1		M_2		M_3	
	Frequency d^{-1}	$sig(f)$	Frequency d^{-1}	$sig(f)$	Frequency d^{-1}	$sig(f)$	Frequency d^{-1}	$sig(f)$
f_1	1.004	56	1.848	28	1.423	36	1.420	31
f_2	3.009	24	1.675	28	1.677	31	0.071	30
f_3	0.039	23	0.993	28	0.598	25	1.794	30
f_4	4.996	9	1.420	26	0.139	23	1.666	27
f_5			0.071	24	2.806	16	0.244	18
f_6			0.561	18	0.968	16	0.993	16
f_7			0.866	17	3.507	11	2.175	16
f_8			1.944	13	3.160	11	0.564	14
f_9			0.325	11				
f_{10}			2.100	10				

Table 4.2: Frequencies determined from analysis of moments for HD 189631. Frequencies for the zeroth (M_0) to third (M_3) moments are shown.

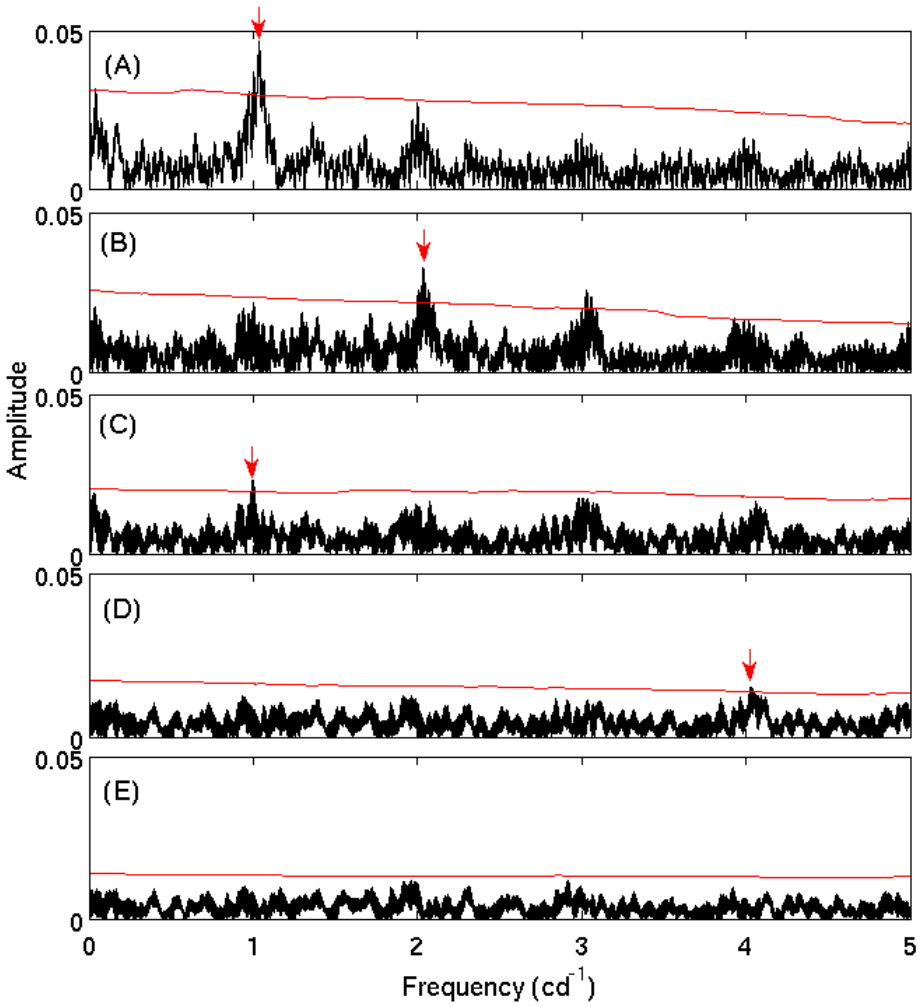

Figure 4.3: Fourier spectra of the zeroth moment (Equivalent Width) of HD 189631. These frequencies appear to be 1-day aliases (A—D) at 1.035 d^{-1}, 2.034d^{-1}, 0.9973d^{-1}, and 4.033d^{-1} with no peak above the noise floor in the bottom panel.

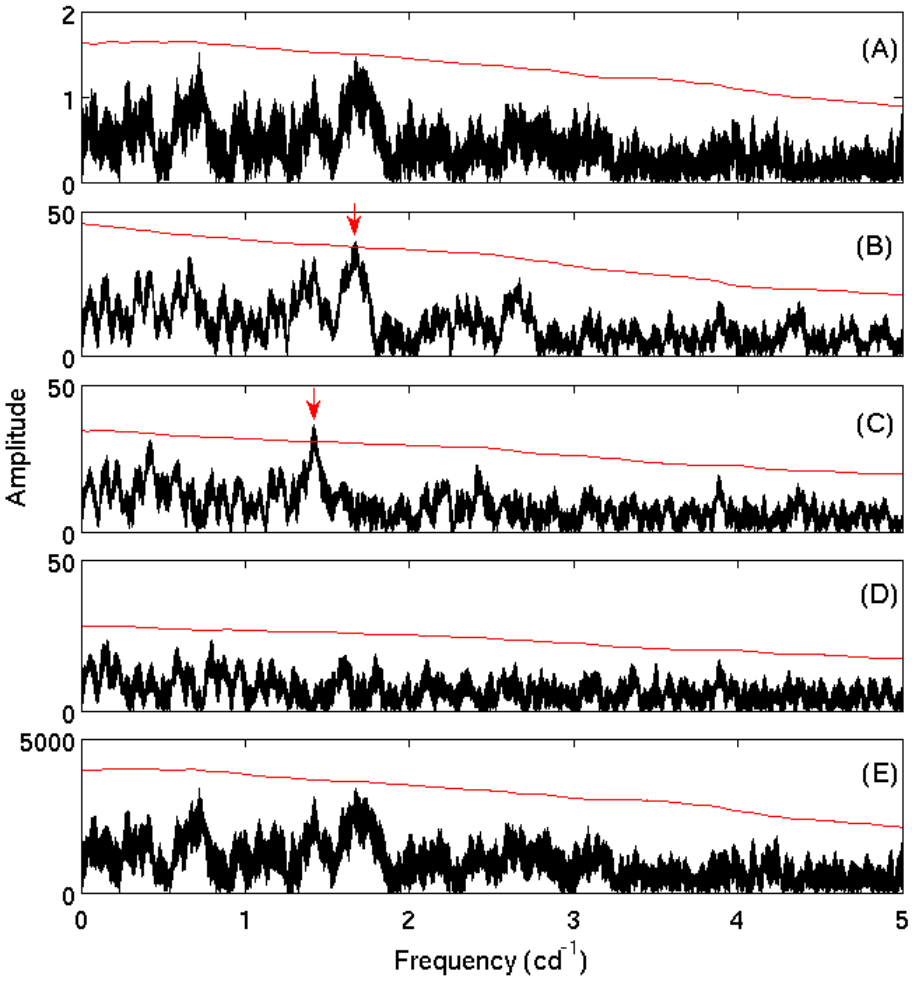

Figure 4.4: Fourier spectra for frequency determination in the first, second, and third moments of HD 189631. The noise floor for each is shown in red. (A): Fourier spectrum of M_1 showing no peak above the noise floor. (B—D): Spectra of M_2 showing frequencies of 1.6744 d^{-1}, 1.4149 d^{-1}, and no peak above the noise floor. (E): a Fourier spectrum of M_3 showing no peak above the noise floor.

	Frequency	
	d^{-1}	$\sigma(f)$
f_1	**1.677**	4×10^{-6}
f_2	**1.420**	4×10^{-6}
f_3	**0.0714**	5×10^{-6}
f_4	**1.823**	4×10^{-6}
f_5	0.996	4×10^{-6}
f_6	2.001	4×10^{-6}

Table 4.3: Frequencies determined from pixel-by-pixel analysis for HD 189631. Uncertainties were estimated using Equation 3.8. In bold are those frequencies retained for further analysis.

4.2 Frequency analysis from pixel-by-pixel method

Frequencies were determined from a pixel-by-pixel analysis of the cross-correlated line profiles. Fourier spectra were created and the frequency corresponding to the highest peak was chosen if above the calculated noise level. A pre-whitening was carried out, removing this frequency and the residuals used as the basis for the next frequency determination.

The determination of frequencies by FAMIAS is perhaps optimistic, as the calculation of the noise floor gives a rather conservative bound on the distinction of noise from a real signal. If a particularly rich range of frequencies are found, FAMIAS may interpret them as noise (such as the 840 frequencies found in the study of HD 49434 by Chapellier et al. (2011) would produce. This may omit significant frequencies if taken alone. Using SIGSPEC also has problems in that it can over-detect frequencies as it takes little consideration of the the intrinsic uncertainty from the contributing spectra. These two techniques were used together to obtain a reasoned set of frequencies for analysis.

Frequencies were determined using FAMIAS as shown in Figure 4.5. The last two frequencies found are seen to be extremely close to one and two cycles per day. The uncertainty for each frequency found by this method was calculated using Equation 3.8 as the determination of a significance using SIGSPEC would have required some combination of significances derived from the analysis of the variation on a pixel-by-pixel basis. These are shown in Table 4.3. Frequencies f_5 and f_6 are seen to be the nightly 1-day frequency and an alias of it. Whilst we cannot be certain that this is not a real frequency in HD 189631, that these frequencies so closely match the peaks in the spectral window due to the data sampling leads to their omission from further analysis.

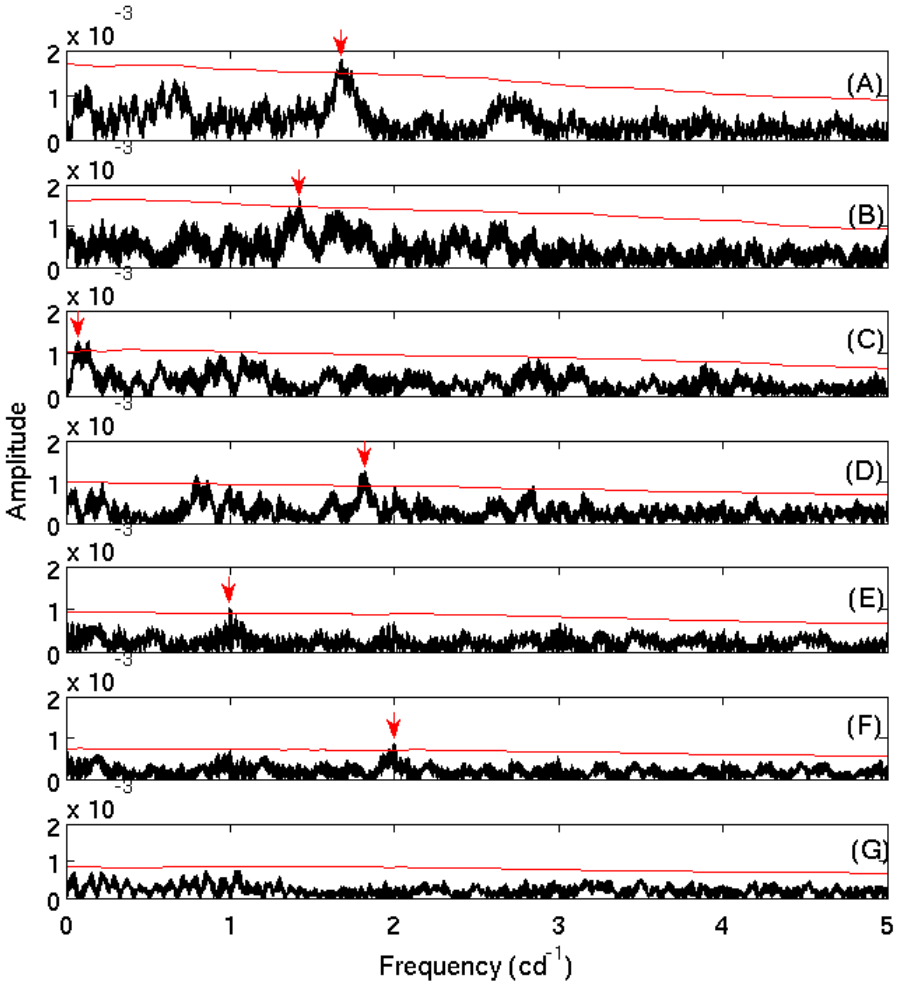

Figure 4.5: Fourier spectra for pixel-by-pixel frequency analysis of HD 189631 in FAMIAS. From top to bottom frequencies are sequentially found and removed by a pre-whitening step. This is done in order of prominence of frequency; the largest amplitude frequency being removed first. The red lines show the 'noise floor'. The bottom spectrum shows no peaks above the noise floor. (A—F) down the highest peak frequencies are: $1.677\mathrm{d}^{-1}$, $1.420\mathrm{d}^{-1}$, $0.0714\mathrm{d}^{-1}$, $1.823\mathrm{d}^{-1}$, $0.996\mathrm{d}^{-1}$, and $2.001\mathrm{d}^{-1}$, with no apparent peak in the seventh (G) spectrum above the noise floor.

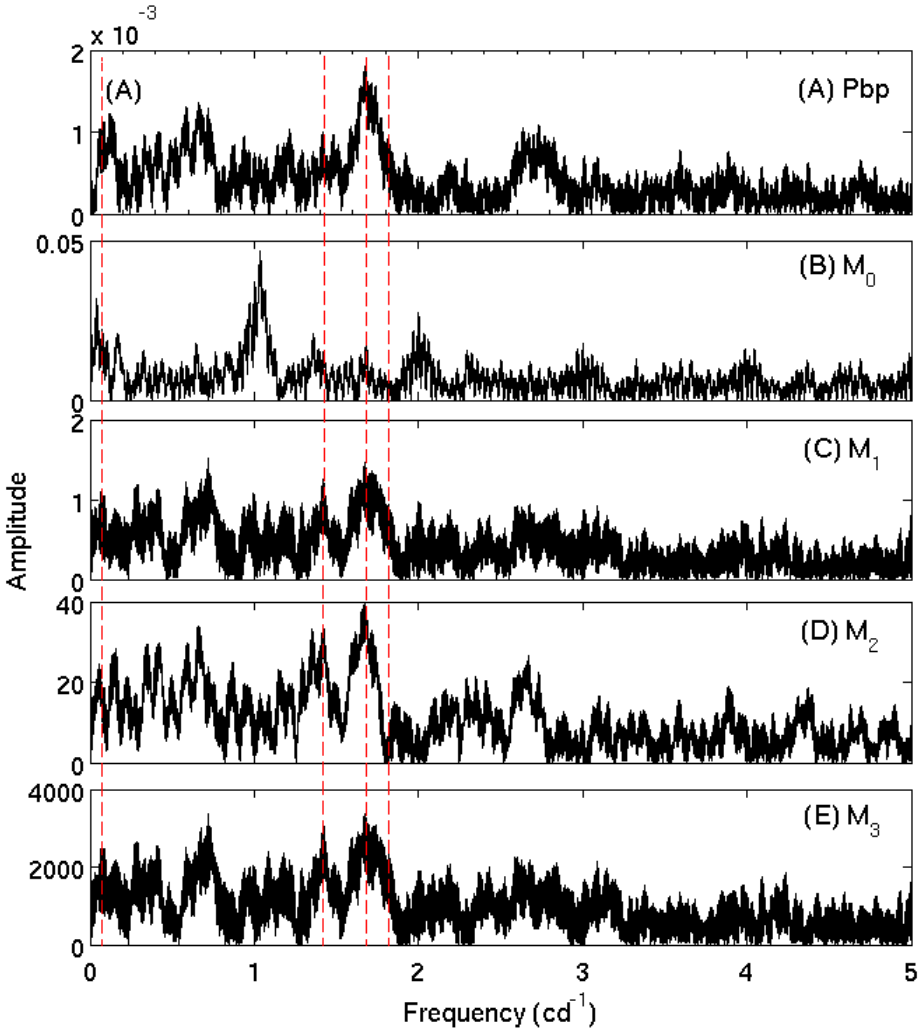

Figure 4.6: Fourier spectra from pixel-by-pixel and from each moment. (A—E): pixel-by-pixel, M_0, M_1, M_2, M_3. Dashed lines in red are the four frequencies found from the pixel-by-pixel analysis. Most of these frequencies are readily seen in moments M_1 to M_3 apart from the 1.822 d^{-1} which is apparent only after several pre-whitening steps.

	Frequency	
	d^{-1}	$\sigma(f)$
f_1	1.6774	0.0002
f_2	1.4174	0.0002
f_3	0.0714	0.0002
f_4	1.8228	0.0002

Table 4.4: The finalised list of frequencies determined for HD 189631 from pixel-by-pixel analysis and from moments.

Comparing the initial Fourier spectra from pixel-by-pixel and each moment reveals many similarities in the spectral features and frequencies (Figure 4.6). The retention of the 1.822 d^{-1} frequency for further analysis was decided on the basis that it appears strongly in *both* the pixel-by-pixel analysis and the first moment Fourier spectra. The uncertainties derived from $sig(f)$ in Table 4.2 using Equation 3.9 were used with the final set of frequencies as we feel they better reflect the larger measure of experimental uncertainty associated with these frequency determinations. That the only frequencies found in the moments using FAMIAS were the 1-day frequency (and aliases) and f_1 and f_2 from Maisonneuve et al. (2011) is rather telling of the different interpretations of what is significant by FAMIAS and SIGSPEC. The final set of frequencies for HD 189631 and their estimated uncertainties are shown in Table 4.4.

Using the frequencies from Table 4.4 it was found that not all of them were sampled well across the whole phase of variation. In particular the lowest apparent frequency f_3 can be seen to be a little sparsely sampled (Figure 4.7 (c)). The paucity of data through phases of about 0.6 and 0.9 make confident model-fitting for mode identification harder.

The variation of the line profiles over the phase of pulsation is shown . It is seen that f_2 and f_4 do not display particularly clean delineation of their pulsation over time. f_2 shows strong features in the wings that appear to remain stationary over some of the pulsational period. Also notable is the slight offset in f_3 (Figure 4.8(c)) which might be accounted for if the phase is poorly sampled, skewing the mean profile away from a mean velocity of zero (green). Generally these phased pulsations seem reasonable and what one would expect from variations due to non-radial pulsation and one may clearly see the retrograde motion of f_3 across the line profile when compared to the other frequencies.

Figure 4.7: Phase sampling for the four frequencies over the dates of observations for HD 189631. (A): f_1, (B): f_2, (C): f_3, (D): f_4. f_3 has the least well sampled phase. This is to be expected as the observed period is of the order of two weeks.

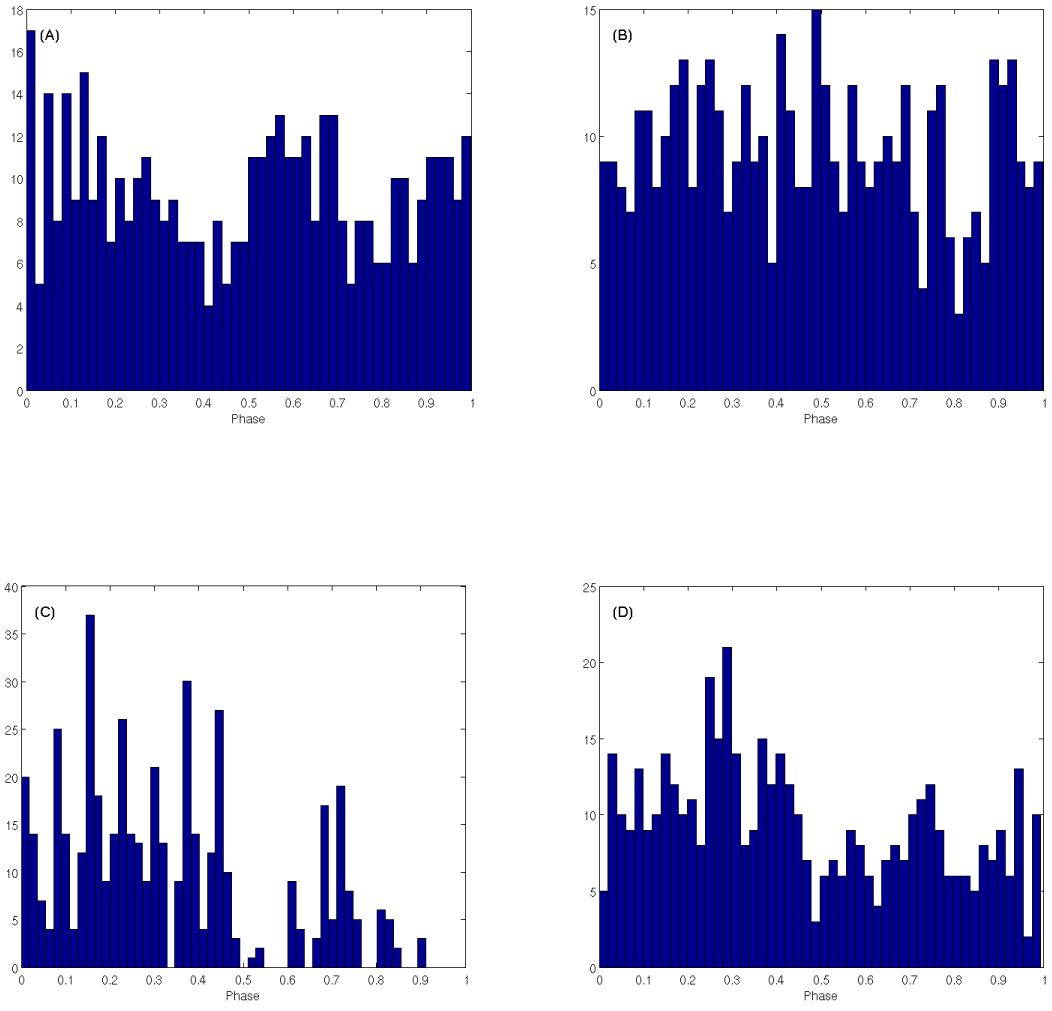

Figure 4.8: Pulsational amplitude over the line profile phased to each determined frequency. (A): f_1, (B): f_2, (C): f_3, (D): f_4. The average line profile has been subtracted.

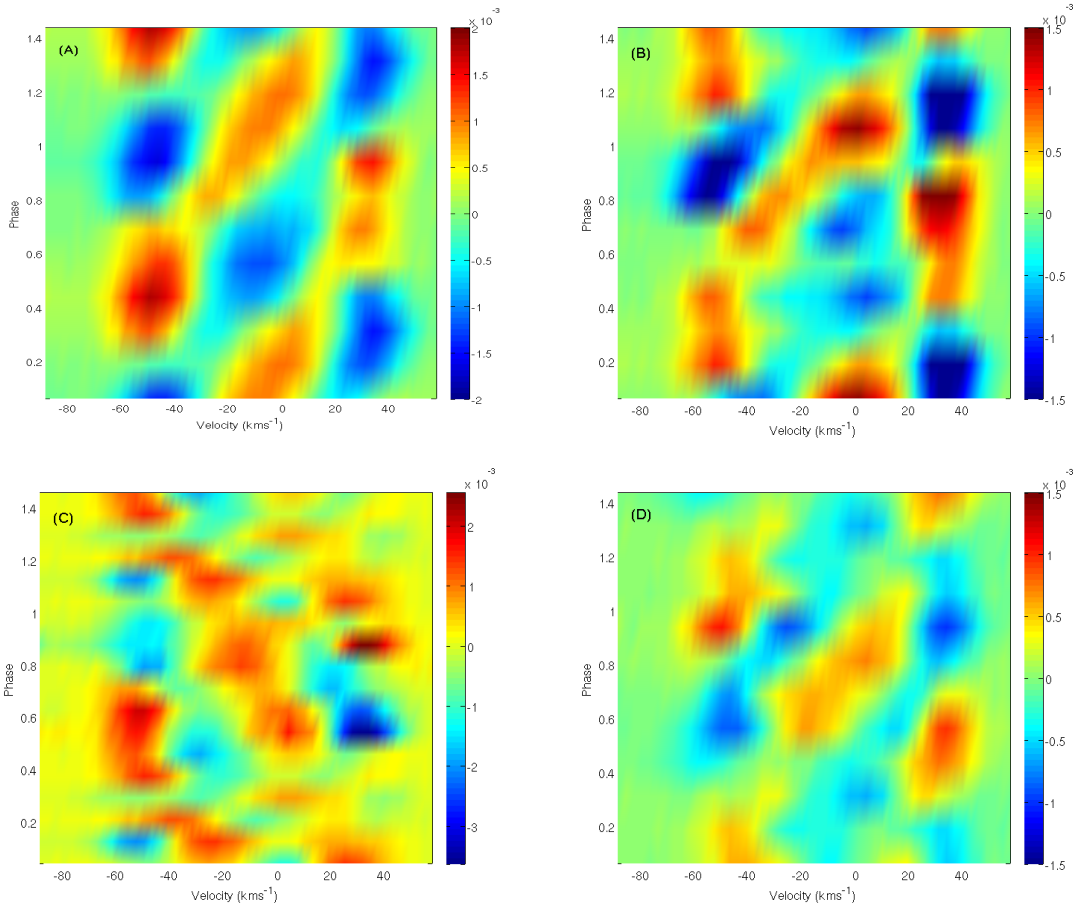

R	1.5 — 1.8 $R_\odot$
M	1.4 — 1.6 $M_\odot$
T	7500K
log$g$	4.2
$[Fe/H]$	0.08
Equivalent width	1.4 — 1.9 kms^{-1}
$v$sin$i$	40 — 50 kms^{-1}
inclination	8°— 90°
Intrinsic width	7 — 10 kms^{-1}
Zero-point shift	-12 — -8 kms^{-1}
l	0 — 4
m	-4 — +4
Amplitude	0.1 — 5 kms^{-1}
Phase	0 — 1

Table 4.5: The parameters used for models generated for mode identification in HD 189631.

l									
0					61				
1				82	76	**11**			
2			47	50	102	66	69		
3		104	58	64	48	63	53	75	
4	128	71	108	52	*33*	39	68	51	78
m	-4	-3	-2	-1	0	1	2	3	4

Table 4.6: Reduced χ^2 values for mode identification of f_1 in HD 189631. The best fit $(1, +1)$ is emboldened and the other notably close fit $(4, 0)$ is italicised.

4.3 Independent mode identification

The first frequency (f_1 = 1.6774 d^{-1}) was fit with models generated in FAMIAS using parameters outlined in Table 4.5. Care was taken to limit the lower bound of the inclination to always be above the inclination at which the equatorial velocity exceeded its critical upper limit. For HD 189631 (with an assumed mass of 1.5 $M_\odot$ and radius of 1.6 $M_\odot$ and a $v$sin$i$ of 43.6 kms^{-1}), a critical inclination of 6° is found, above which equatorial rotation approaches a breakup scenario. The mass and radius estimates were based on typical parameters for the stellar class, so the lower limit for the inclination was set at 8°.

A problem with some mode identifications is that some modes appear very similar at particular inclinations. It is easy, for example, to visualise an $(l, m) = 1, +1$ mode, but now consider an $(l, m) = 2, +1$ mode viewed pole-on and note the similarity. Many mode identifications are very sensitive to the value of the inclination.

The reduced χ^2 values for the models generated (Table 4.6) produced a rather decisive identification that f_1, which was best fitted by an $(l, m) = 1, +1$ mode. This mode was fitted with a reduced χ^2 of 11, the next best fit (a $4, 0$ mode) had a reduced χ^2 of 33. The fit of the phase is clearly much better for the best fit of the (l,m) = $1, +1$ mode (Figure 4.9). This identification agrees with that of Maisonneuve et al. (2011) for the dominant frequency. This best fit mode was achieved with an inclination of 56.0°.

The mode identification of f_2 = 1.4174 d^{-1} was similarly undertaken. It was best fit

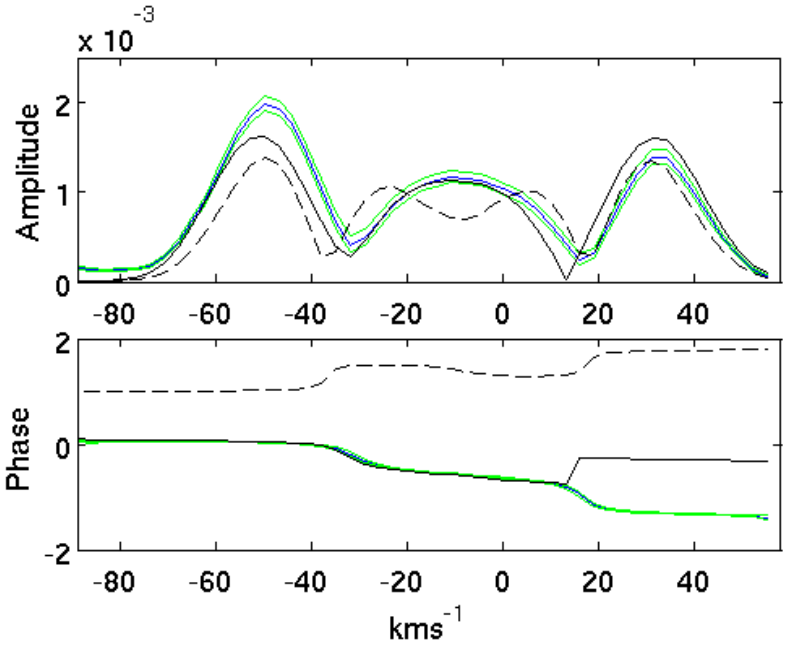

Figure 4.9: Modes fitted to f_1 of HD 189631. Here the observed amplitude and phase across the line are given by the blue line, with error bounds in green. The best fit of the $(l,m) = 1,+1$ mode is given as the solid line and the best fit of the $(l,m) = 4, 0$ mode is given as the dashed line. Note well that a difference of an integer in phase means that the pulsation has the same phase.

with an $(l, m) = 1, +1$ mode (Table 4.7) but with an inclination of 75°. Other close fits were an $(l, m) = 2, -2$ (with an inclination of 13°) or an $(l, m) = 4, 0$ mode (with an inclination of 90°). This difference in the inclinations of the best models is particularly significant when one considers that all modes appear in a star with only one rotational inclination angle (see Section 4.4). The minima for the inclination are rather broad. The mode identified for this frequency by Maisonneuve et al. (2011) was a $(l, m) = 3, -2$ which we find to have a reduced χ^2 value much greater than the best fit $(l, m) = 1, +1$ mode obtained here.

Figure 4.10 shows the three best fits and that of Maisonneuve et al. (2011) for this frequency. The discontinuity in phase at around 20 kms^{-1} has large associated uncertainties, and the phase is generally poorly fit by these models. The asymmetry of the central bump is also poorly modelled with FAMIAS.

The mode identification of $f_3 = 0.0714$ d^{-1} found two modes showing merit. It was best fit with an $(l, m) = 2, -2$ mode (Table 4.8) with another fairly good option being $(l, m) = 4, -2$ mode. The difference in the amplitude profile from these two modes is reasonably small and with the asymmetry in the central bump in the observed profile, is fairly well fit by either a mode with a single central bump or a mode with two low-amplitude central bumps. The difference in the phase of pulsation across the line (Figure 4.11), however, decisively supports the $(l,m) = 2, -2$ mode. Maisonneuve et al. (2011) found a $(l, m) = 2, -2$ mode for this frequency, and this is supported by these results.

The mode identification for f_4 is much more uncertain than the prior modes. The amplitude is small, as it is found in the residuals from three stronger periodic variations. Maisonneuve et al. (2011) found a $(l, m) = 4, +1$ mode but was uncertain and suggested a $(l, m) = 2$, -2 mode as an alternative. These prior results and recommendations are

l									
0					41				
1				30	27	**13**			
2			*24*	39	41	59	40		
3		61	*40*	49	39	47	47	46	
4	39	71	31	38	*25*	54	60	30	55
m	-4	-3	-2	-1	0	1	2	3	4

Table 4.7: Reduced χ^2 values for mode identification of f_2 in HD 189631. The best fit $(1, +1)$ is emboldened and other notable (from Maisonneuve et al. (2011)) or close fits $(2, -2; 3, -2; 4, 0)$ are italicised

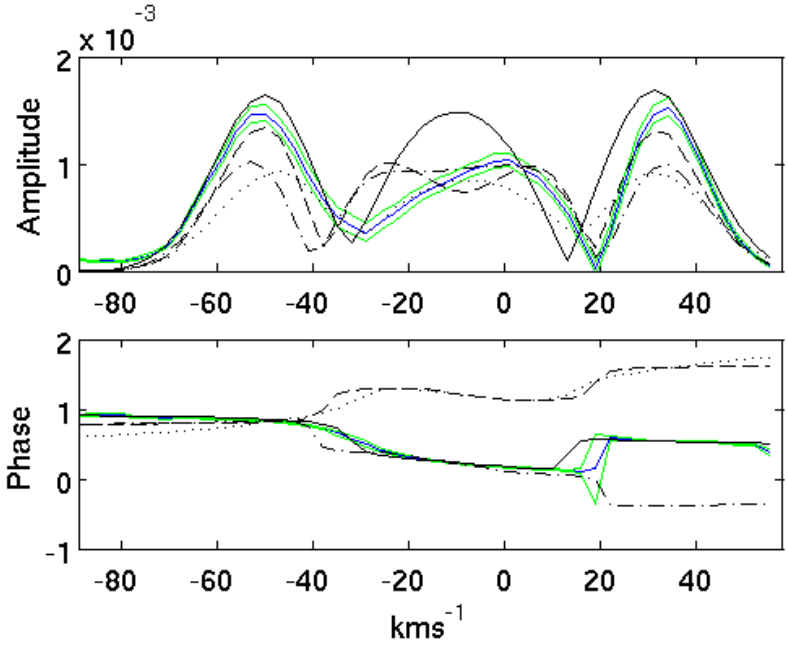

Figure 4.10: Mode identifications for f_2 of HD 189631. Here the observed amplitude and phase across the line are given by the blue line, with error bounds in green. The $(l,m) = 1,+1$ mode is shown with a solid line, the $(l,m) = 4, 0$ mode is shown with a dashed linethe $(l,m) = 2, -2$ mode is shown with the dash-dotted line, and the $(l,m) = 3, -2$ mode is shown with a dotted line.

l									
0					39				
1				39	30	29			
2			**11**	26	48	47	36		
3		36	36	40	28	26	39	38	
4	38	33	*13*	46	33	47	36	47	65
m	-4	-3	-2	-1	0	1	2	3	4

Table 4.8: Reduced χ^2 values for mode identification of f_3 in HD 189631. The best fit $(2, -2)$ is emboldened and the other notable or close fit $(4, -2)$ italicised.

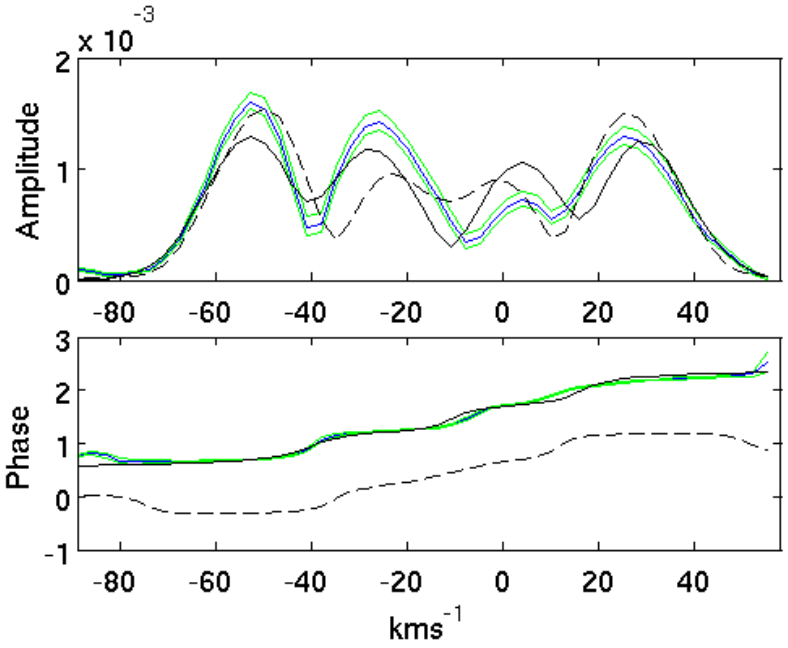

Figure 4.11: Best fitted modes to f_3 of HD 189631. Here the observed amplitude and phase across the line are given by the blue line, with error bounds in green as before. The $(l,m) = 2, -2$ mode is shown with a solid line, the $(l,m) = 4, -2$ mode is shown with a dashed line.

l									
0					33				
1				29	22	**4**			
2			*18*	26	27	27	11		
3		37	28	29	29	29	22	33	
4	40	36	37	21	*16*	*13*	33	22	37
m	-4	-3	-2	-1	0	1	2	3	4

Table 4.9: Reduced χ^2 values for mode identification of f_4 in HD 189631. The best fit $(1, +1)$ emboldened and the modes suggested by Maisonneuve et al. (2011) $(4, +1; 4, 0; 2, -2)$ are italicised.

not in good agreement with those obtained here (Table 4.9). There are good fits of the $(l, m) = 1, +1$ mode, followed by an $(l, m) = 4, 0$, and more distantly followed by those of Maisonneuve et al. (2011). In observing the phase of these pulsational models we see a particularly poor fit to f_4 of the $(l, m) = 4, +1$ mode as recommended by Maisonneuve et al. (2011) (Figure 4.12).

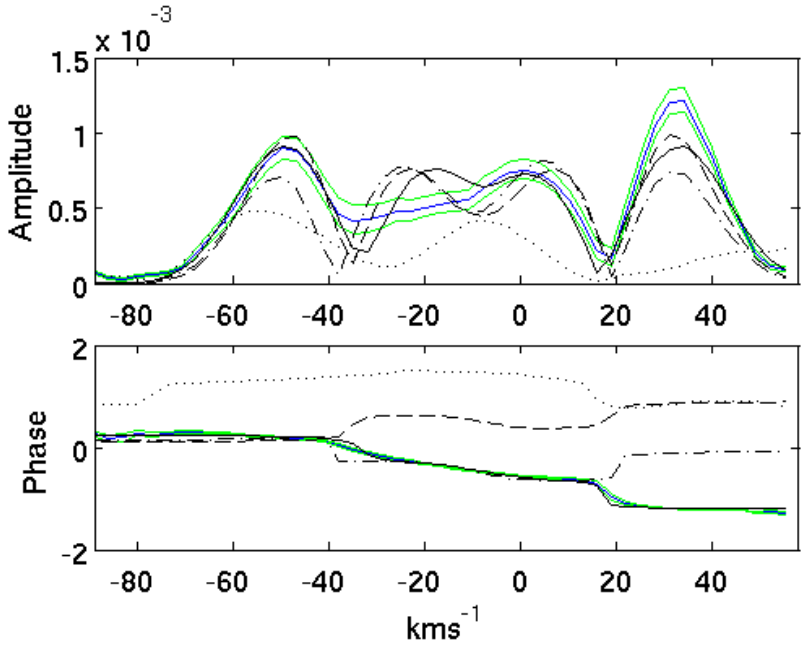

Figure 4.12: Best fitted modes for f_4 in HD 189631. Here, as before, the observed amplitude and phase across the line are given by the blue line, with error bounds in green. The best fit of an $(l, m) = 1, +1$ mode is shown with a solid black line, the best fit of an $(l, m) = 2, -2$ is shown with a dash-dotted line, the best fit of an $(l, m) = 4, 0$ mode is shown with a dashed line, and the best fit of an $(l, m) = 4, +1$ mode is shown with a dotted line.

4.4 Combined mode identification

Mode identification was undertaken with each frequency simultaneously. This forces the models to use one value of each stellar parameter for all modes being fitted. This assumes the pulsation axis for each mode is aligned with the rotation axis.

Modes that are incompatible with each other generate a poor reduced χ^2 when fit together, such as those with very different optimal inclinations. It has been suggested that pulsations may be found that have different pulsational axes; Kurtz et al. (2011) suggest a magnetic pulsation model for rapidly oscillating Ap stars. Whilst the mechanisms at work are dissimilar to those in γ Doradus stars, the intrinsic stellar properties are not. $T = 7400$ K, and a slightly lower log$g$ of 3.6 are given. Whilst this idea of differing axes is only in its infancy, it should still be noted.

All four frequencies were fit simultaneously with models of varying l and m values. As expected the modes found from individual fitting were generally found again in the multimodal fit. The best fitting modes are shown in Table 4.10.

The best fit for f_1 was again an $(l,m) = 1, +1$ mode, for f_2 an $(l,m) = 1, +1$ mode, for f_3 an $(l,m) = 2, -2$ mode and for f_4 an $(l,m) = 1, +1$ mode.

This finding is in agreement with the findings of the individual fits, but conspicuously not in complete agreement with those of Maisonneuve et al. (2011). One thing to note is the difference in the χ^2 values obtained here versus Maisonneuve et al. (2011). Maisonneuve et al. (2011) fit not just the phase and standard deviation profile but the line profile too. The much larger scale in the line profile means that any deviation from the fitted model to the obseverd line profile dominates the χ^2 obtained.

A possible explanation of this discrepancy in these mode identifications is multiple local

Reduced χ^2	f_1		f_2		f_3		f_4	
	l,	m	l,	m	l,	m	l,	m
13	1,	1	1,	1	2,	-2	1,	1
18	1,	1	2,	-2	2,	-2	1,	1
20	1,	1	1,	1	2,	-2	0,	0
20	1,	1	1,	1	2,	-2	1,	0
20	1,	1	1,	1	2,	-2	3,	0
20	1,	1	1,	1	2,	-2	4,	1
20	1,	1	3,	-2	2,	-2	1,	1

Table 4.10: Reduced χ^2 values for multiple simultaneous mode identifications of HD 189631. Only the l, m combinations with the lowest χ^2 values are shown.

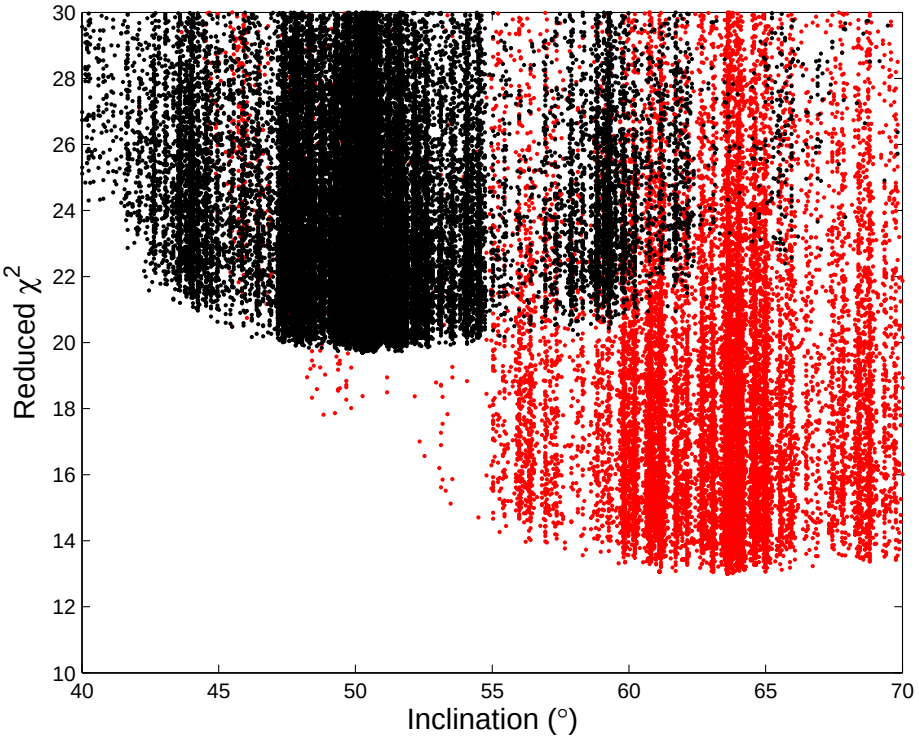

Figure 4.13: Reduced χ^2 values for different inclinations used in the model generation for the fitting to f_2 of an (l,m) = 1, +1 mode in red and (l,m) = 3, -2 mode (as found by Maisonneuve et al. (2011)) in black. These fits were obtained from the simultaneous multi-modal fitting of all frequencies f_1 - f_4.

χ^2 minima in the parameter-space searched. In the optimisation process, if a good model is found then the parameter-space near to that model is searched more closely. This is problematic where things like the azimuthal order m is concerned. If a minimum at $m = -2$ is found, and the adjacent models ($m = -3$ or -1) are poor then models distant to this ($m = +1$ for example) will be examined less. The broadness of the minima in Figure 4.13 gives some idea of the low level of sensitivity to the inclination parameter i. The inclination i, allows for viewing of different sums over the pulsational vector field in the line-of-sight. In the (l,m) $= 3, -2$ case it determines how the equatorial node is presented. What should be noted here is that for low k values (Equation 3.6) as found in g-mode pulsations, FAMIAS does not treat i well. A better independent determination of i could be used from direct matching of synthetic spectra to a good mean spectrum.

4.5 Summary

Analysis of 479 spectra of HD 189631 was undertaken including the 421 spectra analysed by Maisonneuve et al. (2011) and 58 additional spectra from MJUO. Four significant frequencies were found at f_1 1.6774 $\pm$0.0002d^{-1}, f_2 1.4174 $\pm$0.0002d^{-1}, f_3 0.0714 $\pm$0.0002d^{-1}, and f_4 1.8228 $\pm$0.0002d^{-1}. Individual and simultaneous mode identification showed that the best fitting modes were l,$m = (1, +1)$, $(1, +1)$, $(2, -2)$, $(1, +1)$ for f_1 to f_4 respectively. This is in agreement with Maisonneuve et al. (2011) apart from the mode identified for f_4.

Chapter 5

QW Puppis: new observations and a new method

QW Puppis is quite a bright southern γ Doradus star at V = 4.5^m. Wright (2008) analysed spectra of QW Puppis early in the development of mode identificaiton techniques. Wright (2008) found frequencies of 2.122, 2.038, 6.229 and 5.108 d^{-1} via a pixel-by-pixel analysis, two of which were in agreement with two of the frequencies found by Poretti et al. (1997) when aliases were considered.

In the study of QW Puppis a new method will be examined and validated prior to continuing with frequency analysis and mode identification. The analysis of HD 189631 used cross-correlated line profiles. Here will be examined the differences (if any) between cross-correlated line profiles and those obtained by a least-squares deconvolution (LSD). A key part of the rationale for this change is a better ability to deal with rotationally-broadened lines in spectra from stars of higher $v\sin i$. However, before this is applied, it should be demonstrated that both methods perform comparably for a lower $v\sin i$. Wright (2008) found a $v\sin i$ between 50.6 and 52.4 kms^{-1} for QW Puppis. This is a little higher than HD 189631 but still moderate enough to give a fair methodological comparison.

5.1 Cross-correlation versus least-squares deconvolution

The new MJUO spectra from 2012 (Table 2.2) we used for both the cross-correlation and the least-squares deconvolution methods. This single set was chosen because of the number of spectra and their quality. That the data set is large is also relevant because of the relatively long time that the least-squares deconvolution takes to complete.

Both methods created relatively clean line profiles but with some notable differences between the two. Figure 5.1 shows the difference between the line profiles produced by the two methods. Some scaling was carried out to make the line profiles readily comparable. A critical difference is the width of the line profile with the line being much narrower in the LSD method. The absence of broadened wings from inclusion of blended lines means that the line variation is over fewer pixels as seen in Figure 5.1.

Moments were calculated from the generated profiles. These moments are slightly different for the two line profile sets, as the LSD profiles are over a narrower velocity range. The extraction of frequencies from these moments was then undertaken.

What is seen in the frequencies in the zeroth to third moments from the two methods (Tables 5.1 and 5.2) is that, with the exception of f_1 from M_1, most of the frequencies are different in the two methods. There are a few multiples and combinations found between the two sets of frequencies. The significances for the cross-correlated set are generally comparable with that of the LSD set despite the larger number of pixels used in the generation of cross-correlated moments due to line-blending from rotational broadening.

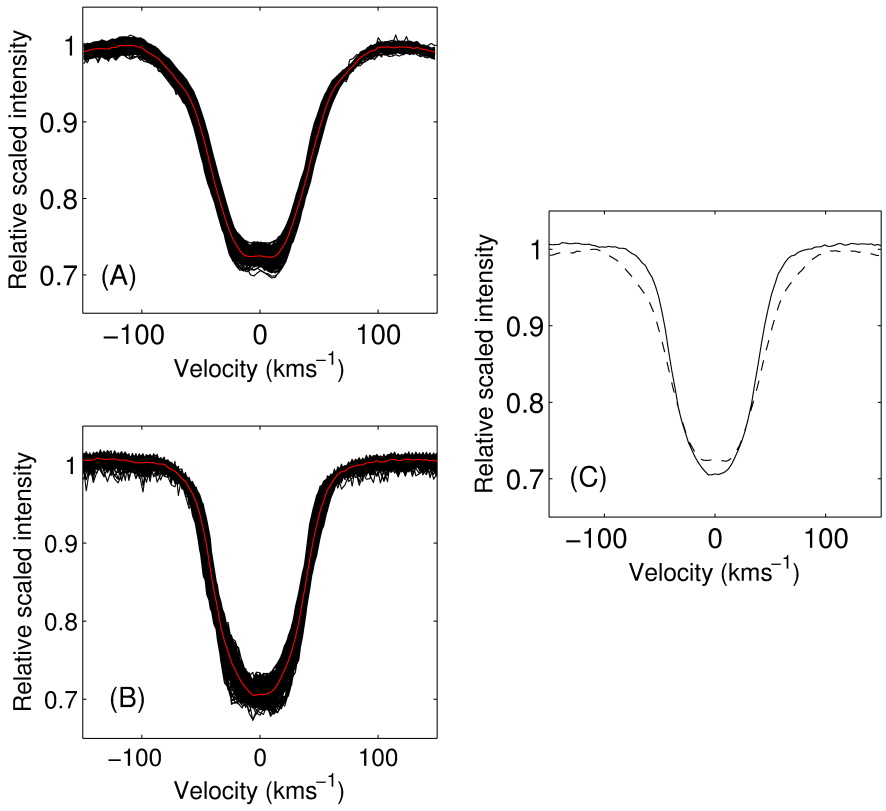

Figure 5.1: QW Puppis line profiles produced using the two different methods. (A): The line profiles generated from the cross-correlation method. (B): The line profiles from the LSD method. The red lines overlayed upon the line profiles are the mean line profiles. (C): The overlayed mean line profiles with the dashed being that of the cross-correlated profiles and the solid line being that of the LSD profiles. Most notable is the contribution to the cross-correlated line wings by blended lines.

	M_0		M_1		M_2		M_3	
	Frequency		Frequency		Frequency		Frequency	
	d^{-1}	$sig(f)$	d^{-1}	$sig(f)$	d^{-1}	$sig(f)$	d^{-1}	$sig(f)$
f_1	1.971	29.8	0.032	53.2	1.067	25.3	1.973	50.1
f_2	1.092	14.7	1.935	32.0	1.994	17.2	2.122	28.4
f_3			2.165	27.1			0.976	22.2
f_4			3.007	17.0			3.903	14.5
f_5			3.242	14.1			2.155	13.5
f_6			5.093	12.8				
f_7			1.426	11.5				

Table 5.1: Frequencies from the analysis of moments using cross-correlation for MJUO 2012 spectra of QW Puppis. Frequencies for the zeroth (M_0) to third (M_3) moments with significances $sig(f) > 10$ are shown.

	M_0		M_1		M_2		M_3	
	Frequency		Frequency		Frequency		Frequency	
	d^{-1}	$sig(f)$	d^{-1}	$sig(f)$	d^{-1}	$sig(f)$	d^{-1}	$sig(f)$
f_1	0.991	34.0	0.032	45.0	0.991	36.6	0.936	19.7
f_2			1.045	24.1	1.274	7.0	2.605	10.8
f_3			0.893	23.0			2.326	7.1
f_4			0.720	14.5				
f_5			2.518	7.0				
f_6			6.009	5.1				

Table 5.2: Frequencies from the analysis of moments using LSD profiles for MJUO 2012 spectra of QW Puppis. Frequencies for the zeroth (M_0) to third (M_3) moments with significances $sig(f) > 10$ are shown.

When analysed on a pixel-by-pixel basis, the LSD method appears superior to the cross-correlation method in the lower level of noise in the Fourier spectrum. Figure 5.2 compares the two Fourier analyses which both show the same first peak (f_1).

5.2 Frequency analysis from moments

Having shown that there are benefits in using the LSD method of line-profile generation, this method was subsequently used for frequency and mode identification of QW Puppis.

Difficulties were encountered with the SAAO data set. A large proportion of this set of spectra had serious defects and had to be omitted at a very early stage in order to obtain a reasonable mean spectrum. The first few attempts at line profile formation produced severely asymmetrical profiles and also had a large offset of the mean centroid (even when the cross-correlation method was used). Initially it was believed that the problem with these line profiles arose from poor barycentric corrections and these were recalculated and reapplied to no benefit. After then suspecting that the continuum fitting was at fault and repeating it several times it was seen that these defects were present in multiple orders

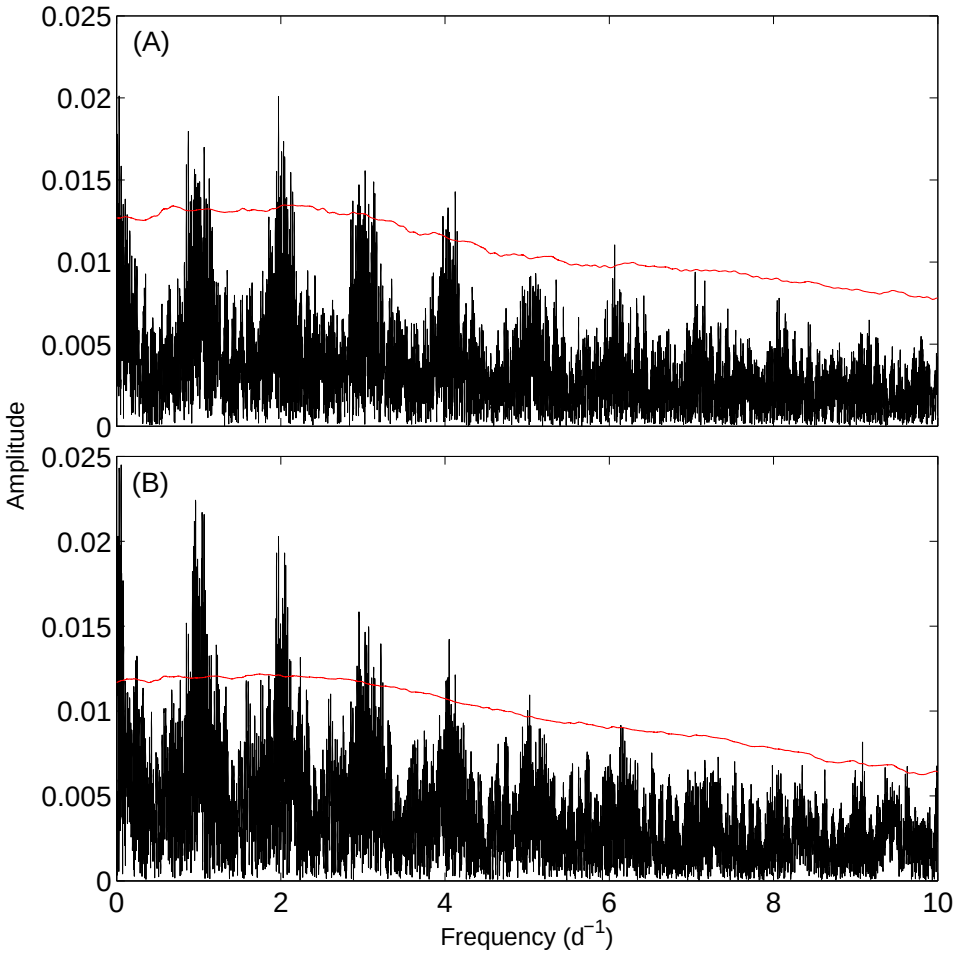

Figure 5.2: Fourier spectra for the pixel with the highest amplitude variation at the first frequency for cross-correlation and LSD methods. A clear reduction in the relative noise level (more and sharper peaks above the red line) between cross-correlated spectrum (A) and the LSD derived spectrum (B) is seen.

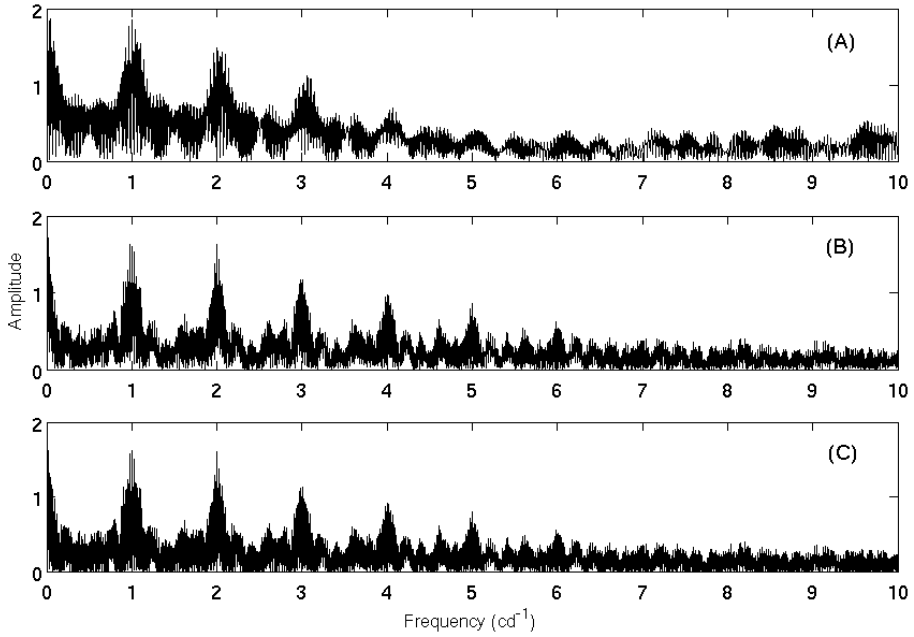

Figure 5.3: (A) Spectral windows from HRSP data, (B) from MJUO 2012 data, (C) from both sets combined.

even prior to normalisation. It is still uncertain what the cause of these defects was as they appeared at many different wavelengths and oft resulted in abberant order profiles as well. It is suspected that this defect arose from poor tracing along the order in the initial stages of FITS reduction on site at the SAAO. Ninety-six of the original 125 spectra were retained after culling the worst offending spectra and it is the line profiles from these that are shown in Figure 5.4. However the line profiles from the SAAO were still too dissimilar to those of the MJUO observations to be included in the analysis. Whilst this data set loses the benefit of having spectra from multiple sites, it still increases the total number of spectra obtained well above that of all prior spectroscopic analyses of this target. The combination of both MJUO data sets does little to the resultant combined spectral window as it is dominated by the larger number of 2012 spectra (Figure 5.3).

Significant too is the bimodality seen in the older MJUO line profiles in Figure 5.4(C). It appears that there are two very distinct groups of profiles obtained. The reason for this is shown in the subsequent frequency analysis where the dominant frequencies found have very long periods which are poorly sampled by this set of observations.

On examination of the frequencies apparent in the calculated moments of the line profiles (Table 5.3), a couple of long-period sampling artifacts are found. The spectra obtained have a very large gap between the two observing campaigns and it is expected that this would be reflected in the frequencies seen in the data set. Even if these two low frequencies were rightly present, the sampling over their expected pulsational phase would be so poor as to make mode identification extremely hard. f_7 in M_1, f_6 in M_2 and possibly f_3 in M_3 (Table 5.3) are likely 1-day aliases.

When the line profiles were phased to the frequencies found from the full LSD moment analysis (Table 5.3), examination of the sampling across the pulsational phase was made possible and the general regularity of the pulsation made visible. Figure 5.5 shows the

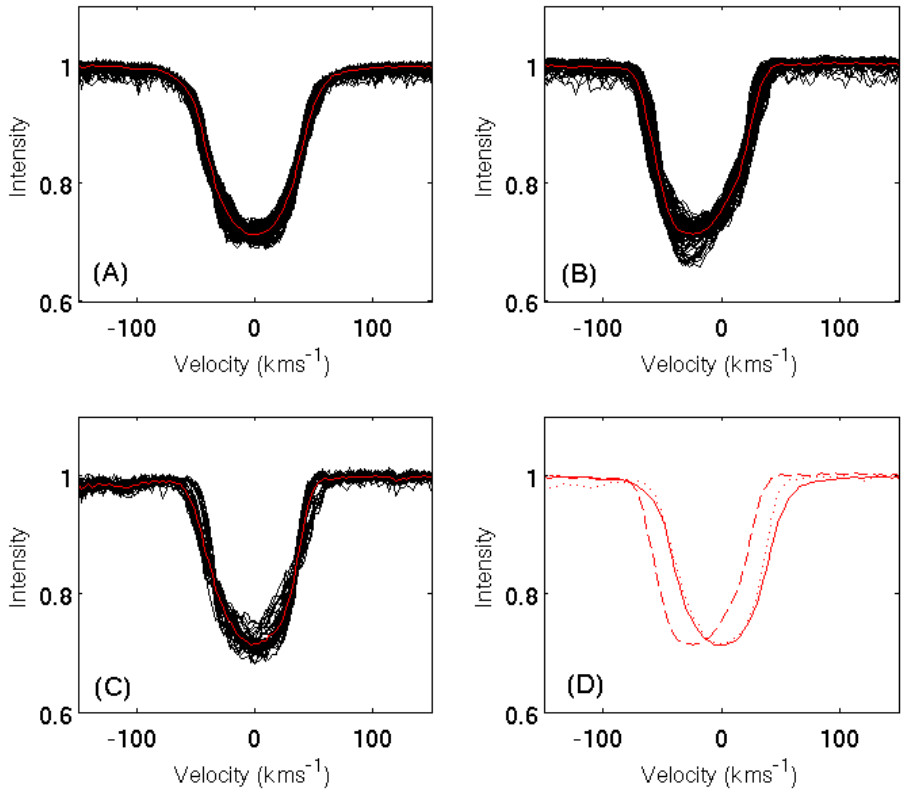

Figure 5.4: QW Puppis line profiles. (A): Those from the 2012 MJUO observing campaign. (C): those from older MJUO observations. (B): line profiles from the SAAO observations. (D): overlayed mean line profiles for each set, with the solid line being that of the 2012 MJUO lines, the dotted line the mean of the older MJUO observations and the dashed line the mean of the SAAO observations.

	M_0		M_1		M_2		M_3	
	Frequency d^{-1}	$sig(f)$	Frequency d^{-1}	$sig(f)$	Frequency d^{-1}	$sig(f)$	Frequency d^{-1}	$sig(f)$
f_1	0.00050[a]	73	**0.0548**	51	0.00033[b]	56	**0.0552**	55
f_2	0.0104	29	**0.0634**	53	2.0462	31	**0.0638**	47
f_3	0.0121	21	0.2051	30	0.9347	24	2.0390	25
f_4	1.8917	13	2.9446	22	**2.9648**	17	1.8790	18
f_5	1.8125	11	2.1196	19	0.7014	13	3.2420	13
f_6			3.3592	18	4.9985	12	6.6021	14
f_7			1.0020	11			4.0709	14
f_8			0.0751	11			2.6347	11
f_9							3.2507	11

Table 5.3: Frequencies from analysis of moments from LSD profiles obtained from the combined set of spectra. Frequencies for the zeroth (M_0) to third (M_3) moments are shown. In bold are those frequencies retained for mode identification.

pulsational pattern and sampling over phase for f_1 in M_1 (0.0548 d^{-1}). There is some cyclicity with the pattern moving from zero to one phase, however the phase sampling of these data is sporadic. This is similarly seen for f_2 and f_3 in M_1. f_4 shows fair periodicity but it is noted that one may almost exactly obtain f_4 as a three-daily alias of f_1 ($3 - 0.0548$). The frequency f_5, however, looks reasonably robust in the defined profile over the phased period, but it is noted that two times the $1d^{-1}$ (which is readily found in the pixel-by-pixel analysis) when added to f_1 and f_2 give a frequency of 2.1182 d^{-1}, which is very close to f_4 at 2.1196 d^{-1} (from M_1), and well within uncertainties, so this could be an alias. With such small frequencies as f_1 and f_2 it becomes easy to construct other frequencies similar to multiples of them.

Figure 5.6 shows the line profile and phase sampling for the frequencies obtained in the second moment. The phase sampling for f_1 is very poor. If one adds twice M_1's f_1 and subtracts M_1's f_2 with two nightly 1 d^{-1} one obtains 2.0464 d^{-1}, hence in M_2 we can see this as $f_2 = 2.0462$ d^{-1}. f_4 shows a noisy but strong profile and fair sampling and is worth a closer examination. It is not readily apparent that this frequency is an alias of another. It is similar to, but more clear than, f_4 in M_1. The profile of f_3 looks very poor. f_5 appears scattered in the phased phased line profiles. f_6 appears weak but also as if the period should be longer than that given by the frequency to which the line profiles have been phased. f_2 and f_4 were retained for mode identification.

Figure 5.7 shows the rather disappointing results from phasing to the frequencies found in M_3. With the exception of f_1, which is rather similar to f_1 in the first moment, little is seen of hopeful periodicities.

5.3 Frequency analysis from pixel-by-pixel method

Pixel-by-pixel analysis was undertaken (again using FAMIAS) for the LSD-derived line profiles. These frequencies were removed from the data in a prewhitening step to allow subsequent frequency analysis of the residuals. This was done using both the full set of spectra and solely from the recent 2012 set, as the recent set avoids problems with such a long data-poor period between observing runs (Figure 5.8).

The frequencies found are shown in Table 5.4. The difference in the magnitude of the associated uncertainties between the full dataset and the 2012 data is due to the change in the timebase over which the spectra were collected. The frequency f_6 from the 2012 data alone is also seen as f_1 in the full data set. The standard deviation profile across the line for f_1 is also much superior to f_5. f_1 and f_3 were retained because they appeared in the analysis of moments strongly, and f_4 because of the clarity of phased profiles. The f_1 and f_3 were checked to see if any simple 1-day aliases (1—3 $\pm$ f_1, f_3) showed more clear variation but they did not.

Examining the sampling over the phase of these frequencies in Figures 5.9 and 5.10, the very low frequencies and frequencies close to 1 d^{-1} are poorly sampled. This is expected for this single-site dataset as the 1 d^{-1} alias is inescapable and longer periods will not be fully sampled as they require particularly long continuous observing runs - challenging to obtain in competitive telescope schedules even with *a priori* frequency analysis.

The frequencies found as prospects for mode identification are shown in Table 5.5. In consideration of aliases within this group of frequencies it is noted that the uncertainties stated are so low that these frequencies could not be aliases of one another. It is suspected that these uncertainties are underestimated, as the total timebase T used to calculate

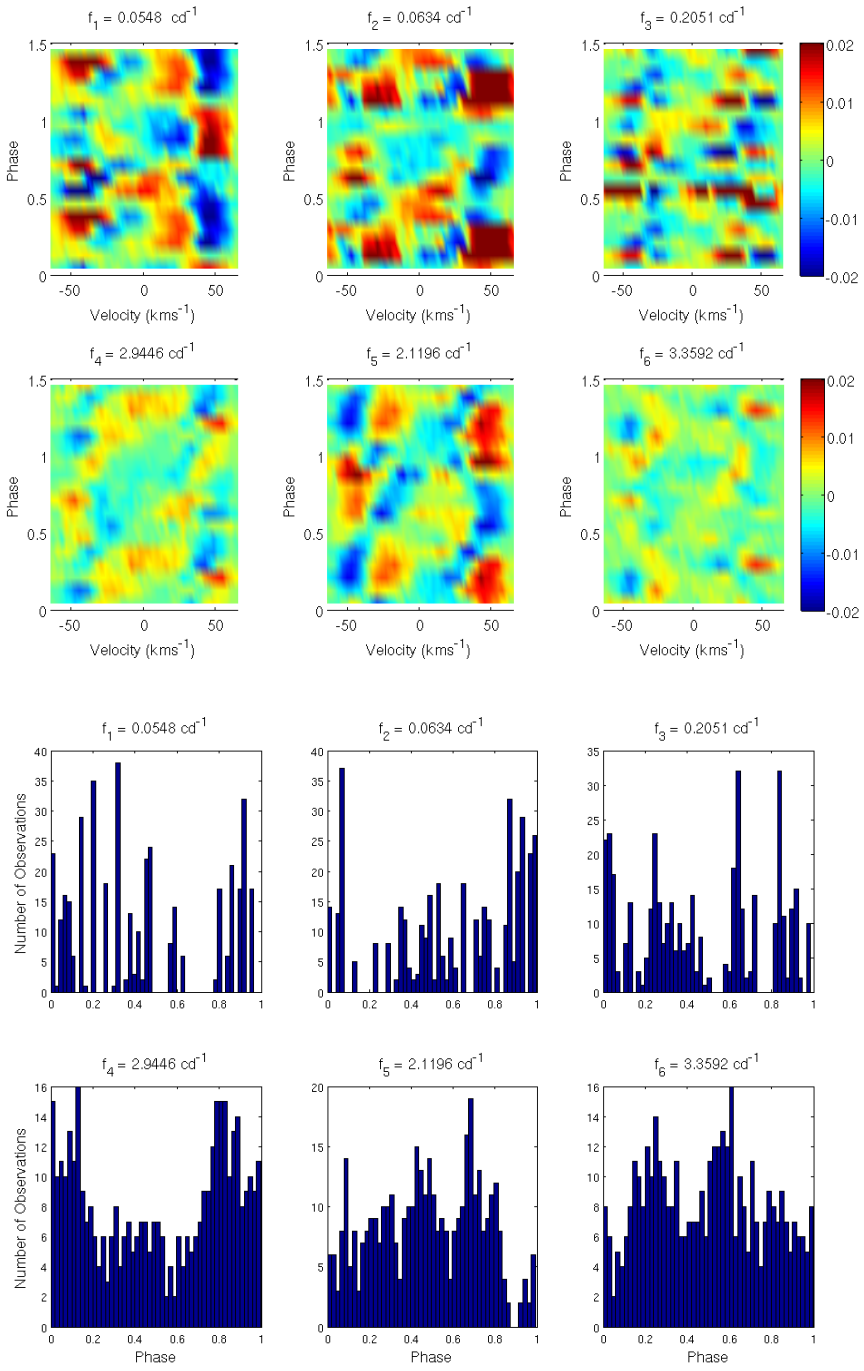

Figure 5.5: Pulsational amplitude over the line profile phased to each determined frequency from the first moment (M_1 - see Table 5.3). The average line profile has been subtracted. Lower panels: data sampling across the phase of the pulsations.

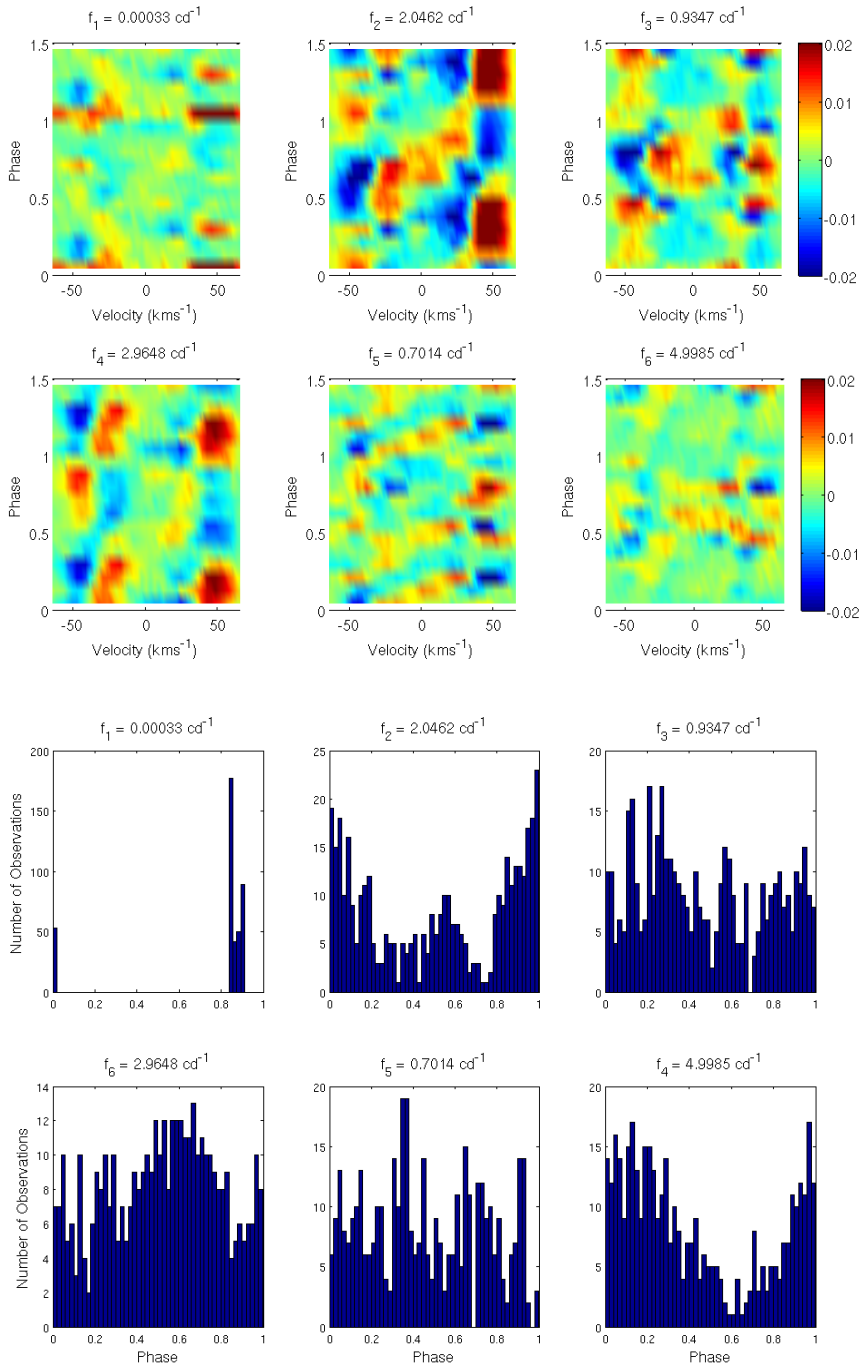

Figure 5.6: Pulsational amplitude over the line profile phased to each significant frequency from the second moment (M_2 - see Table 5.3). The average line profile has been subtracted. Lower panels: data sampling across the phase of the pulsations.

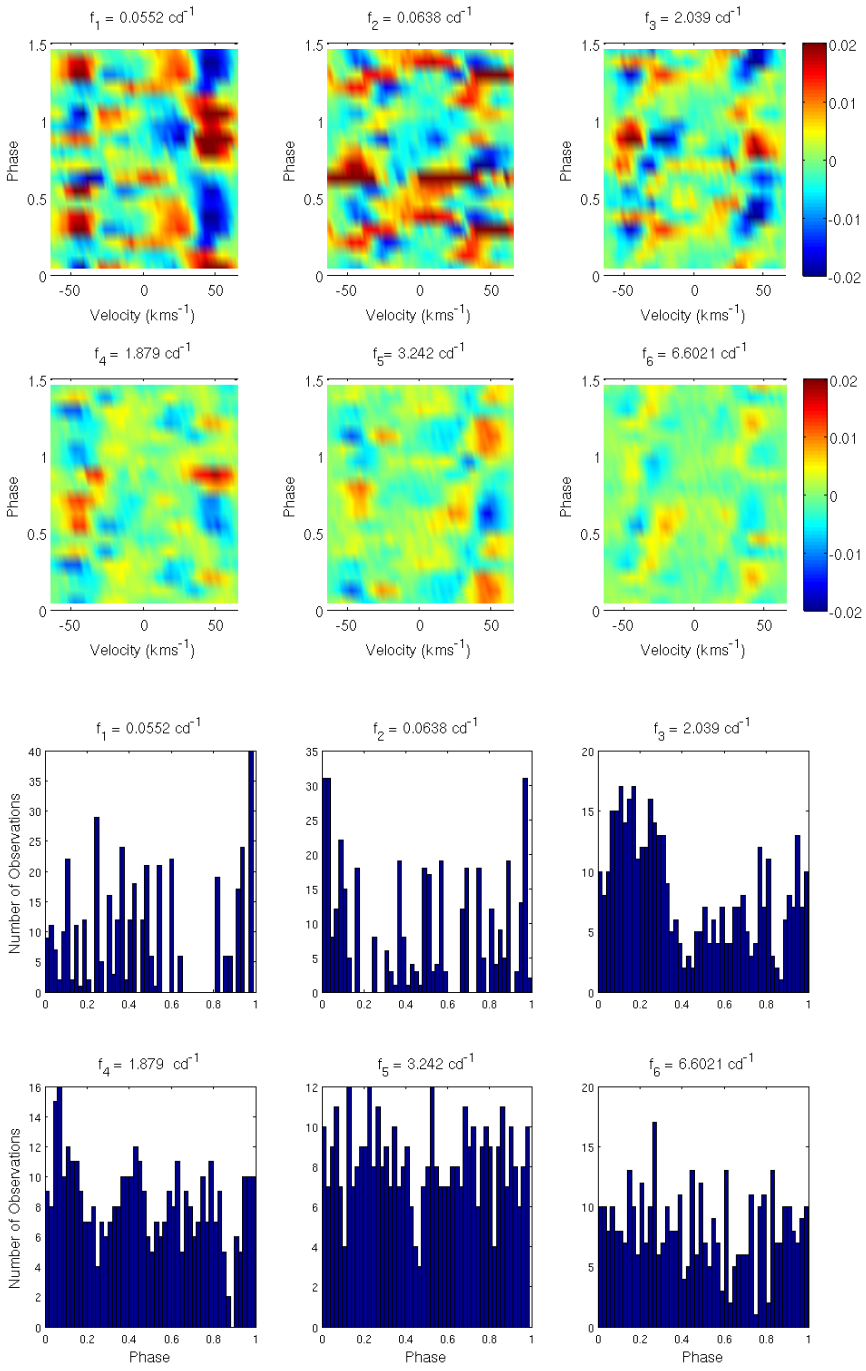

Figure 5.7: Pulsational amplitude over the line profile phased to the six most significant frequencies from the third moment (M_3 - see Table 5.3). The average line profile has been subtracted. Lower panels: data sampling across the phase of the pulsations.

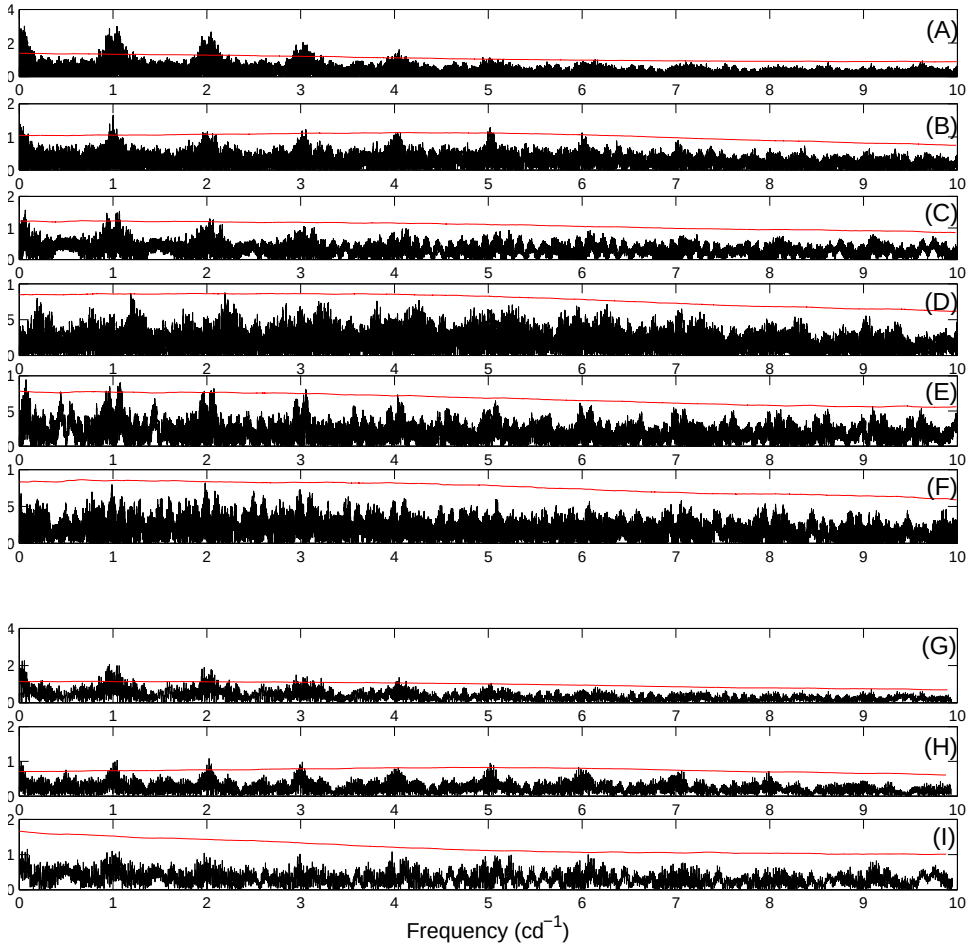

Figure 5.8: (A—F) Fourier spectra of the pixel with the highest amplitude from which the frequencies of the dataset were found. (G—I): data from only 2012. In each set the bottom spectrum is that of the noise floor, with no significant peak above this level.

	Frequency	
	d^{-1}	$\sigma(f)$
f_1	**0.055972**	0.000005
f_2	1.000972[a]	0.000003
f_3	**0.064846**	0.000004
f_4	**5.219398**	0.000002
f_5	1.052200	0.000003
f_6	0.0557	0.0006
f_7	2.0249	0.0004

[a]likely 1-day sampling frequency

Table 5.4: Frequencies determined from the pixel-by-pixel analysis of QW Puppis. Uncertainties were estimated using Equation 3.8. Frequencies f_6 and f_7 are from analysis of only the 2012 line profiles (Figure 5.8). Those in bold were retained for mode identification.

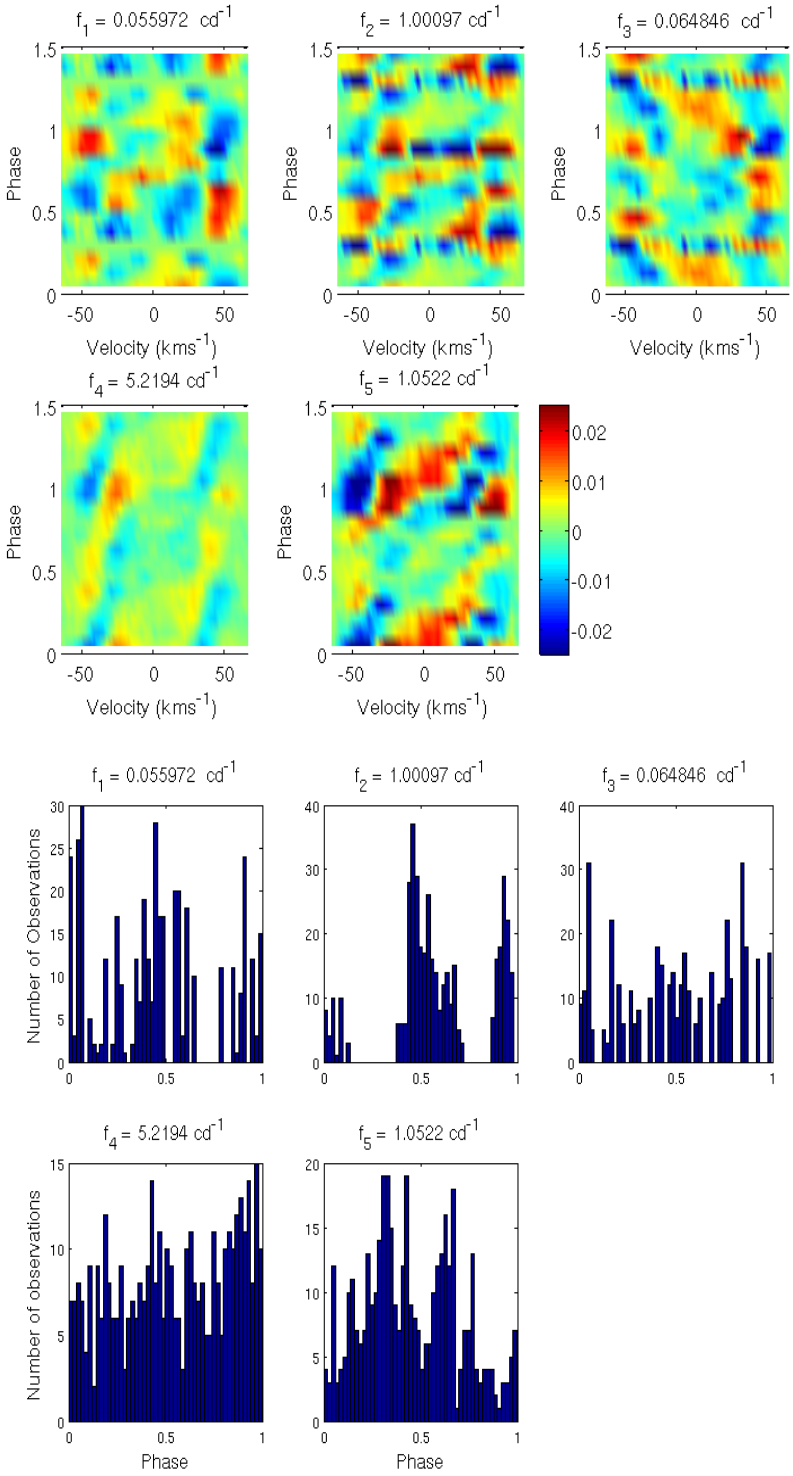

Figure 5.9: Pulsational amplitude over the line profile phased to pixel-by-pixel frequencies from (f_1 to f_5 — see Table 5.4). The average line profile has been subtracted. Lower panels: data sampling across the phase of the pulsations.

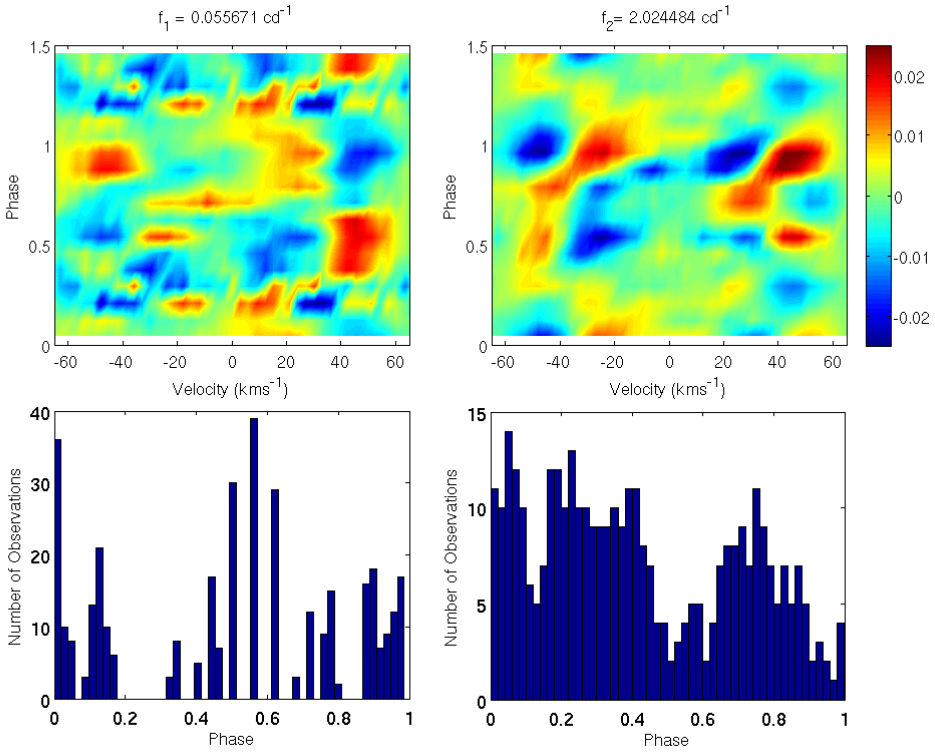

Figure 5.10: Phase sampling and pulsational amplitude from pixel-by-pixel analysis of 2012 MJUO line profiles (f_6 and f_7 — see Table 5.4). The average line profile has been subtracted. Upper panels: data sampling across the phase of the pulsations.

	Frequency	
	d^{-1}	$\sigma(f)$
f_1	0.055972	0.000004
f_2	0.064846	0.000004
f_3	5.219398	0.000002
f_4	2.9648	0.00009

Table 5.5: Frequencies for further examination in QW Puppis. f_1, f_2, f_3 are the frequencies from pixel-by-pixel analysis and f_4 from moments. Uncertainties given were calculated with Equations 3.8 or 3.9 as appropriate.

them perhaps assumed a more even sampling than was obtained in this work. Examining the standard deviation and phase profile generated for these frequencies, the veracity of possible combinations of frequencies giving rise to others was examined. However the frequency with the strongest appearance in the Fourier spectrum was retained.

What is noticeable is that Poretti et al. (1997) found 1.0434 ± 0.0004, 0.9951 ± 0.0010, 1.1088 ± 0.0017 and 0.9019 ± 0.0020 d^{-1} in *uvby* photometry and, debatably, these are not found here until aliases are considered. However, these findings were from 20 measurements over a total timebase of 41 nights. Wright (2008) found frequencies of 2.122, 2.038, 6.229 and 5.108 d^{-1} from 179 MJUO and SAAO spectra obtained over a timebase of 55 days in 2004. Here 411 spectroscopic line profiles were used from a total timebase of 2761 nights. f_1 and f_2 are found strongly both in moments and in the pixel-by-pixel analysis. These frequencies are likely only obtained in this work because of the long timebase afforded to it. The frequency f_3 is comparable to one of those found by Wright (2008) but not equal to it. Wright's first frequency has already been detected and excluded here as being an alias of f_1 and f_2, and his first two frequencies were identified as aliases of frequencies found by Poretti et al. (1997).

Forced fits of the frequencies from the literature, but not found here, are given in Appendix B.

5.4 Independent mode identification

Independent mode identification was carried out on each of the frequencies shown in Table 5.5 using FAMIAS. The initial parameters used are shown in Table 5.6. It should be noted that QW Puppis has a lower critical inclination of $i_{crit} = 8°$ in order to reach breakup equatorial velocity for the $v\sin i$ found by Wright (2008). This value was used as the lower bound on inclination for FAMIAS. Other values were chosen as typical for stars of this type as in prior work (Wright, 2008).

M	1.2 — 1.8 $M_\odot$
R	1.3 — 1.9 $R_\odot$
T	7500K
log$g$	4.2
$[Fe/H]$	-1.0
Equivalent width	10 — 40 kms^{-1}
$v$sin$i$	48 — 54 kms^{-1}
inclination	8°— 90°
Intrinsic width	6 — 16 kms^{-1}
Zero-point shift	-0.708661 kms^{-1}
l	0 — 4
m	-4 — +4
Amplitude	0.01 — 40 kms^{-1}
Phase	0 — 1

Table 5.6: The parameters used for models generated for mode identification of QW Puppis.

l									
0					80				
1				**27**	50	**29**			
2			43	**29**	54	33	36		
3		77	43	34	60	34	47	47	
4	72	84	44	37	67	31	31	49	55
m	-4	-3	-2	-1	0	1	2	3	4

Table 5.7: Reduced χ^2 values for mode identification of f_1 in QW Puppis. The best fits are emboldened.

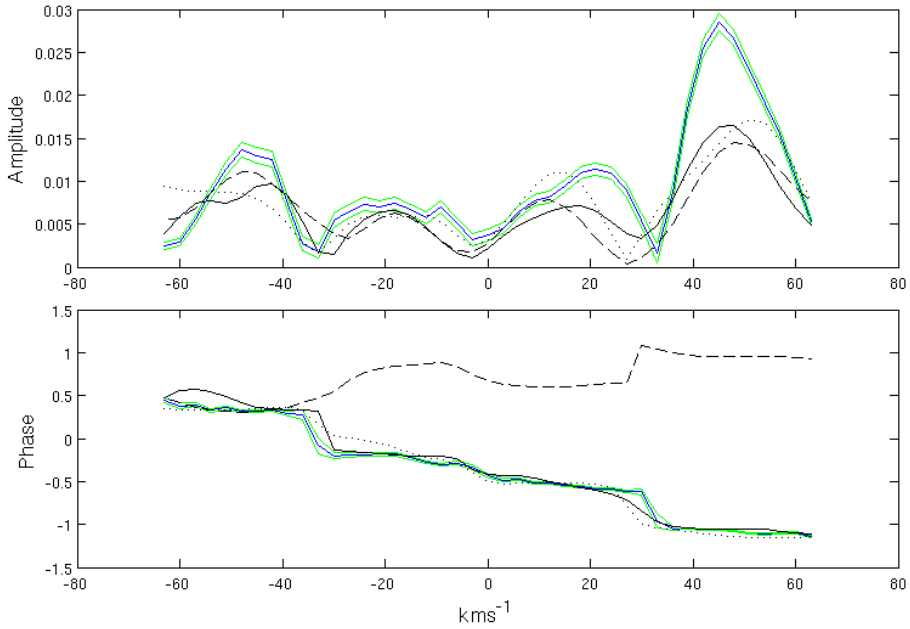

Figure 5.11: Best fitted modes for f_1 in QW Puppis. Here, as before, the observed amplitude and phase across the line are given by the blue line, with error bounds in green. The best fit of an $(l, m) = 1$, -1 mode is shown with a solid black line, the best fit of an $(l, m) = 2$, -1 mode is shown with a dashed line, and the best fit of an $(l, m) = 1$, +1 mode is shown with a dotted line.

Table 5.7 shows the best χ^2 obtained for each mode. The best obtained for f_1 was for an (l,m) = 1,-1 mode closely followed by an (l,m) = 1,+1 and an (l,m) = 2,-1 mode. The fit of these is relatively poor due to the severe asymmetry in the deviation profile (Figure 5.11), but they were well-fit to the phase profiles, and in particular the transitions in the (l,m) = 1,-1 mode. Possible modes for $5 \leq l \leq 8$ were also examined with none showing a better fit (lower reduced χ^2) than those shown.

l									
0					17				
1				16	19	11			
2			24	**7**	17	**8**	28		
3		26	14	9	15	10	18	19	
4	14	16	15	**7**	17	**6**	11	16	17
m	-4	-3	-2	-1	0	1	2	3	4

Table 5.8: Reduced χ^2 values for mode identification of f_2 in QW Puppis. The best fits are emboldened.

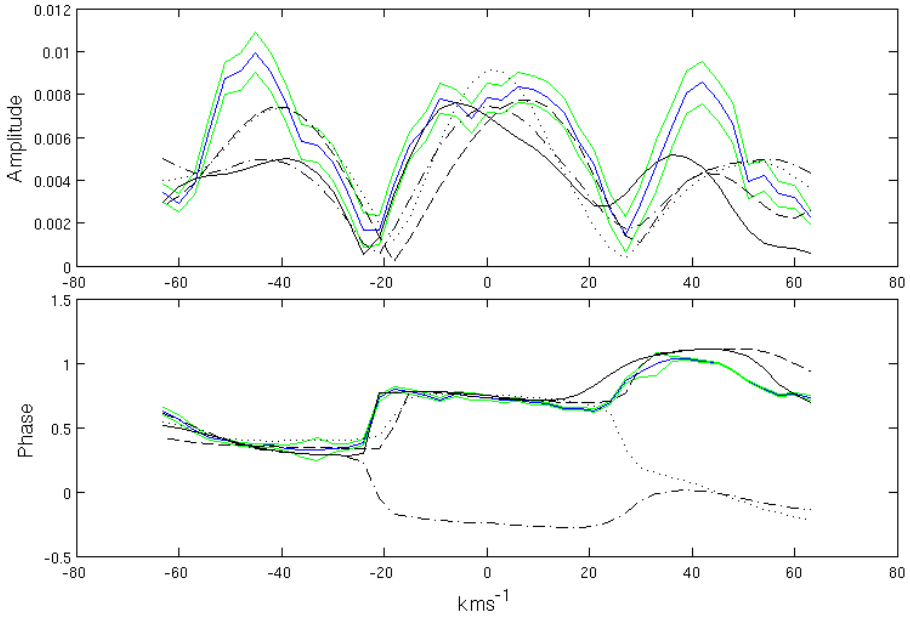

Figure 5.12: Best fitted modes for f_2 in QW Puppis. Here, as before, the observed amplitude and phase across the line are given by the blue line, with error bounds in green. The best fit of an $(l, m) = 1$, -1 mode is shown with a solid black line, the best fit of an $(l, m) = 1$, +1 mode is shown with a dashed line, the best fit of an $(l, m) = 4$, +1 mode (with the lowest χ^2) is shown with a dotted line, and the best fit of an $(l, m) = 4$, -1 mode is shown with a dash-dotted line.

l									
0					23				
1				18	22	14			
2			17	19	17	15	13		
3		22	21	11	8	10	7	7	
4	22	22	18	14	11	**4**	**3**	6	**3**
m	-4	-3	-2	-1	0	1	2	3	4

Table 5.9: Reduced χ^2 values for mode identification of f_3 in QW Puppis. The best fits are emboldened.

Table 5.8 displays the χ^2 values for the best fits to each of the modes attempted. The best fits obtained were for $l = 2$ or $l = 4$ and $m = \pm 1$. The χ^2 values for these best four modes are all very close. Figure 5.12 shows these fitted four modes to the deviation and phase profiles for f_2. Despite problems in the direction of phase transition for the two $l = +4$ modes, the phases do differ by an integer value from the observed profile and so are seen to be in phase after the phase transition. That these models were all fit with such similar χ^2 values means the discernment of the best fitting mode will likely be dependent upon the multimodal fitting in the subsequent section.

Table 5.9 displays the χ^2 values for the best fits of the various modes modelled for f_3. It is seen that there are three $l = 4$ modes that all fit the profile of f_3 fairly well. What is most pleasing about this is that what seem to be irregular peaks on the two maxima of the deviation profile are actually well modelled by the best fitting (l,m) = 4, +2 mode in Figure 5.13. Possible modes for $5 \leq l \leq 8$ were also examined with none showing a better fit (lower reduced χ^2) than those shown.

Attempts to carry out a mode identification of f_4 showed that the standard deviation profile and phase profile looked extremely similar to that of f_1, and when it was attempted to form a least squares fit to both simultaneously f_4's deviation profile was reduced to noise and the phase profile showed negligible phase transition across the profile. This strengthens the case that f_4 is an alias of the prior strong frequencies. Whilst this may seem a shame, it may have the benefit that modelling the pulsational behaviour of QW Puppis may be achieved with fewer non-radial modes.

5.5 Combined mode identification

For each of the frequencies f_1 to f_3 all combinations of the best fitting modes (emboldened in Tables 5.7, 5.8 and 5.9) were fitted. Each combination of these modes was optimised within the parameter space. It was found that fits for f_1 were well fitted by a (l,m) = 1, -1 or a 1, +1 mode. It may be reasoned that if this mode were the (l,m) = 1, +1 option then in the stellar reference frame this would have a negative frequency; which is unphysical. This is based on the assumed parameters for the star (Table 5.6) with an inclination of 68° from mode fitting optimisations. For the (l,m) = 1, -1 mode it is seen that in the stellar reference frame $f_1 = 0.74$ d^{-1} (with the intrinsic stellar rotational frequency at 0.68 d^{-1} calculated from the $v\sin i$, the inclination from mode-fitting, and a conservative radius estimate of 1.6M$_\odot$). This is an acceptable and physical solution. The four best combinations of modes are shown in Table 5.10. These fits were repeated several times with reduced χ^2 values varying less than 0.01 for each fit between repetitions.

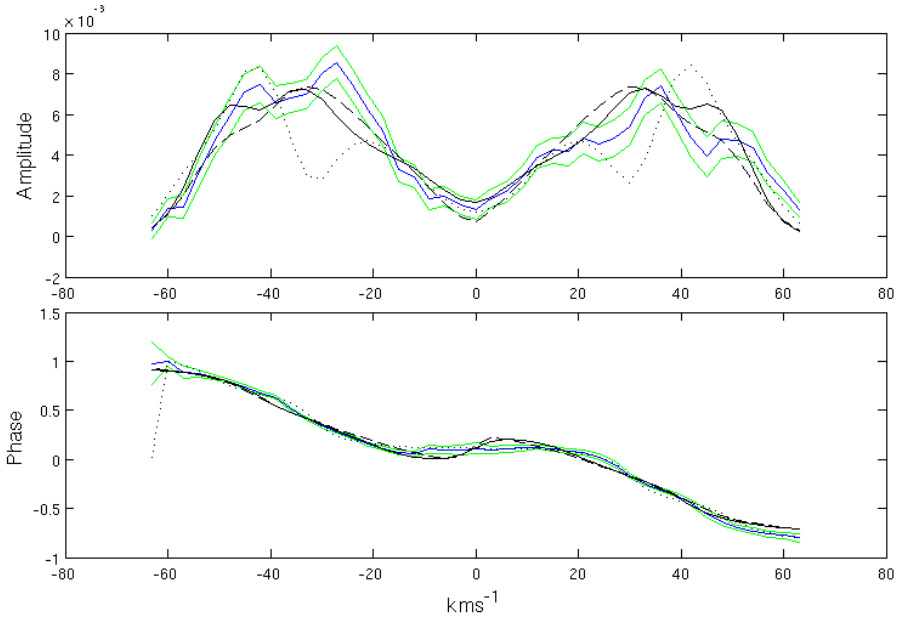

Figure 5.13: Best fitted modes for f_3 in QW Puppis. Here, as before, the observed amplitude and phase across the line are given by the blue line, with error bounds in green. The best fit of an $(l, m) = 4, +2$ mode is shown with a solid black line, the best fit of an $(l, m) = 4, +4$ mode is shown with a dashed line, and the best fit of an $(l, m) = 4, +1$ mode is shown with a dotted line.

	f_1		f_2		f_3	
Reduced χ^2	l,	m	l,	m	l,	m
27.0	1,	1	4,	-1	4,	2
27.8	1,	-1	4,	-1	4,	2
30.8	1,	1	4,	-1	4,	4
33.3	1,	-1	4,	-1	4,	4

Table 5.10: Reduced χ^2 values for multiple simultaneous mode identifications of QW Puppis. Only the l, m combinations with the lowest χ^2 values are shown.

That the optimised multimodal fitting is not markedly better for either of the f_1 $m = \pm 1$ scenarios makes the case for unambiguous mode identification of it as an (l,m) = 1, -1 mode weaker but of the two options this is the one that is physically viable. In the individual fits the m = -1 solution for f_1 displayed the lowest χ^2 value. A similar argument should be made for f_2 where again the ambiguity lies with $m = \pm 1$. This ambiguity is supported by Townsend (2003a) and Reese et al. (2012) in that prograde and retrograde modes with the same |m| can be quite similar in appearance.

It was found that individually the frequency f_1 was best modelled by an (l,m) = 1, -1 mode. f_2 was best modelled by an (l,m) = 4, -1 mode and f_3 was best modelled by an (l,m) = 4, +2 mode.

5.6 Summary

We obtained 463 spectra in 2004 and 2012 from MJUO and 122 from the SAAO for the study of QW Puppis. The SAAO data unfortunately could not be included due to dissimilarity of mean line profiles. Upon analysis, four frequencies were detected and three modes identified for QW Puppis. $f_1 = 0.055972 \pm 0.000004$ d^{-1}, $f_2 = 0.064846 \pm 0.000004$ d^{-1}, $f_3 = 5.219398 \pm 0.000002$ d^{-1}, and $f_4 = 2.9648 \pm 0.00009$ d^{-1}. The modes identified for the first three of these were f_1 a (1, -1) mode, f_2 a (4, -1) mode and f_3 a (4, +2) mode.

Chapter 6

IR Draconis: results from the multi-site campaign

In the study of IR Draconis, spectra from a number of different sites around the northern hemisphere were obtained. Those that gave the best data in terms of mean line profile ($>$ 40 spectra without change of CCD) were selected for LSD line profile construction. Those spectra obtained from the Okayama Astrophysical Observatory (OAO) (165 HIDES spectra), l'Observatoire de Haute-Provence (OHP) (90 SOPHIE spectra) and Roque de los Muchachos Observatory on La Palma Island (Canary Islands, Spain) (212 HERMES spectra) sites were used. The key features of these spectra are their observing times and high quality with dense observing runs obtained in March and July 2009 and January 2012 and smaller groups of spectra, obtained using HERMES on La Palma Island, interspersed between these groups of observations providing a measure of continuity in the data.

These spectra were reduced as described in Sections 2.3.1 to 2.3.3 and line profiles created as per Section 3.2. These line profiles were then scaled to have similar amplitudes for the creation of moments, pixel-by-pixel analysis, and mode identification. The line profiles from HERMES appeared to be of particularly high quality, and given the observing times (Figure 6.1), also of better sampling over possible pulsational phases. The mean of the HERMES line profiles was selected as the standard mean profile to which the other line profiles were scaled (Figure 6.2). In the HERMES profiles significant variation of the location of the centre of the line over time is seen. Some differences in the mean profiles are seen between the different sites.

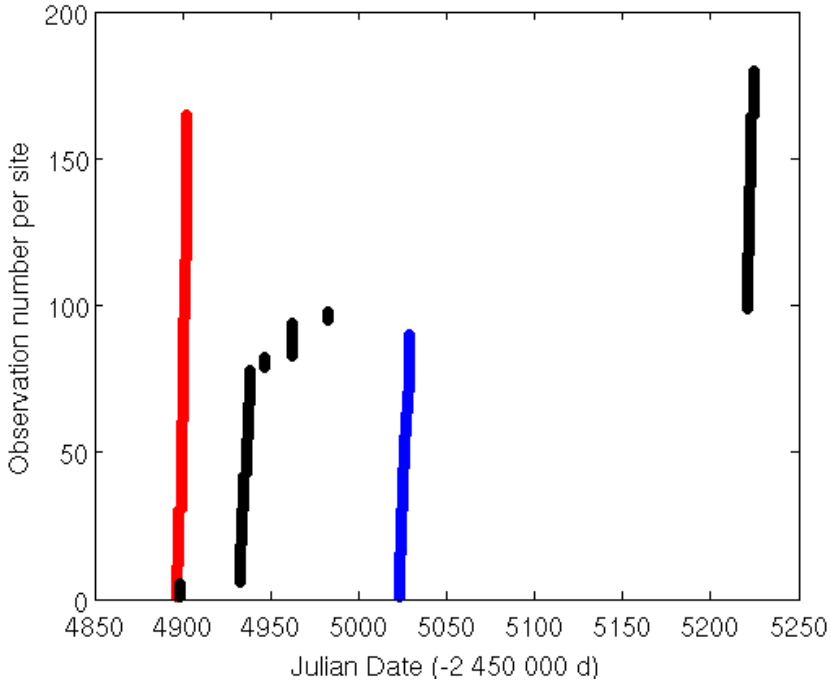

Figure 6.1: Julian Dates for acquisition of spectra of IR Draconis. Red is for OAO spectra, black is for HERMES spectra, and blue is for those from OHP.

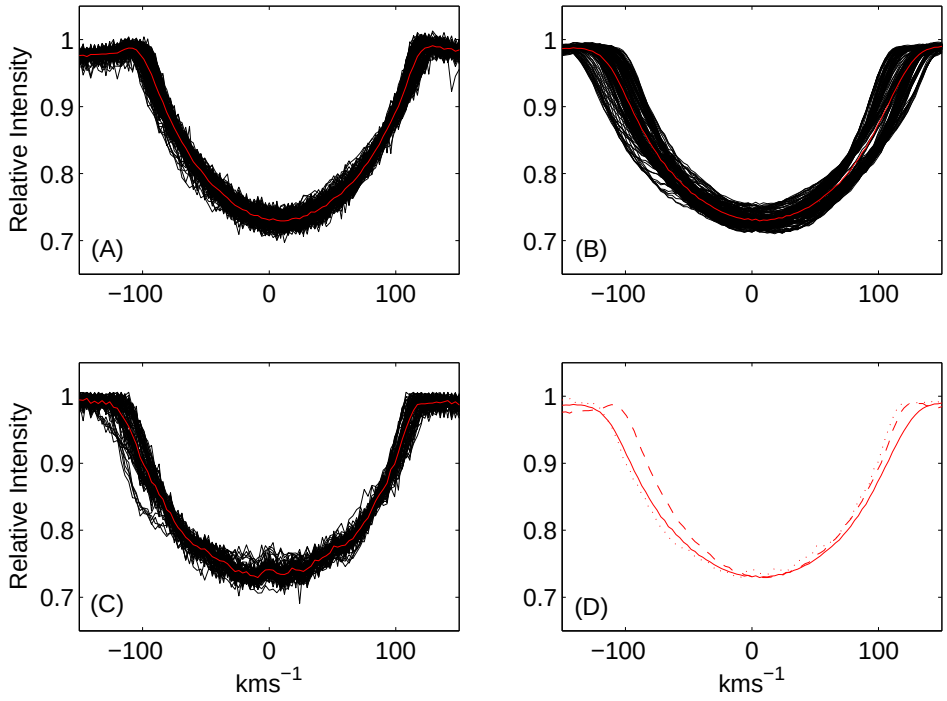

Figure 6.2: IR Draconis LSD line profiles. (A) OAO; (B) HERMES; (C) OHP. (D) the mean line profiles for each site where the OAO is shown as a dashed line, OHP is dotted, and HERMES is a solid line.

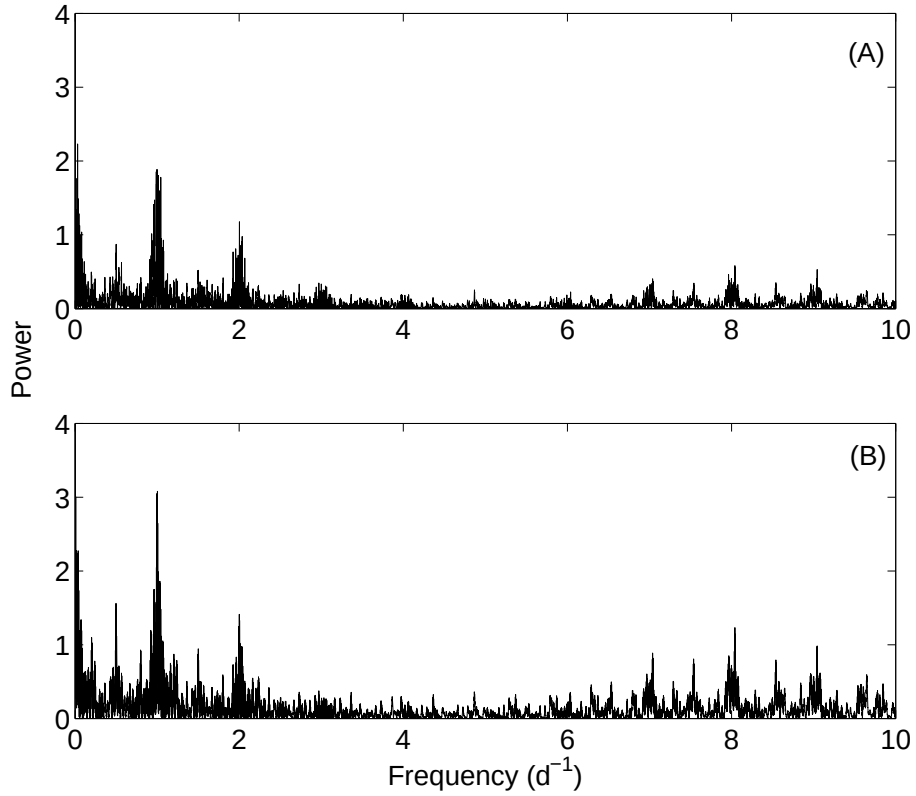

Figure 6.3: Spectral windows from observations of IR Draconis. (A) Spectral window from all observations combined, (B) HERMES observations.

6.1 Frequency analysis from moments

Spectral windows from HERMES observations, and from all observations combined are shown in Figure 6.3. The much less sharp 1 d^{-1} peak is seen from the multi-site data. The comparatively blunted peaks of the multi-site spectral window is expected when the observing times are spread over all hours of the day. Indeed, when the data are phased on a frequency of 1d^{-1} (as seen in Figure 6.4), there is only a small gap in data acquisition over a 1-day cycle.

Moments M_0 to M_3 were calculated using FAMIAS and analysed using SIGSPEC as described in sections 3.3 and 3.3. The results of the frequency extraction from the moments are shown in Table 6.1.

A number of frequencies appear in multiple moments. f_3 in M_0 is seen again as f_2 in M_2 and as f_5 in M_2 with a 1-day alias. f_2 in M_1 is repeated as f_2 in M_3 as well as f_{13} in M_2 from just the HERMES line profiles. Also seen in the HERMES data set alone are f_{14} and f_{15} which appear in both M_1 and M_3. A number of of 1-day aliases are also visible.

What is interesting is the detection of frequencies in M_0 (equivalent width) with $f_3 = 2.3885$ d^{-1}. This means that there is some periodic equivalent width variations indicating some non-adiabatic activity in this system of pulsations. If the photometry from Henry et al. (2005) had been obtained and phased upon f_3 in M_0 it may have been interesting to see if the detected variations occurred one half cycle out of phase as expected for luminosity variations.

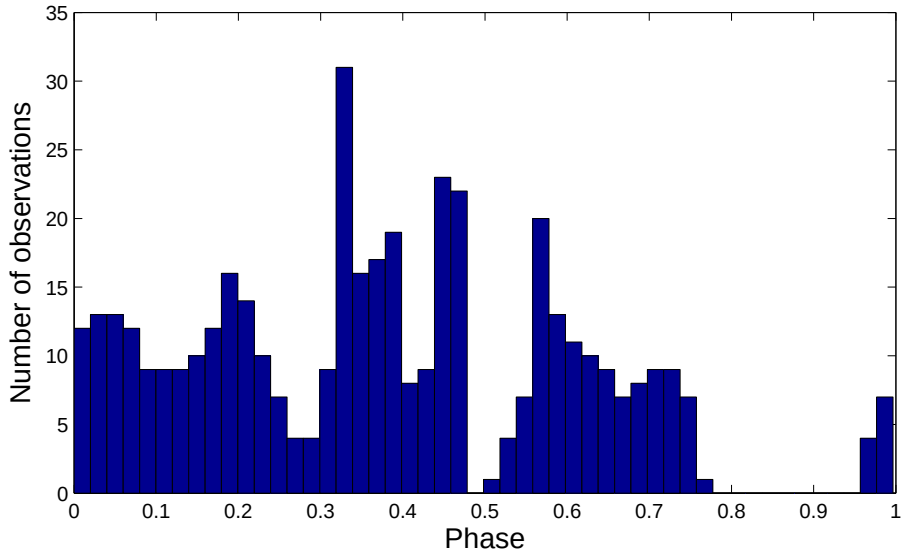

Figure 6.4: Spectra collected for IR Draconis phased on a frequency of $1\mathrm{d}^{-1}$. This, while not perfect, does show what can be achieved with multiple sites observing the same target.

	M_0		M_1		M_2		M_3	
	Frequency d^{-1}	$sig(f)$	Frequency d^{-1}	$sig(f)$	Frequency d^{-1}	$sig(f)$	Frequency d^{-1}	$sig(f)$
f_1	1.0033	80	**0.0049**	79	0.0101	62	0.0028	72
f_2	3.0062	44	**2.3554**	39	**2.3808**	48	**2.3557**	53
f_3	**2.3885**	15	0.9503	22	0.9686	19	2.2392	20
f_4	5.8346	20	0.5067	21	1.2851	20	2.4311	21
f_5	0.8832	14	3.1295	23	**3.3883**	14	2.5558	25
f_6	0.5034	12	5.8991	15	2.7546	18	3.1791	21
f_7	2.7759	11	4.5986	16	1.4855	18	4.7111	19
f_8			1.6739	23	6.7772	18	6.1616	18
f_9			8.5182	13	6.1091	18	5.3511	13
f_{10}					6.6800	12	2.9397	13
f_{11}					11.1954	12	9.5918	15
f_{12}							12.8358	12
f_{13}	0.0572	22	0.0017	35	**2.3554**	28	0.0015	32
f_{14}	0.2501	15	**2.3627**	28	4.0485	15	**2.3626**	29
f_{15}	3.8526	13	**2.7352**	13	3.7112	14	**2.7356**	12
f_{16}			6.6471	12	0.1258	13	6.6509	12
f_{17}			6.0170	13	7.8267	12	4.0520	12
f_{18}					15.5735	11	6.0005	12

Table 6.1: Frequencies from analysis of moments from LSD profiles obtained from the complete dataset (upper panel) and from the HERMES data in isolation (lower). Frequencies for the zeroth (M_0) to third (M_3) moments are shown. In bold are those frequencies found in multiple moments or also in the pixel-by-pixel analysis.

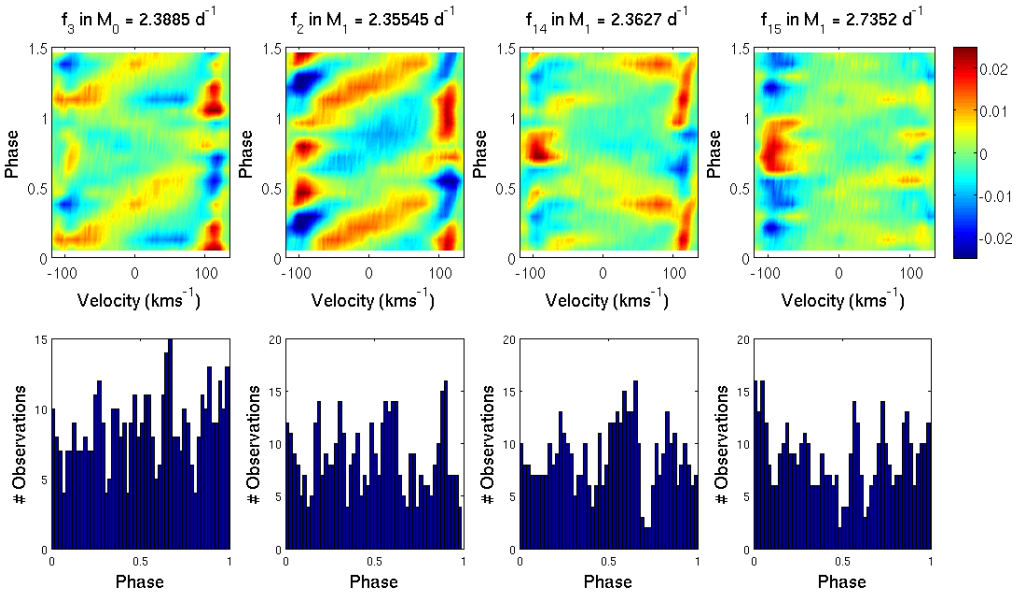

Figure 6.5: Line profile variation phased to the frequencies determined from the analysis of moments. Those frequencies seen in bold in the first two moments in Table 6.1 have had the line profiles phased to them. These frequencies are duplicated in the higher moments and those are not shown.

When the line profiles are phased on the commonly appearing frequencies (in bold in Table 6.1) some strongly defined line profile variations are seen (Figure 6.5). f_2 in M_1 appears to have strongly defined line profile variation over once cycle.

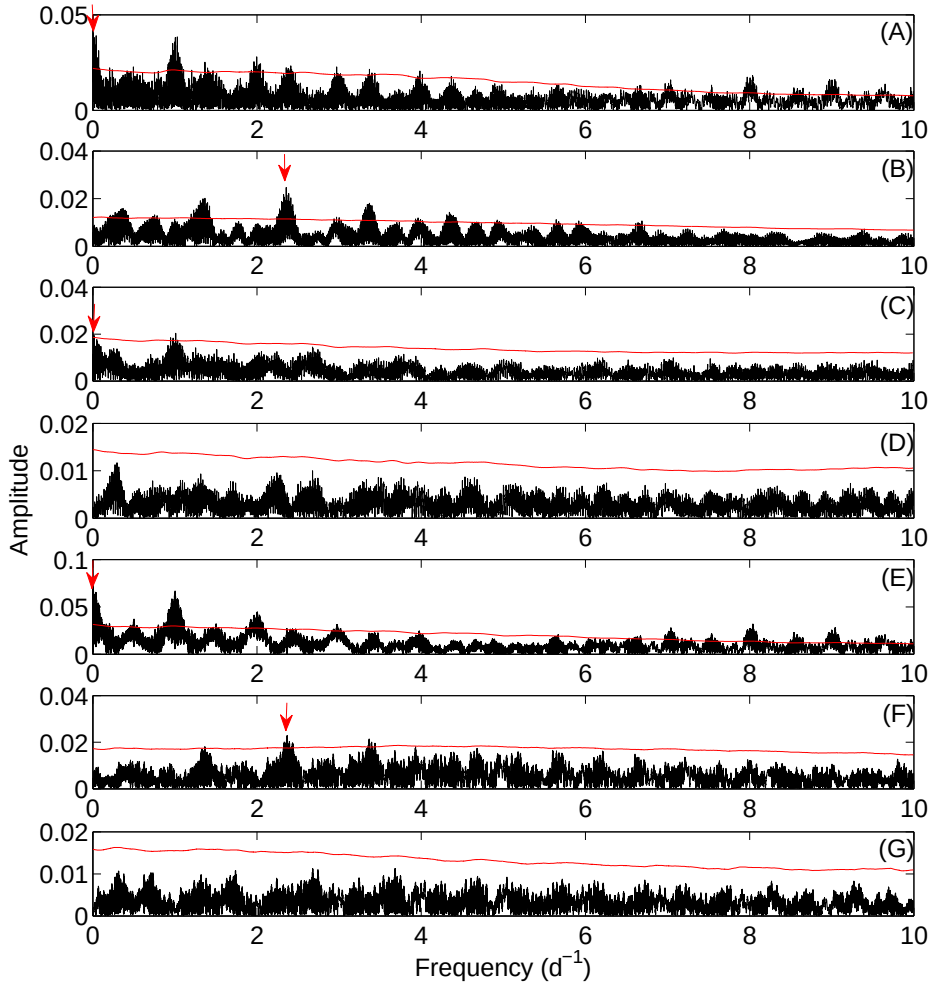

Figure 6.6: Pixel-by-pixel Fourier spectra with noise levels in red for IR Draconis. (A) — (C) Spectra for f_1 to f_3 from all observations. (D) No significant frequency above the noise floor. (E) and (F) Spectra for f_4 and f_5 from only the HERMES observations. (G) As for (D) but from the HERMES observations. Small red arrows show the most significant peak for each frequency.

6.2 Frequency analysis from pixel-by-pixel method

The analysis of the line profiles using the pixel-by-pixel method was also undertaken. The Fourier spectra for the pixels with the greatest amplitude are shown in Figure 6.6, each subsequent frequency is found after removing the prior by prewhitening. Surprisingly few frequencies were found in this method when compared with those found from the moments. The first frequency found, shown in Table 6.2 ($f_1 = 0.00515 \pm 0.00003$ d^{-1}) is very low considering what is typical for γ Doradus frequencies. 1-day aliases of this frequency were examined showing generally unremarkable line profile variation, and no improvement over that of f_1.

f_1 corresponds to a period of 184.7 days. As this was suspiciously close to half a year period, the barycentric corrections were checked. The line profile variation is strong but not continuously defined across the profile (Figure 6.8) with most of the variation occurring

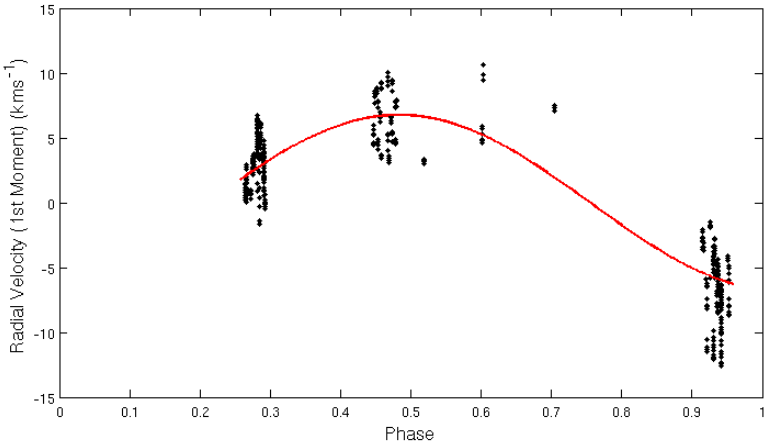

Figure 6.7: Best fit to f_1 in M_1 weighted by the normalised weights from line profile generation. The observations were phased on $f_1 = 0.005202$ d^{-1}.

in the wings of the line. The problem with such a low frequency is that its long period is not well-sampled over the whole cycle, and very few phases were sampled (see Figure 6.8). However, as seen for both HD189631 and QW Puppis, the presence of low frequencies may merely indicate the presence of a mode with a negative m. Without a good reason for discarding it, this frequency was retained for analysis.

The frequency f_1 from the pixel-by-pixel analysis is similar to that of f_1 in M_1 and twice f_2 in M_2 as well. Calculating the radial velocity (first moment) from all the line profiles and fitting a sine curve with the parameters of the highest peak in the Fourier spectrum ($f_1 = 0.005202$ d^{-1}, an amplitude of $A = 6.494 \pm 0.115$ kms^{-1}, and a phase of $\phi = 0.65595 \pm 0.00418$) and it is seen that this frequency is quite reasonable as illustrated in Figure 6.7).

The frequency f_2 (and f_5) from the pixel-by-pixel method are seen in the analysis of moments M_1 and M_3. The strong 2.35538 d^{-1} frequency ($P = 0.42456$ d) found in the moments and in the pixel-by-pixel methods (Figure 6.8) is also seen in the literature. Aerts et al. (1998) reported two periods of $P_1 = 0.4245$ d and $P_2 = 0.4458$ d, Henry et al. (2005) reported five periods, which were $P_1 = 0.42450$ d, $P_2 = 0.44583$ d, $P_3 = 0.40533$ d, $P_4 = 0.39830$ d, and $P_5 = 0.48797$ d . Both primary periods P_1 from these papers match well as they were both the periods of strongest frequencies found in these studies. In the analysis of our data we do not see the additional frequencies found in these papers. There is no small group of five frequencies previously found by Henry et al. (2005). It is conceivable that these five frequencies are the result of rotational splitting of an $l = 2$ mode with further modulation of their spacings so they appear asymmetric in their spacing about the strong main frequency. However these were not similarly found by Aerts et al. (1998), nor are they found here. Phasing the line profiles to the frequencies found in the literature may be seen in Appendix C.

The frequencies in Table 6.2 had all the line profiles phased to them (Figures 6.8 and 6.9). The variation of f_2 (and the similar f_5) appears to be well-defined, it is also well-sampled across the cycle. Whilst strong, the variation of f_1 is not well sampled over the phase, but as will be seen in Section 6.3, the deviation profile across the line is quite well defined if a little asymmetrical.

f_3 is not well defined in the phased colour plots, (Figure 6.8) just as f_1 is atypical

	Frequency		Period	
	d^{-1}	$\sigma(f)$	d	$\sigma(f)$
f_1	0.00515	0.00003	194.2	1.1
f_2	2.35538	0.00004	0.42456	0.00001
f_3	0.01372	0.00006	72.9	0.32
f_4	0.00178	0.00005	561.8	16
f_5	2.35890	0.0001	0.42393	0.00002

Table 6.2: Frequencies from the pixel-by-pixel analysis of LSD profiles obtained from all sites (upper panel) and from HERMES data in isolation (lower). Uncertainties were estimated using Equation 3.8.

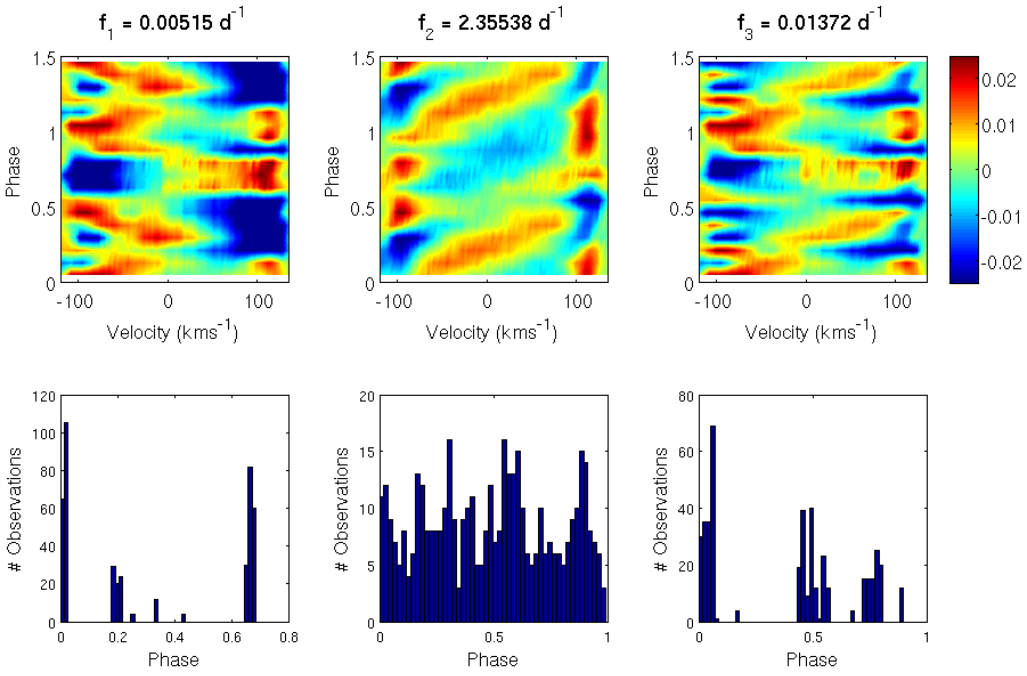

Figure 6.8: Line profile variation phased to f_1 to f_3 from pixel-by-pixel analysis.

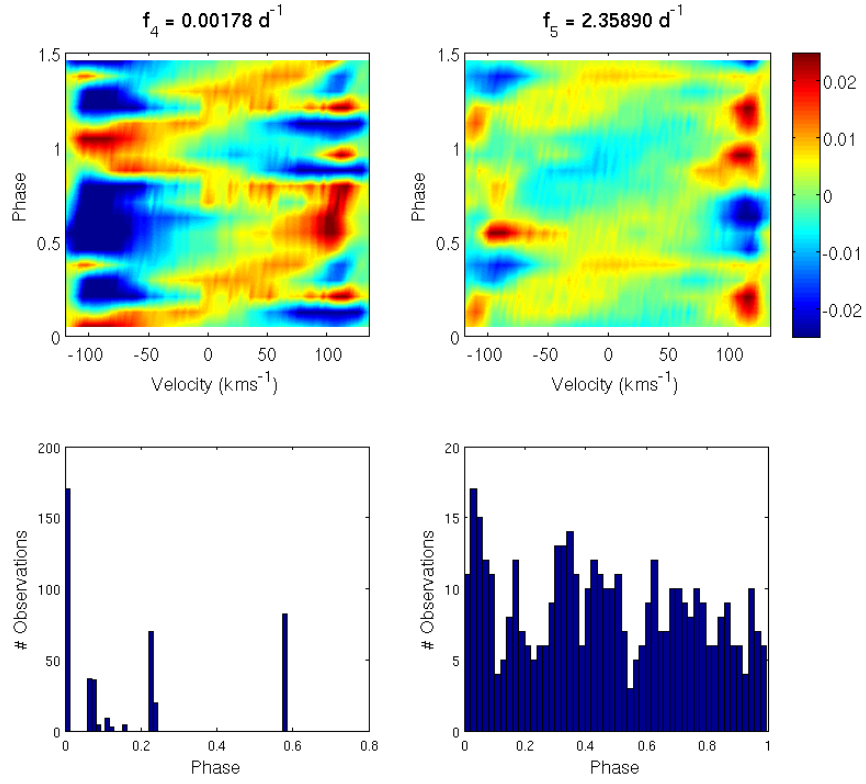

Figure 6.9: Line profile variation phased to f_4 and f_5 from pixel-by-pixel analysis.

of non-radial pulsations. The phase sampling is rather non-uniform (Figure 6.8) and so the coloured plot seems discontinuous. f_3 is significantly more than twice f_1 and so not an obvious alias. When mode identification was attempted for f_3 after removing f_1 by prewhitening the variation too was largely removed, suggesting that f_3 is related to the frequency f_1. For this reason f_3 was not included in the set of frequencies for mode identification.

R	1.2 — 1.8 $R_\odot$
M	1.5 — 1.6 $M_\odot$
T	7180K
log$g$	4.01
$[Fe/H]$	-0.14
Equivalent width	40 — 50 kms^{-1}
d(EW)/d(T)	-0.8 — 0.8 kms^{-1}/K
$v$sin$i$	100 — 130 kms^{-1}
inclination	15°— 90°
Intrinsic width	10 — 20 kms^{-1}
Zero-point shift	6 — 7 kms^{-1}
l	0 — 4
m	-4 — +4
Amplitude	0.01 — 120 kms^{-1}
Phase	0 — 1

Table 6.3: The parameters used for initial generation of models for mode identification of the frequencies found in IR Draconis.

6.3 Independent mode identification

Initial fits of over 10^5 models to the mean line profile using the parameters set in Table 6.3 found a $v$sin$i$[a] of 115.6 kms^{-1}, which is in good agreement with the value obtained by Fekel et al. (2003) of 115 kms^{-1}. A best mass value of 1.554 $M_\odot$ was also obtained, which was in agreement with Aerts et al. (1998) and Plavchan et al. (2009) who reported masses of 1.5 $M_\odot$ and 1.56 $M_\odot$ respectively. The values obtained here are not intended to provide new determinations of these parameters, but to confirm that the line profiles and subsequent analyses are comparable to prior examinations of IR Draconis.

Mode identification with FAMIAS for IR Draconis was done using 3000 segments over the stellar surface as compared to 1000 segments for HD 189631 and QW Puppis. This is due to the higher $v$sin$i$ of this star requiring a larger number of points to adequately sample the surface velocity vector field.

The lower bound for stellar inclination was obtained using a $v$sin$i$ of 115.6 kms^{-1}, a mass of 1.56 $M_\odot$, and an estimated radius of 1.6 $R_\odot$ to obtain a critical inclination of 15°, below which Keplerian equatorial breakup would be approached. The detection of significant frequencies in the zeroth moment suggested the presence of some non-adiabatic component so an additional term (dEW/dT) was included in the model to account for this in Table 6.3.

The frequencies used for this identification of modes are f_1 andf_2 from Table 6.2. A group of models was optimised for each possible mode in the range of l and m from Table 6.3. In the fitting of the frequencies for this star the mean line profile was also fitted. This was done to improve the rather poor fits of the pulsational amplitudes and phase over the line profile. This does not introduce additional variables since the stellar mass and projected rotation rate are quite well constrained. This does however dramatically inflate the reduced χ^2 value obtained in the case of a poorly fitting model. However, those that

[a]An uncertainty for this value and that of the mass is not given as it would probably have had to be determined from the geometry of the reduced χ^2 values of the line profile fit about the optimal value. The shape of this arrangement need not necessarily be a gaussian nor any other regular distribution.

l									
0					66360				
1				**146**	149703	**185**			
2			273	407	137476	417	285		
3		354	325	764	138596	947	294	323	
4	442	484	452	1264	130382	1224	356	345	333
m	-4	-3	-2	-1	0	1	2	3	4

Table 6.4: Reduced χ^2 values for mode identification of f_1 in IR Draconis. The best fits are emboldened.

l									
0					82				
1				81	85	**42**			
2			**66**	116	109	92	***40***		
3		126	111	113	92	112	*76*	***53***	
4	143	141	123	78	90	125	*79*	*68*	*62*
m	-4	-3	-2	-1	0	1	2	3	4

Table 6.5: Reduced χ^2 values for mode identification of f_2 in IR Draconis. The best fits are emboldened. Italicised fits are those later ruled out as non-physical. The lower limits of inclination used here are $i = 15°$ for all values of m apart from $m = 1$ which was 37°.

fit poorly are generally not of interest.

The analysis of the low frequency, $f_1 = 0.00515$ d^{-1}, was a little uncertain as the amplitude profile was poorly fit. The variation across the line was located mostly in the wings and was asymmetric as well. The large amplitude of variation compared to that of HD 189631 and QW Puppis means that the reduced χ^2 values obtained (Table 6.4) are a great deal larger than those found in the mode identification of the prior two stars HD 189631 and QW Puppis due to the magnitude of any differences obtained between the observed and the model applied, and the addition of the fit to the mean line profile.Given that $f_1 = 0.00515$ d^{-1}, we may assume that m is negative, otherwise the frequency would be negative in the reference frame of the star. Models including positive m values were still optimised in FAMIAS for completeness. f_1 was best fit with an $(l,m) = 1, -1$ mode, closely followed by an $(l,m) = 1, +1$ mode (Table 6.4). These fits seemed to poorly model the large amplitude variation both in the wings of the line profile and the more uniform mid-section of the line. Given the admittedly poor phase-sampling over the pulsational phase it was unanticipated that the phase profile would be as continuous as it appears in Figure 6.10. Given the mediocre phase sampling, the direction of the phase transition in the middle of Figure 6.10 is perhaps questionable, casting further doubt as to certainty of the distinction between $m = 1$ and $m = -1$.

The individual mode identification of f_2 for IR Draconis finds an $(l,m) = 2, +2$ mode to be the best candidate with a reduced χ^2 value of 40, followed by an $(l,m) = 1, +1$ with a reduced χ^2 of 42, the next best option is an $(l,m) = 3, +3$ with a reduced χ^2 of 53 (Table 6.5). Comparing these two fits to the observed clearly demonstrates the superior fit of the $(l,m) = 2, +2$ mode both in phase and in amplitude (Figure 6.11).

A prograde mode ($m > 0$) must have a frequency greater than the intrinsic stellar rotational frequency. FAMIAS unfortunately allows the fitting of non-physical modes. With

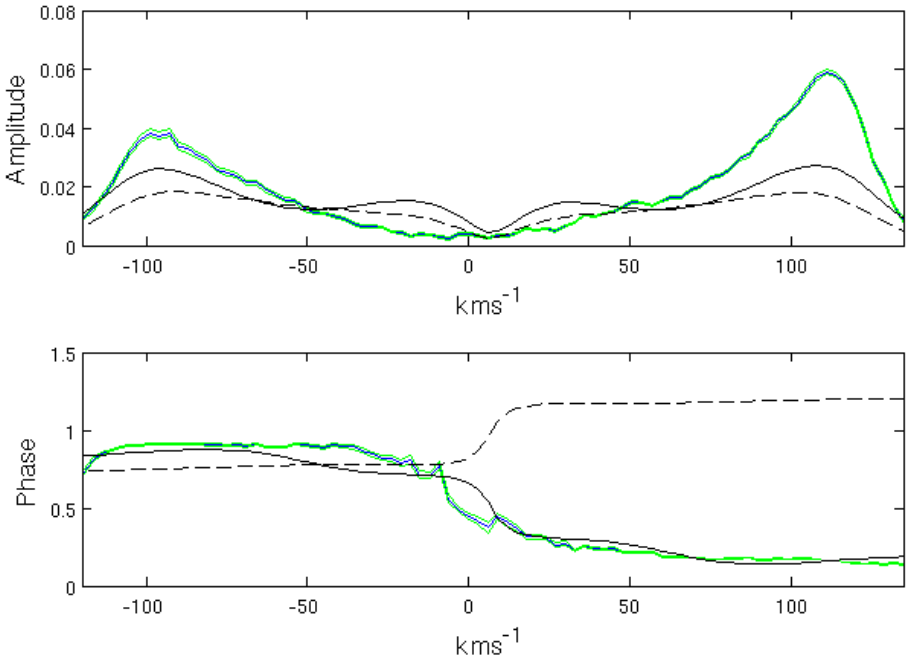

Figure 6.10: Best fitting modes for f_1 in IR Draconis. The observed amplitude and phase across the line is given by the blue line, with error bounds in green. The best fit of an $(l,m) = 1,-1$ mode is shown with a solid black line, and of an $(l,m) = 1,1$ by the dashed line.

a little familiarity it can be suspected that f_1 may not be fitted with $m \geq 1$, and fortunately the best fit for f_1 finds $m = -1$. What is not so readily apparent is that for such a rapidly rotating star, limits of inclination constrain the modes viable for fitting to f_2 as well. It has been shown that f_2 was best fit with an $(l,m) = 2,+2$ mode, but if this were done, then it would appear as a negative frequency in the stellar reference frame. In fact it is found that for $m \geq 2$ no inclination above i_{crit} will give a physically realisable mode, and for $m = 1$ the inclination must be 37°or greater. This results in the frequency for the mode being greater than, or equal to, the rotational frequency for the star ($f > 0$ d^{-1} in the stellar reference frame). The mode optimisations were repeated utilising the constraints that $i > 37$°and $m = 1$, and these new results are shown in Table 6.5.

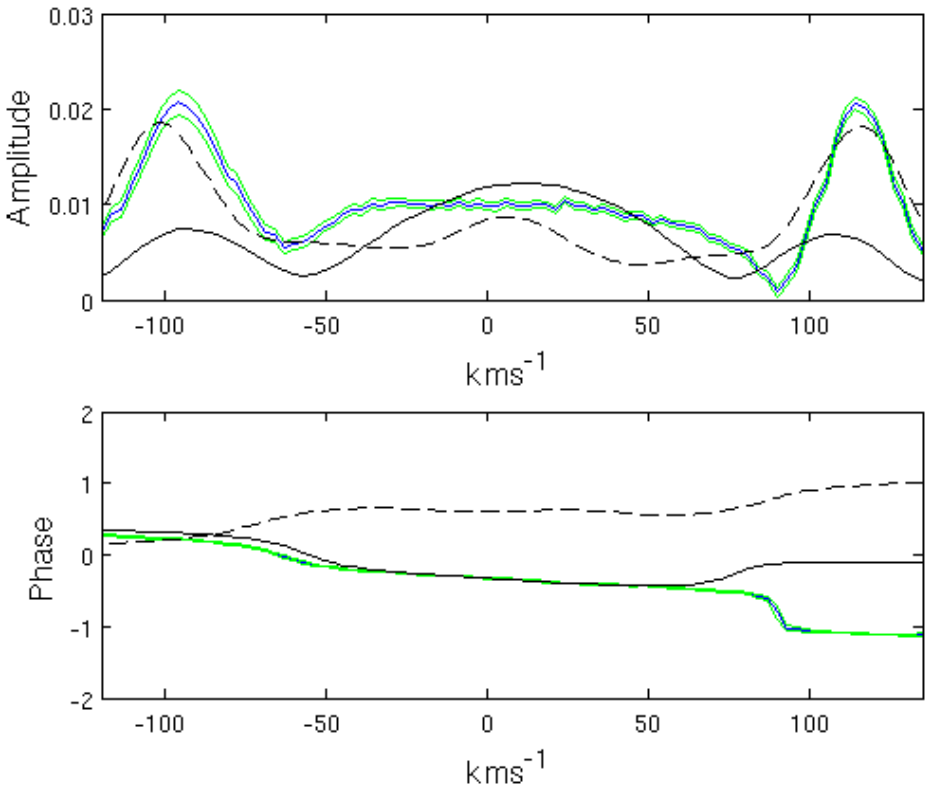

Figure 6.11: Best fitting modes for f_2 in IR Draconis. The observed amplitude and phase across the line is given by the blue line, with error bounds in green. The best fit of an $(l,m) = 1, +1$ mode is shown with a solid black line, and of an $(l,m) = 2, -2$ by the dashed line. Note again that a difference in phase of an integer amount shows that both lines are in phase with each other.

Reduced χ^2	f_1 l,	m	f_2 l,	m
111	1,	-1	1,	1
131	1,	1	2,	-2
146	1,	1	2,	-2
183	1,	-1	1,	1

Table 6.6: Reduced χ^2 values for multiple simultaneous mode identifications of IR Draconis. Only the l, m combinations with the lowest χ^2 values are shown.

6.4 Combined mode identification

Combined mode identification was undertaken for IR Draconis. Optimisations were carried out for both frequencies f_1 and f_2 simultaneously using the best fitting frequencies from the individual mode identifications. Despite only using phyically plausible modes for f_2, f_1 was allowed to vary over $-1 < m < 1$ as no other mode fit comparably well in the individual fits. Table 6.6 shows the optimised simultaneous fits of f_1 and f_2. In models where f_1 was prograde, the incliniation was set to ensure this was at least physically possible.

Given that the frequency f_1 should have a negative m to be a physical frequency in the stellar reference frame, the (l,m) $= 1, -1$ was the best fit for this frequency individually, and the selection of the $m = -1$ mode was made. f_2 was best fit with an (l,m) $= 1, +1$ mode and again this was supported in the multimodal fit.

6.5 Summary

425 spectra from three sites were used to analyse frequencies apparent in IR Draconis. $f_1 = 0.00515 \pm 0.00003\mathrm{d}^{-1}$ was best fit with an (l,m) $= 1, -1$ mode, and $f_2 = 2.35538 \pm 0.00004\mathrm{d}^{-1}$ was best fit with an (l,m) $= 1, +1$ mode (with an inclination above 37°). These results are supported by simultaneous fitting of both frequencies.

Chapter 7

Discussion

Spectra from three γ Doradus stars were analysed, frequencies were found and the best-fitting modes for each frequency determined. The key findings of this study are presented in Table 7.1. The cross-correlation method employed by Maisonneuve et al. (2010), Davie (2011), Maisonneuve et al. (2011) and Brunsden et al. (2012a,b) was used for creating line profiles for HD 189631.

An improved method was applied in the examinations of QW Puppis and IR Draconis. This method minimises the contribution of blended lines in the formation of a combined line profile. This method showed improvement in the treatment of stars with more rapid rotation.

In this spectroscopic study of three stars, one or more of the frequencies found agreed with those from prior studies of each star. The addition of fifty-eight more spectra to those used in Maisonneuve (2010) enable a reanalysis of HD 189631. All four of the frequencies found in this study agree very well with those found by Maisonneuve (2010). However, the modes identified here are different for f_2 and f_4 than found previously. The mode identified for f_2 by Maisonneuve (2010) was that of an $(l,m) = 3, -2$, in this study is reported an $(l,m) = 1, +1$. Similarly or f_4 where previously was found an $(l,m) = 4, +1$, here is reported an $(l,m) = 1, +1$ mode. The other two modes identified are consistent with the prior results.

In the analysis of QW Puppis, 402 new spectra were obtained in 2012 at MJUO and combined with those from the past work by Wright (2008). The first frequency found by Wright (2008) was obtained as a combination of f_1 and f_2 in this study, itself an alias of a frequency found in Poretti et al. (1997). Equation 1.5 tells us that as the observed frequency approaches zero, for the corotating frequency to remain positive, m must be negative. Two relatively low frequencies for this star, f_1 and f_2 (Table 7.1), were identified with modes having $m = -1$.

A multisite campaign was organised for the study of IR Draconis. From three observatories, 425 specra were obtained and analysed. The first frequency found by Aerts et al. (1998) and Henry et al. (2005) corresponds very well with f_2 in this study (Table 7.1). This frequency was identified with an $(l,m) = 1, +1$ mode. A very low frequency was found also (f_1), and identified with an $(l,m) = 1, -1$ mode. Because of the very long period, the pulsational phase of f_1 here was poorly sampled. This period is long enough that it could perhaps be a binary system with a low-mass secondary, but there is no suggestion of this in the literature.

The detection of lower frequencies is only possible through the use of a long observing timebase to adequately sample these long periods. Each low frequency was identified as having a retrograde mode ($m < 0$). This is a little problematic as the pulsational frequency will be similar to the intrinsic rotational frequency of the star for these frequencies. Without well-determined inclinations for these stars, the stellar rotational frequency will be poorly determined, and so will the pulsational frequency in the stellar reference frame. These

	Frequency d^{-1}	Period d	Mode l	m
HD 189631				
f_1	$1.6774 \pm 2\times10^{-4}$	$0.59616 \pm 7\times10^{-5}$	1,	+1
f_2	$1.4174 \pm 2\times10^{-4}$	$0.7055 \pm 1\times10^{-4}$	1,	+1
f_3	$0.0714 \pm 2\times10^{-4}$	$14.01 \pm 4\times10^{-2}$	2,	–2
f_4	$1.8228 \pm 2\times10^{-4}$	$0.54861 \pm 6\times10^{-5}$	1,	+1
QW Puppis				
f_1	$0.0556 \pm 4\times10^{-4}$	$17.866 \pm 1\times10^{-3}$	1,	–1
f_2	$0.0648 \pm 4\times10^{-4}$	$15.421 \pm 1\times10^{-3}$	4,	–1
f_3	$2.9648 \pm 1\times10^{-4}$	$0.1915930 \pm 1\times10^{-7}$	4,	+2
IR Draconis				
f_1	$0.00515 \pm 3\times10^{-5}$	194.2 ± 1.1	1,	–1
f_2	$2.35538 \pm 4\times10^{-5}$	$0.42456 \pm 1\times10^{-5}$	1,	+1

Table 7.1: Summary of frequencies found for HD 189631, QW Puppis and IR Draconis and the modes identified for each.

low frequencies have periods such that, without prior knowledge, the full period is unlikely to be well-sampled. This can lead to ill-defined phase transitions across the line profile variation and so a challenging identification of the associated mode. Future spectroscopic analyses of this nature would do well to analyse some of their spectra early in the hope of identifying these possible low frequencies. Thus it would be possible to tailor the rest of the observing campaign to collect spectra so that potential periods are well sampled.

The single aspect of this work that was the most challenging was that of combining the multi-site data. Whilst having spectra from different longitudes allows for closer-to-continuous observing, the different treatments and generally absent documentation about what exactly was done to the spectra made handling these spectra very time consuming. If not for private communication with Dr. Eiji Kambe (the observer) via Dr. Peter De Cat, the data treatment of the OAO spectra would have been very challenging and awareness of order effects above 700 nm may have been missed. The observing log for these spectra contained just dates, times of exposure, lengths of exposure, count per pixel, and the file names. This is nowhere near the detail included in the standard FITS headers. Multi-site data really need to be collated with adequately recorded descriptions of the way in which they were collected and treated. This is critical to the usefulness of these data. There were not enough spectra from some sites to give a representative mean line profile. This is not to say that the spectra were bad, merely that there were too few in this instance.

The use of the LSD method in this study led to the spectroscopic mode identifications of IR Draconis. To date, IR Draconis has the highest $v\sin i$ (115 kms^{-1}) of any main sequence star with a spectroscopic mode identification after the abnormal γ Doradus star, HD 209295, with a $v\sin i$ of 98±10 kms^{-1}(Handler et al., 2002). The application of this technique should be reasonably straight-forward for other stars with similar behaviours, like KIC 8054146 (Breger et al., 2012), given that the spectra for such an analysis have already been obtained. Indeed a great deal of ground-based spectroscopic follow-up work is foreseen to examine some of the better and more interesting targets from the *Kepler* photometry.

The study and understanding of non-radial pulsations of γ Doradus stars is at a particularly exciting stage. Why particular modes are excited and detected is still poorly understood. The pendulum between observation and theory is preparing to swing back to the domain of the theoreticians. The time of the CoRoT satellite has ended, and the analysis of *Kepler* satellite photometry is well underway. The theory and modelling groups now need to develop good models of these stars, to help understand and explain the growing weight of spectroscopic mode identifications and the large number of expected modes from the *Kepler* photometry.

Chapter 8

Conclusions and Future Work

Several spectroscopic observing campaigns were carried out to obtain spectra of the three stars studied. These spectra were used to create cross-correlated line profiles and, for HD 189631, frequencies were found from these using Fourier methods and models optimised to fit pulsational modes to these frequencies using FAMIAS. The frequencies and modes identified for HD 189631 were $f_1 = 1.6774 \pm 0.0002$ d^{-1} with an $(l,m) = (1,+1)$ mode, $f_2 = 1.4174 \pm 0.0002$ d^{-1} with an $(l,m) = (1,+1)$ mode, $f_3 = 0.0714 \pm 0.0002$ d^{-1} with an $(l,m) = (2,-2)$ mode, and $f_4 = 1.8228 \pm 0.0002$ d^{-1} with an $(l,m) = (1,+1)$ mode.

In the analysis of QW Puppis, a least-squares deconvolotion method was implemented and compared with that of line profiles formed by the more simple cross-correlation method. It was found that this method performed as well or better than the prior and so was used subsequently. The analysis of QW Puppis identified modes for three frequencies, these were $f_1 = 0.055972 \pm 0.000004$ d^{-1} with an $(l,m) = (1,-1)$ mode, $f_2 = 0.064846 \pm 0.000004$ d^{-1} with an $(l,m) = (4,-1)$ mode, and $f_3 = 5.219398 \pm 0.000002$ d^{-1} with an $(l,m) = (4,+1)$ mode.

The analysis of the rapidly rotating star IR Draconis identified two frequencies: $f_1 = 0.00515 \pm 0.00003$ d^{-1} with an $(l,m) = (1,-1)$ mode, and $f_2 = 2.35538 \pm 0.00004$ d^{-1} with an $(l,m) = (1,+1)$ mode.

These findings build upon the number of γ Doradus stars with identified modes, and find a number of retrograde ($m < 0$) modes. There is still work to be done in the determination of the stellar parameters of these stars for modelling and in the ongoing development of the methods of analysis of these pulsations.

The determination of effective temperature and metallicity of the stars analysed in this work has, for the most part, been carried out previously. In all cases they were calculated from very few or one spectrum.

A large number of good spectra are used in this work and it is proposed that an excellent mean spectrum incorporating *all* phases of pulsation be used for metallicity analysis given that this is calculated using variable spectral lines. The equivalent widths, however, should not change significantly with time as there is usually no temperature variation associated with these pulsations, although frequencies in the zeroth moment were seen in IR Draconis.

It would be useful to test this assumption and also to see if a relatively automated metallicity determination technique, such as MOOG (Sneden, 1973), experiences any phase related variation as a result. If phase-related variation is found then this would mean that one could not use just one isolated observation of a g-mode pulsator to obtain a representative metallicity. Phase-binning of these spectra, by one or more of the dominant frequencies, may show any variation reasonably well. It is expected that the answer should be negative, but experimental verification of this would be welcome. A linelist for this analysis has been prepared and is found in Appendix D.

In the calculation of cross-correlated line and LSD profiles, a line-mask was used in which the delta-funtions in the line-mask are scaled by the equivalent widths of the line.

This weights the cross-correlated profile contribution by the strength of the line and therefore by the amount of signal. However, further weighting may be beneficial. It is suggested that additional weighting of each line by the excitation potential particular to that line may better treat the small differences in line profile variation on a line-by-line basis.

Acknowledgements

I would like to thank my supervisors Dr Karen Pollard and Prof. Peter Cottrell for their invaluable patience, guidance, and high expectations through this project and Emily Brunsden for her feedback and deep experience in this field.

I'd also like to thank Drs Peter De Cat and Duncan Wright for their spectra, and Duncan for his assistance in November in implementing and debugging the LSD code. I would like to thank all the observers for the time they spent observing for this and related projects.

Thanks also to the Marsen Fund committee for supporting new and exciting research, and the Dennis William Moore Scholarship committee for awarding me their scholarship this year. Generous financial support is hard to come by and greatly appreciated where it affords a modicum of freedom from the additional pressures of life.

Appendix A

Least-squares deconvolution Matlab script

```
function LSD = compute_LSD(wave,int,errs,wavelengths,widths,del_v,velpixlim)

%LSD = compute_LSD(wave,int,errs,wavelengths,widths,del_v,velpixlim)
% wave       = wavelengths vector
% int        = intensity vector
% errs       = vector of one stdev errors for each pixel
% wavelengths= vector of the delta-fns to consider
% widths     = vector of the delta-fns EWs to consider
% del_v      = step size of the output LSD in velocity m/s (i.e. 1500 m/s)
% velpixlim  = number of pixels +/- for the LSD output (i.e. 200 pixels)

A = compute_Ajk(del_v,velpixlim,wave,wavelengths,widths);

R = int(:) - 1;              %the normalised, continuum subtracted spectrum
V = diag(1./(errs(:).^2));   %the inverse variances

%z = (A' * V * A)^-1 A' * V * R
% V is a vector of pixel variances
% R is the observed normalised, continuum subtracted spectrum
% A is determined using compute_Ajk (below)

% This can be computed by thinking of it as AAx=b
% where AA is an array ((A' * V * A)^-1), x is a
% vector (the output z) and b is a vector (A' * V * R) in which case the
% solution is x = AA\b (a.k.a x = inv(AA)*B) i.e.

AA = A' * V * A;
b =  A' * V * R;

LSD = AA\b;


function A = compute_Ajk(del_v,velpixlim,wave,wavelengths,widths)
%%%%%%%%%%%%%%%%%%%%%%%%%%%%%%%%%%%%%%%%%%%%%%%%%%%%%%%%%%%%%%%%%%%%%%%%%%%%
c = 299792458; %speed of light m/s
%input wavelength of spectrum is: wave
%input delta function list is: wavelengths, widths
%assuming 1500 m/s per output bin and 601 bins then
% del_v = 1500; %m/s bin size in out put profile
```

```
% velpixlim = 150;

output_vel = (-velpixlim:velpixlim) * del_v;

%fixed input arrays
t_wave = repmat(wave(:)',numel(wavelengths),1);
t_lam_i = repmat(wavelengths(:),1,numel(wave));
t_d_i = repmat(widths(:),1,numel(wave));
%preallocate array
A = zeros(numel(wave),numel(output_vel));
parfor k = 1:numel(output_vel)               %output pixel number
    %Vk is the RV of output LSD profile bin
    Vk = output_vel(k);
    %triangular function
    x = (Vk - c*((t_wave - t_lam_i)./t_lam_i))/del_v;
    trian_x = zeros(size(x));
    M = x>-1 & x<0;
    N = x>0  & x<1;
    trian_x(M) = 1+x(M);
    trian_x(N) = 1-x(N);
    %depths is array t_d_i
    A(:,k) = sum( t_d_i .* trian_x ,1);
end
```

Appendix B

Line profiles phased to literature frequencies for QW Puppis

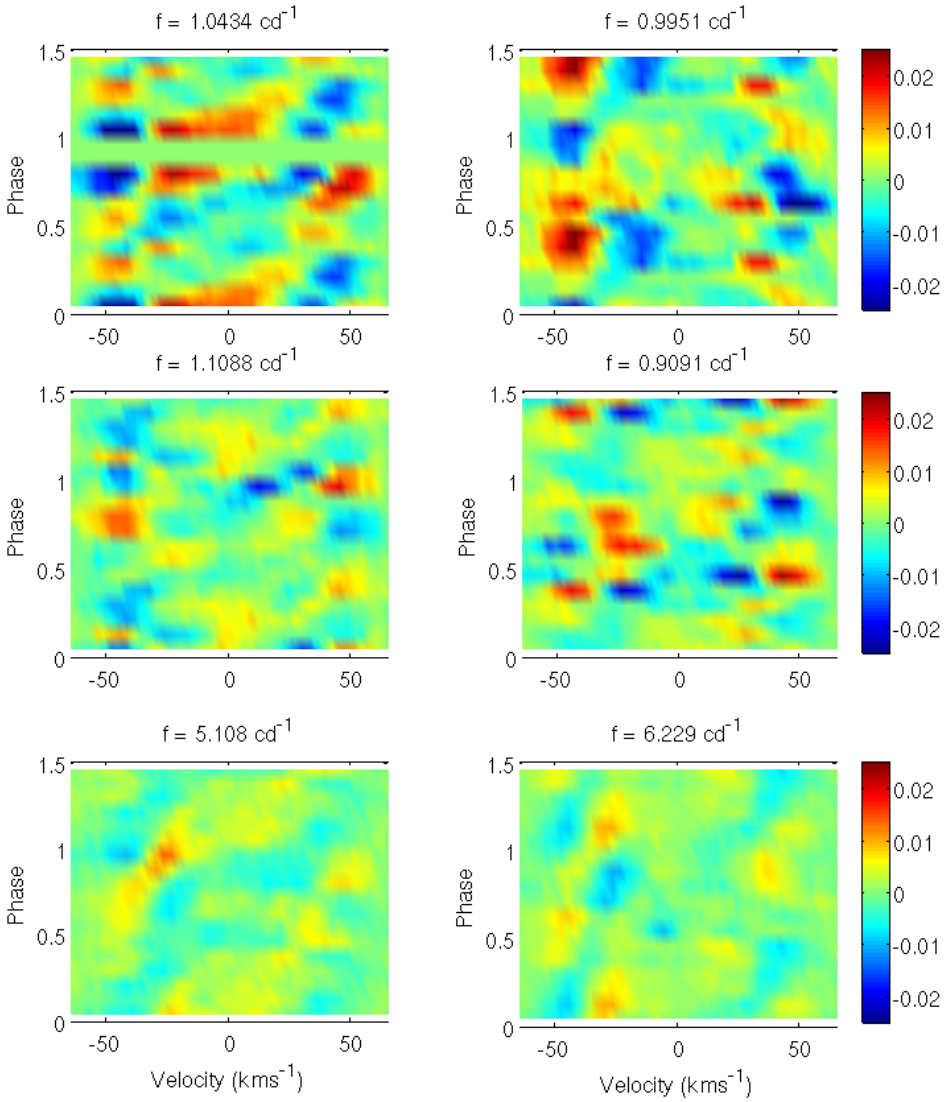

Forced fits of the frequencies found by Poretti et al. (1997): 1.0434±0.0004, 0.9951±0.0010, 1.1088±0.0017 and 0.9019±0.0020 cd^{-1} in *uvby* photometry as shown in the top four subplots. Forced fits of the two frequencies not found in this work but which were discerned by Wright (2008): frequencies of 6.229 and 5.108 cd^{-1} in the lower two subplots. Whilst there is some suggestion of phased variation at 5.108 cd^{-1} it is much

more strongly shown at $5.219cd^{-1}$ in this study. These frequencies generally show poor systematic variation over the imposed frequencies.

Appendix C

Line profiles phased to literature frequencies for IR Draconis

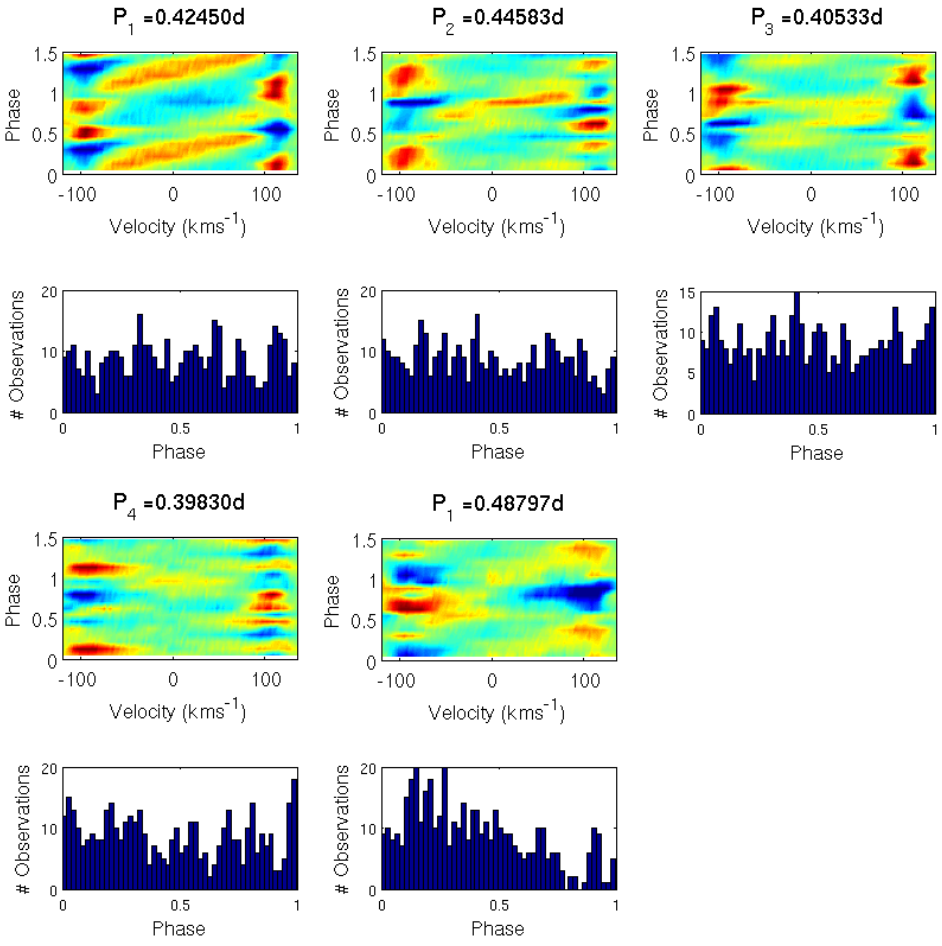

Line profiles Phased to literature frequencies for IR Draconis from Aerts et al. (1998) and Henry et al. (2005). Phasing the line profiles from IR Draconis to the literature frequencies liberates little more than the single frequency found from both analysis of moments and pixel-by-pixel.

Appendix D

Spectral line list for abundance analysis

Table D.1: The spectral line list used for metallicity determination.

Species	Wavelength (Å)	Excitation Potential (eV)	$\log(gf)$
Si I	5645.6130	4.930	-2.140
Si I	5675.4170	5.619	-1.231
Si I	5708.4000	4.954	-1.470
Si I	5747.6670	5.614	-1.543
Si I	5753.6230	5.616	-1.754
Si I	6125.0210	5.614	-1.464
Si I	6131.8520	5.616	-1.615
Si I	6145.0160	5.616	-1.310
Si I	6194.4160	5.871	-2.511
Si I	6237.3190	5.614	-0.975
Si I	6243.8150	5.616	-1.242
Si I	6244.4660	5.616	-1.093
Si I	6254.1880	5.619	-0.929
Si I	6414.9800	5.871	-1.035
Si II	6347.1090	8.121	0.297
Si II	6371.3710	8.121	-0.003
Ti I	4981.7310	0.848	0.504
Ti I	5210.3850	0.048	-0.884
Ti II	4501.2698	1.116	-0.770
Ti II	4518.3270	1.080	-2.910
Ti II	4544.0162	1.243	-2.580
Ti II	4563.7574	1.221	-0.690
Ti II	4589.9465	1.237	-2.940
Ti II	4779.9850	2.048	-1.260
Ti II	4805.0850	2.061	-0.960
Ti II	5010.2105	3.095	-1.290
Ti II	5013.6770	1.582	-2.190
Ti II	5129.1520	1.892	-1.240
Ti II	5211.5304	2.590	-1.160
Ti II	5381.0150	1.566	-1.920
Ti II	5490.6900	1.566	-2.430
Ti II	6491.5610	2.061	-1.793
Fe I	4547.8470	3.546	-1.012

Continued on next page

Species	Wavelength (Å)	Excitation Potential (eV)	log(gf)
Fe I	4566.9885	3.415	-2.080
Fe I	4602.9410	1.485	-2.209
Fe I	4607.6460	3.266	-1.467
Fe I	4613.2027	3.292	-1.670
Fe I	4625.0450	3.241	-1.340
Fe I	4632.9110	1.608	-2.913
Fe I	4638.0098	3.602	-1.119
Fe I	4733.5910	1.485	-2.988
Fe I	4735.8430	4.076	-1.325
Fe I	4736.7730	3.211	-0.752
Fe I	4745.8000	3.654	-1.270
Fe I	4757.5780	3.274	-2.040
Fe I	4791.2462	3.274	-2.435
Fe I	4802.8797	3.642	-1.514
Fe I	4843.1430	3.396	-1.840
Fe I	4909.3830	3.929	-1.231
Fe I	4942.4590	4.220	-1.409
Fe I	4946.3870	3.368	-1.170
Fe I	4966.0880	3.332	-0.871
Fe I	4967.8970	4.191	-0.487
Fe I	4969.9170	4.217	-0.710
Fe I	4973.1019	3.960	-0.950
Fe I	4988.9500	4.154	-0.890
Fe I	4994.1295	0.915	-3.080
Fe I	5014.9420	3.943	-0.303
Fe I	5027.1230	4.154	-0.534
Fe I	5028.1260	3.573	-1.123
Fe I	5029.6176	3.415	-2.050
Fe I	5054.6426	3.640	-1.921
Fe I	5067.1496	4.220	-0.970
Fe I	5074.7480	4.220	-0.200
Fe I	5076.2640	4.301	-0.809
Fe I	5090.7730	4.256	-0.400
Fe I	5121.6390	4.283	-0.810
Fe I	5123.7200	1.011	-3.068
Fe I	5131.4680	2.223	-2.515
Fe I	5133.6880	4.178	0.140
Fe I	5141.7390	2.424	-1.964
Fe I	5150.8390	0.990	-3.003
Fe I	5151.9109	1.011	-3.322
Fe I	5159.0576	4.283	-0.820
Fe I	5162.2729	4.178	0.020
Fe I	5194.9410	1.557	-2.090
Fe I	5198.7110	2.223	-2.135

Continued on next page

Species	Wavelength (Å)	Excitation Potential (eV)	log(gf)
Fe I	5217.3890	3.211	-1.070
Fe I	5228.3760	4.220	-1.290
Fe I	5242.4910	3.634	-0.967
Fe I	5243.7760	4.256	-1.150
Fe I	5250.6460	2.198	-2.181
Fe I	5253.4617	3.283	-1.573
Fe I	5281.7900	3.038	-0.834
Fe I	5302.3000	3.283	-0.720
Fe I	5315.0700	4.371	-1.550
Fe I	5339.9290	3.266	-0.647
Fe I	5341.0240	1.608	-1.953
Fe I	5361.6250	4.415	-1.430
Fe I	5364.8710	4.445	0.228
Fe I	5373.7086	4.473	-0.860
Fe I	5379.5740	3.694	-1.514
Fe I	5389.4790	4.415	-0.410
Fe I	5391.4590	4.154	-0.782
Fe I	5393.1670	3.241	-0.715
Fe I	5398.2790	4.445	-0.670
Fe I	5400.5010	4.371	-0.160
Fe I	5405.7750	0.990	-1.844
Fe I	5410.9098	4.473	0.398
Fe I	5415.1990	4.386	0.642
Fe I	5424.0680	4.320	0.520
Fe I	5434.5238	1.011	-2.122
Fe I	5441.3387	4.312	-1.730
Fe I	5445.0420	4.386	-0.020
Fe I	5466.3960	4.371	-0.630
Fe I	5472.7090	4.209	-1.495
Fe I	5473.9005	4.154	-0.760
Fe I	5483.0988	4.154	-1.407
Fe I	5497.5160	1.011	-2.849
Fe I	5501.4650	0.958	-3.047
Fe I	5506.7790	0.990	-2.797
Fe I	5543.1470	3.695	-1.570
Fe I	5560.2116	4.434	-1.190
Fe I	5563.6000	4.191	-0.990
Fe I	5569.6180	3.417	-0.486
Fe I	5576.0888	3.430	-1.000
Fe I	5586.7559	3.368	-0.120
Fe I	5633.9460	4.991	-0.270
Fe I	5638.2620	4.220	-0.870
Fe I	5686.5300	4.548	-0.446
Fe I	5701.5440	2.559	-2.216

Continued on next page

Species	Wavelength (Å)	Excitation Potential (eV)	log(gf)
Fe I	5705.9920	4.607	-0.530
Fe I	5717.8329	4.284	-1.130
Fe I	5731.7620	4.256	-1.300
Fe I	5752.0320	4.549	-1.177
Fe I	5762.9920	4.209	-0.450
Fe I	5809.2170	3.883	-1.840
Fe I	5816.3730	4.548	-0.601
Fe I	5859.5860	4.549	-0.419
Fe I	5862.3570	4.549	-0.127
Fe I	5883.8170	3.960	-1.360
Fe I	5930.1799	4.652	-0.230
Fe I	5934.6549	3.928	-1.170
Fe I	5987.0650	4.796	-0.429
Fe I	6003.0110	3.881	-1.120
Fe I	6008.5560	3.884	-0.986
Fe I	6020.1690	4.607	-0.270
Fe I	6024.0580	4.548	-0.120
Fe I	6027.0509	4.076	-1.089
Fe I	6056.0047	4.733	-0.460
Fe I	6065.4820	2.608	-1.530
Fe I	6078.4910	4.796	-0.321
Fe I	6127.9060	4.143	-1.399
Fe I	6136.6150	2.453	-1.400
Fe I	6170.5060	4.795	-0.440
Fe I	6173.3340	2.223	-2.880
Fe I	6213.4300	2.223	-2.482
Fe I	6219.2810	2.198	-2.433
Fe I	6230.7220	2.559	-1.281
Fe I	6232.6400	3.654	-1.223
Fe I	6252.5550	2.404	-1.687
Fe I	6256.3610	2.453	-2.408
Fe I	6265.1320	2.176	-2.550
Fe I	6270.2230	2.858	-2.464
Fe I	6335.3300	2.198	-2.177
Fe I	6336.8230	3.686	-0.856
Fe I	6338.8760	4.795	-1.060
Fe I	6380.7430	4.186	-1.376
Fe I	6408.0180	3.686	-1.018
Fe I	6419.7780	5.348	-4.379
Fe I	6421.3500	2.279	-2.027
Fe II	4520.2240	2.807	-2.617
Fe II	4541.5240	2.856	-2.973
Fe II	4576.3400	2.844	-2.976
Fe II	4620.5210	2.828	-3.315

Continued on next page

Species	Wavelength (Å)	Excitation Potential (eV)	$\log(gf)$
Fe II	4731.4530	2.891	-3.127
Fe II	5120.3520	2.828	-4.256
Fe II	5256.9380	2.891	-4.182
Fe II	5362.8690	3.199	-2.616
Fe II	6084.1110	3.199	-3.881
Fe II	6147.7410	3.889	-2.827
Fe II	6149.2580	3.889	-2.841
Fe II	6238.3920	3.889	-2.754
Fe II	6247.5570	3.892	-2.435
Fe II	6416.9190	3.892	-2.877
Fe II	6432.6800	2.891	-3.687

References

H. A. Abt and N. I. Morrell. The Relation between Rotational Velocities and Spectral Peculiarities among A-Type Stars. *ApJS*, 99:135, July 1995. doi: 10.1086/192182.

C. Aerts. Asteroseismology lecture notes. Universities of Leuven and Nijmegen, 2006. Figure by Christensen-Dalsgaard, J.

C. Aerts, M. de Pauw, and C. Waelkens. Mode identification of pulsating stars from line profile variations with the moment method. an example - The Beta Cephei star Delta Ceti. *A&A*, 266:294–306, December 1992.

C. Aerts, L. Eyer, and E. Kestens. The discovery of new gamma Doradus stars from the HIPPARCOS mission. *A&A*, 337:790–796, September 1998.

C. Aerts, J. Christensen-Dalsgaard, and D. W. Kurtz. *Asteroseismology*. Springer, 1st edition, 2010. doi: 10.1007/978-1-4020-5803-5.

L. A. Balona. Mode identification from line profile variations. *MNRAS*, 219:111–129, March 1986a.

L. A. Balona. Mode identification from line profile variations. II - A quantitative least-squares algorithm. *MNRAS*, 220:647–656, June 1986b.

L. A. Balona, J. A. Guzik, K. Uytterhoeven, J. C. Smith, P. Tenenbaum, and J. D. Twicken. The Kepler view of γ Doradus stars. *MNRAS*, 415:3531–3538, August 2011. doi: 10.1111/j.1365-2966.2011.18973.x.

J. R. Barnes, J. S. Jenkins, H. R. A. Jones, P. Rojo, P. Arriagada, A. Jordán, D. Minniti, M. Tuomi, S. V. Jeffers, and D. Pinfield. Red Optical Planet Survey: a new search for habitable earths in the southern sky. *MNRAS*, 424:591–604, July 2012. doi: 10.1111/j.1365-2966.2012.21236.x.

C. A. Beichman, G. Bryden, K. R. Stapelfeldt, T. N. Gautier, K. Grogan, M. Shao, T. Velusamy, S. M. Lawler, M. Blaylock, G. H. Rieke, J. I. Lunine, D. A. Fischer, G. W. Marcy, J. S. Greaves, M. C. Wyatt, W. S. Holland, and W. R. F. Dent. New Debris Disks around Nearby Main-Sequence Stars: Impact on the Direct Detection of Planets. *ApJ*, 652:1674–1693, December 2006. doi: 10.1086/508449.

S. V. Berdyugina, H. Korhonen, C. Schrijvers, and J. H. Telting. Mapping the Non-Radial Pulsations. In M. A. Smith, H. F. Henrichs, and J. Fabregat, editors, *IAU Colloq. 175: The Be Phenomenon in Early-Type Stars*, volume 214 of *Astronomical Society of the Pacific Conference Series*, page 268, 2000.

M. Breger, L. Fossati, L. Balona, D. W. Kurtz, P. Robertson, D. Bohlender, P. Lenz, I. Müller, T. Lüftinger, B. D. Clarke, J. R. Hall, and K. A. Ibrahim. Relationship between Low and High Frequencies in δ Scuti Stars: Photometric Kepler and Spectroscopic Analyses of the Rapid Rotator KIC 8054146. *ApJ*, 759:62, November 2012. doi: 10.1088/0004-637X/759/1/62.

M. Briquet and C. Aerts. A new version of the moment method, optimized for mode identification in multiperiodic stars. *A&A*, 398:687–696, February 2003. doi: 10.1051/0004-6361:20021683.

E. Brunsden, K. R. Pollard, P. L. Cottrell, D. J. Wright, and P. De Cat. Spectroscopic pulsational frequency identification and mode determination of γ Doradus star HD 12901. *MNRAS*, 427:2512–2522, December 2012a. doi: 10.1111/j.1365-2966.2012.22125.x.

E. Brunsden, K. R. Pollard, P. L. Cottrell, D. J. Wright, P. De Cat, and P. M. Kilmartin. Spectroscopic pulsational frequency identification and mode determination of γ Doradus star HD 135825. *MNRAS*, page 2786, April 2012b. doi: 10.1111/j.1365-2966.2012.20861.x.

H. Bruntt, P. De Cat, and C. Aerts. A spectroscopic study of southern (candidate) γ Doradus stars. II. Detailed abundance analysis and fundamental parameters. *A&A*, 478: 487–496, February 2008. doi: 10.1051/0004-6361:20078523.

M. Cerna and A. F. Harvey. The fundamentals of fft-bsed signal analysis and measurement. Technical report, National Instruments Corporation, 2000.

E. Chapellier, E. Rodríguez, M. Auvergne, K. Uytterhoeven, P. Mathias, M.-P. Bouabid, E. Poretti, D. Le Contel, S. Martín-Ruíz, P. J. Amado, R. Garrido, M. Hareter, M. Rainer, L. Eyer, M. Paparo, D. Díaz-Fraile, A. Baglin, F. Baudin, C. Catala, E. Michel, and R. Samadi. The γ Doradus CoRoT target HD 49434. II. Frequency analysis of the CoRoT data. *A&A*, 525:A23, January 2011. doi: 10.1051/0004-6361/201014207.

M. W. Davie. A study of non-radial pulsations in hd 49434. Astronomy 391 project, University of Canterbury, 2009.

M. W. Davie. Analysing non-radial oscillations in hd 189631. Astronomy 480 project, University of Canterbury, 2011.

T. J. Deeming. Fourier Analysis with Unequally-Spaced Data. *Ap&SS*, 36:137–158, August 1975. doi: 10.1007/BF00681947.

J.-F. Donati, M. Semel, B. D. Carter, D. E. Rees, and A. Collier Cameron. Spectropolarimetric observations of active stars. *MNRAS*, 291:658, November 1997.

M. Duflot, P. Figon, and N. Meyssonnier. Vitesses radiales. Catalogue WEB: Wilson Evans Batten. Subtittle: Radial velocities: The Wilson-Evans-Batten catalogue. *A&A*, 114:269–+, December 1995.

M.-A. Dupret, A. Grigahcène, R. Garrido, M. Gabriel, and R. Scuflaire. Theoretical instability strips for δ Scuti and γ Doradus stars. *A&A*, 414:L17–L20, January 2004. doi: 10.1051/0004-6361:20031740.

M.-A. Dupret, A. Grigahcène, R. Garrido, M. Gabriel, and R. Scuflaire. Convection-pulsation coupling. II. Excitation and stabilization mechanisms in δ Sct and γ Dor stars. *A&A*, 435:927–939, June 2005. doi: 10.1051/0004-6361:20041817.

F. C. Fekel, P. B. Warner, and A. B. Kaye. Spectroscopy of Early F Stars: γ Doradus Candidates and Possible Metallic Shell Stars. *AJ*, 125:2196–2214, April 2003. doi: 10.1086/368239.

G. A. Gontcharov. Pulkovo Compilation of Radial Velocities for 35 495 Hipparcos stars in a common system. *Astronomy Letters*, 32:759–771, November 2006. doi: 10.1134/S1063773706110065.

D.F. Gray. *The observation and analysis of stellar photospheres*. Wiley-Interscience publication. Wiley, 1976. ISBN 9780471323808.

R. O. Gray and R. F. Garrison. The early F-type stars - Refined classification, confrontation with Stromgren photometry, and the effects of rotation. *ApJS*, 69:301–321, February 1989. doi: 10.1086/191315.

A. Grigahcène, V. Antoci, L. Balona, G. Catanzaro, J. Daszyńska-Daszkiewicz, J. A. Guzik, G. Handler, G. Houdek, D. W. Kurtz, M. Marconi, M. J. P. F. G. Monteiro, A. Moya, V. Ripepi, J.-C. Suárez, K. Uytterhoeven, W. J. Borucki, T. M. Brown, J. Christensen-Dalsgaard, R. L. Gilliland, J. M. Jenkins, H. Kjeldsen, D. Koch, S. Bernabei, P. Bradley, M. Breger, M. Di Criscienzo, M.-A. Dupret, R. A. García, A. García Hernández, J. Jackiewicz, A. Kaiser, H. Lehmann, S. Martín-Ruiz, P. Mathias, J. Molenda-Żakowicz, J. M. Nemec, J. Nuspl, M. Paparó, M. Roth, R. Szabó, M. D. Suran, and R. Ventura. Hybrid γ Doradus-δ Scuti Pulsators: New Insights into the Physics of the Oscillations from Kepler Observations. *ApJ*, 713:L192–L197, April 2010. doi: 10.1088/2041-8205/713/2/L192.

J. A. Guzik, A. B. Kaye, P. A. Bradley, A. N. Cox, and C. Neuforge. Driving the Gravity-Mode Pulsations in γ Doradus Variables. *ApJ*, 542:L57–L60, October 2000. doi: 10.1086/312908.

J. A. Guzik, A. B. Kaye, P. A. Bradley, A. N. Cox, C. Neuforge-Verheecke, and P. B. Warner. A Proposed Pulsation Driving Mechanism for γ Doradus Variable Stars. In C. Aerts, T. R. Bedding, and J. Christensen-Dalsgaard, editors, *IAU Colloq. 185: Radial and Nonradial Pulsationsn as Probes of Stellar Physics*, volume 259 of *Astronomical Society of the Pacific Conference Series*, page 502, 2002.

G. Handler. The domain of γ Doradus variables in the Hertzsprung-Russell diagram. *MNRAS*, 309:L19–L23, October 1999. doi: 10.1046/j.1365-8711.1999.03005.x.

G. Handler and R. R. Shobbrook. On the relationship between the δ Scuti and γ Doradus pulsators. *MNRAS*, 333:251–262, June 2002. doi: 10.1046/j.1365-8711.2002.05401.x.

G. Handler, L. A. Balona, R. R. Shobbrook, C. Koen, A. Bruch, E. Romero-Colmenero, A. A. Pamyatnykh, B. Willems, L. Eyer, D. J. James, and T. Maas. Discovery and analysis of p-mode and g-mode oscillations in the A-type primary of the eccentric binary HD 209295*. *MNRAS*, 333:262–279, June 2002. doi: 10.1046/j.1365-8711.2002.05295.x.

J. B. Hearnshaw, S. I. Barnes, G. M. Kershaw, N. Frost, G. Graham, R. Ritchie, and G. R. Nankivell. The Hercules Échelle Spectrograph at Mt. John. *Experimental Astronomy*, 13:59–76, March 2002. doi: 10.1023/A:1023770225275.

G. W. Henry, F. C. Fekel, and S. M. Henry. Eleven New γ Doradus Stars. *AJ*, 129: 2815–2830, June 2005. doi: 10.1086/429876.

H. Hensberge, G. Deridder, C. Doom, H. M. Maitzen, W. W. Weiss, M. Gerbaldi, F. Delmas, N. Morguleff, and P. Renson. A photoelectric investigation of light variability in AP stars. *A&AS*, 46:151–170, October 1981.

I. Hubeny and T. Lanz. Synspec: General Spectrum Synthesis Program. *Astrophysics Source Code Library*, page 9022, September 2011.

S. Jankov. Fourier analysis of rotationally broadened stellar spectra. *Publications de l'Observatoire Astronomique de Beograd*, 50:75–80, August 1995.

T. Kallinger, P. Reegen, and W. W. Weiss. A heuristic derivation of the uncertainty for frequency determination in time series data. *A&A*, 481:571–574, April 2008. doi: 10.1051/0004-6361:20077559.

A. B. Kaye, G. Handler, K. Krisciunas, E. Poretti, and F. M. Zerbi. Gamma Doradus Stars: Defining a New Class of Pulsating Variables. *PASP*, 111:840–844, July 1999. doi: 10.1086/316399.

A. B. Kaye, P. B. Warner, and J. A. Guzik. The first theoretical γ Doradus instability strip. 310:474, May 2004.

D. W. Kurtz, M. S. Cunha, H. Saio, L. Bigot, L. A. Balona, V. G. Elkin, H. Shibahashi, I. M. Brandão, K. Uytterhoeven, S. Frandsen, S. Frimann, A. Hatzes, T. Lueftinger, M. Gruberbauer, H. Kjeldsen, J. Christensen-Dalsgaard, and S. D. Kawaler. The first evidence for multiple pulsation axes: a new rapidly oscillating Ap star in the Kepler field, KIC 10195926. *MNRAS*, 414:2550–2566, July 2011. doi: 10.1111/j.1365-2966.2011.18572.x.

P. Ledoux. The Nonradial Oscillations of Gaseous Stars and the Problem of Beta Canis Majoris. *ApJ*, 114:373, November 1951. doi: 10.1086/145477.

R. B. Leighton. In R. N. Thomas, editor, *Aerodynamic Phenomena in Stellar Atmospheres*, volume 12 of *IAU Symposium*, pages 321–325, 1960.

M. Maintz, T. Rivinius, S. Štefl, D. Baade, B. Wolf, and R. H. D. Townsend. Stellar and circumstellar activity of the Be star omega CMa. III. Multiline non-radial pulsation modeling. *A&A*, 411:181–191, November 2003. doi: 10.1051/0004-6361:20031375.

F. Maisonneuve, K. R. Pollard, P. L. Cottrell, P. M. Kilmartin, D. J. Wright, and P. De Cat. Spectroscopic mode identification of main-sequence non-radially pulsating stars. *Ap&SS*, 328:105–108, July 2010. doi: 10.1007/s10509-009-0219-z.

F. Maisonneuve, K. R. Pollard, P. L. Cottrell, D. J. Wright, P. De Cat, L. Mantegazza, P. M. Kilmartin, J. C. Suárez, M. Rainer, and E. Poretti. Frequency analysis and pulsational mode identification of two γ Doradus stars: HD 40745 and HD 189631. *MNRAS*, 415:2977–2992, August 2011. doi: 10.1111/j.1365-2966.2010.17918.x.

Florian. Maisonneuve. *Three case studies in spectroscopic mode identification of non-radial pulsators.* PhD thesis, University of Canterbury., 2010.

P. Mathias, J.-M. Le Contel, E. Chapellier, S. Jankov, J.-P. Sareyan, E. Poretti, R. Garrido, E. Rodríguez, A. Arellano Ferro, M. Alvarez, L. Parrao, J. Peña, L. Eyer, C. Aerts, P. De Cat, W. W. Weiss, and A. Zhou. Multi-site, multi-technique survey of γ Doradus candidates. I. Spectroscopic results for 59 stars. *A&A*, 417:189–199, April 2004. doi: 10.1051/0004-6361:20034503.

MATLAB. *version 7.10.0 (R2011a)*. The MathWorks Inc., Natick, Massachusetts, 2011.

J. D. Monnier, R. H. D. Townsend, X. Che, M. Zhao, T. Kallinger, J. Matthews, and A. F. J. Moffat. Rotationally Modulated g-modes in the Rapidly Rotating δ Scuti Star Rasalhague (α Ophiuchi). *ApJ*, 725:1192–1201, December 2010. doi: 10.1088/0004-637X/725/1/1192.

M. H. Montgomery and D. O'Donoghue. A derivation of the errors for least squares fitting to time series data. *Delta Scuti Star Newsletter*, 13:28, July 1999.

F. Ochsenbein, P. Bauer, and J. Marcout. The VizieR database of astronomical catalogues. *A&AS*, 143:23–32, April 2000. doi: 10.1051/aas:2000169.

M. A. C. Perryman and ESA, editors. *The HIPPARCOS and TYCHO catalogues. Astrometric and photometric star catalogues derived from the ESA HIPPARCOS Space Astrometry Mission*, volume 1200 of *ESA Special Publication*. 1997.

W. D. Pesnell. A new driving mechanism for stellar pulsations. *ApJ*, 314:598–604, March 1987. doi: 10.1086/165089.

P. Plavchan, M. W. Werner, C. H. Chen, K. R. Stapelfeldt, K. Y. L. Su, J. R. Stauffer, and I. Song. New Debris Disks Around Young, Low-Mass Stars Discovered with the Spitzer Space Telescope. *ApJ*, 698:1068–1094, June 2009. doi: 10.1088/0004-637X/698/2/1068.

E. Poretti, C. Koen, P. Martinez, F. Breuer, H. Haupt, and D. de Alwis. Discovery and analysis of Gamma Doradus type pulsations in the F0 IV star HR 2740=QW PUP. *MNRAS*, 292:621, December 1997.

P. Reegen. SigSpec User's Manual. *ArXiv e-prints*, June 2010.

D. R. Reese, V. Prat, C. Barban, C. van 't Veer-Menneret, and K. B. MacGregor. Mode visibilities in rapidly rotating stars. *ArXiv e-prints*, December 2012.

F. Royer. Determination of v sin i with Fourier transform techniques. *Memorie della Societa Astronomica Italiana Supplementi*, 8:124, 2005.

J. Skuljan. HRSP - A dedicated echelle reduction software package for Hercules. In D. W. Kurtz and K. R. Pollard, editors, *IAU Colloq. 193: Variable Stars in the Local Group*, volume 310 of *Astronomical Society of the Pacific Conference Series*, page 575, May 2004.

A. Slettebak, G. W. Collins, II, T. D. Parkinson, P. B. Boyce, and N. M. White. A system of standard stars for rotational velocity determinations. *ApJS*, 29:137–159, May 1975. doi: 10.1086/190338.

C. A. Sneden. *Carbon and Nitrogen Abundances in Metal-Poor Stars.* PhD thesis, THE UNIVERSITY OF TEXAS AT AUSTIN., 1973.

R. H. D. Townsend. Asymptotic expressions for the angular dependence of low-frequency pulsation modes in rotating stars. *MNRAS*, 340:1020–1030, April 2003a. doi: 10.1046/j.1365-8711.2003.06379.x.

R. H. D. Townsend. A semi-analytical formula for the light variations due to low-frequency g modes in rotating stars. *MNRAS*, 343:125–136, July 2003b. doi: 10.1046/j.1365-8711.2003.06640.x.

K. Uytterhoeven, P. Mathias, E. Poretti, M. Rainer, S. Martín-Ruiz, E. Rodríguez, P. J. Amado, D. Le Contel, S. Jankov, E. Niemczura, K. R. Pollard, E. Brunsden, M. Paparó, V. Costa, J.-C. Valtier, R. Garrido, J. C. Suárez, P. M. Kilmartin, E. Chapellier, C. Rodríguez-López, A. J. Marin, F. J. Aceituno, V. Casanova, A. Rolland, and I. Olivares. The γ Doradus CoRoT target HD 49434. I. Results from the ground-based campaign. *A&A*, 489:1213–1224, October 2008. doi: 10.1051/0004-6361:200809992.

D. J. Wright. *Spectroscopic Mode Identification In A Sample Of Non-Radially Pulsating Stars*. Phd, University of Canterbury, 2008.

F. M. Zerbi and A. B. Kaye. Observation of γ Doradus Stars in the Space Asteroseismology Era (invited paper). 259:494, 2002.

W. Zima. FAMIAS User Manual. *Communications in Asteroseismology*, 155:17–121, October 2008.